RICE UNIVERSITY

Iron: From Synthesis, Characterization, and Application of Sulfide Green Rust to Viability in Arsenic Water Treatment

by

Christopher Jay Jones

A THESIS SUBMITTED
IN PARTIAL FULFILLMENT OF THE
REQUIREMENTS FOR THE DEGREE

Doctor of Philosophy

APPROVED, THESIS COMMITTEE:

Vicki L. Colvin,
Kenneth S. Pitzer-Schlumberger
Professor of Chemistry, Chair

Lon J. Wilson
Professor of Chemistry

Pedro J. J. Alvarez
George R. Brown Professor of
Engineering

HOUSTON, TEXAS
May 2013

ABSTRACT

Iron: From Synthesis, Characterization, and Application of Sulfide Green Rust to Viability in Arsenic Water Treatment

by

Christopher Jay Jones

Iron chemistry plays an important role in our world. At the nanoscale, iron oxide nanoparticles (nanomagnetite) have many inherent physical or chemical characteristics that drive potential solutions to real-world problems; appropriation of nanomagnetite's properties as a "scaffold" for chemistry would further enhance its effectiveness in applications. In an effort to make use of nanomagnetite's physical properties, a new "Sulfide Green Rust" (sGR) has been synthesized from magnetic iron nanoparticles. The material is crystalline, reactive due to high iron(II) content, and dissolves in the aqueous phase. Nanomagnetite's magnetic properties were also observed to persist after sGR synthesis. X-ray absorption spectroscopy (XAS) confirmed the synthesis of this new FeS_2-like material. The crystallinity, composition, and various physical characteristics were examined using a host of techniques including X-ray diffraction (XRD), X-ray photoelectron spectroscopy (XPS), transmission electron microscopy (TEM), Mössbauer spectroscopy, CRYO-TEM, Raman spectroscopy, and ultraviolet-to-visible (UV-Vis) spectroscopy. To

demonstrate its use, the material was then subjected to a test of its reactive potential, namely water remediation of an orange dye contaminant.

Iron serves a function at the macroscale as well regarding water treatment, since iron coagulation-filtration is the industry standard for arsenic treatment. Determining a technology's merit as a solution goes beyond technical concern, however, as environmental and economic aspects also play important roles. Life Cycle Analysis, or LCA, methodology works to holistically compare each of these facets from cradle to grave. To address the current arsenic drinking water requirements at a case setting in Hungary, the LCA technique was applied on two example arsenic removal technologies, both coagulation-filtration and adsorption. 9 out of 10 considered impact categories tended to favour coagulation-filtration in this small municipality study, however realistic variations in water chemistry and product characteristics led to some overlap of their environmental impact. Electricity did not have a large direct impact, regeneration of the adsorption technology was very costly, and adsorption's hazardous waste was not reduced compared to coagulation-filtration. Coagulation-filtration is also the cheaper of the two technologies; its highest cost is that of waste disposal, while the highest single expense modeled is that of adsorption media cost.

ACKNOWLEDGEMENTS

I am extremely grateful and want to express my sincere thanks to everyone who has contributed to making my graduate experience a success.

First let me thank Dr. Vicki Colvin, my thesis advisor, for the many good ideas and skill building opportunities she's presented to me over the years. I could never have imagined the opportunities I would have access to, and many of them are directly or indirectly related to her and my experience in her lab.

Next, I want to thank Dr. Carolina Avendano, for her caring guidance and planning support. Carolina always has an intrinsic desire to understand and help people; navigating this path would have been much more convoluted without her counsel.

During my stay in Hungary, no person deserves more acknowledgement than Dr. Dora Laky, my official Fulbright host. It is inconceivable to think our project would have succeeded without her engineering and technical knowledge, her very open-door availability, and of course her guidance when navigating issues foreign to me in Hungary. Dr. Ildiko Galambos deserves credit in the same breath, being a knowledgeable collaborator, a third person to bounce ideas off of, and essentially my co-host in Hungary. I should also thank all the people at BME's Department of Sanitary and Environmental Engineering and Corvinus University of Budapest's Department of Food Engineering for their entirely welcoming, friendly, and helpful faculty and staff.

Special thanks also for Huba Bruckner, Former Executive Director of the Fulbright Commission Hungary, for his kind guidance this year, as well as over the last 20 years in making this Commission stand out. Annamaria Sas, Program Officer at the Fulbright Commission, also deserves credit for organizing our exciting monthly events in Hungary, and doing a stellar job at keeping the Fulbright family together. Both of these individuals made my 10 months in Hungary a both a successful and spectacular experience I will remember my entire life.

Many thanks to Dr. Caroline Quenemoen, for her support in guiding me through the long application process; Gergely Szakacs and Adrianna Potacsniak, for knowing the right people at the right time for me to get in touch with, and kindly passing my information along; Houston's Hungarian Consul Aronoff, for taking the time to meet with and recommend me to the Fulbright Commission; and Ann-Paula and Gabriella Cserei, for introducing me to my first real dose of Hungarian language and culture.

Let me thank the SEA staff for their diligence with Rice's instrumentation. At some institutions, graduate students must find, repair, and maintain instruments on top of balancing their academic, research, and teaching requirements. The SEA helps to eliminate this extra distraction, so I am extremely grateful for their work. Special thanks to Bo, Rich, Wenh, and Angelo for their support during my time at Rice.

I want to thank fellow and former Colvin lab members: J.T., Denise, Arjun, Zuzanna, Huiguang, Camila, Tushar, Cafer, Josh, Karl, Seung Soo, Minjung, Elizabeth, Adina, Natalia, Qingbo, Hema, Feng, Jennifer, and William. Our lab constantly "self assembled' to both

support in times of need and to nurture our professional development for a conference or presentation. We simply could not have functioned without collective support, so I am extremely thankful to have worked with so many determined self-starters. Teresa and Kelly also have heaps of credit due to them; when time was limited, they made mountains move.

Many of my Rice colleagues and personal friends deserve credit for their support over the years. David, Alex, Emilia, Victor, Sagnak, Stuart, Alvin, Jorge, Eoghan, Leo, Courtney, Meagan, Indre, Ash, Irina, Mikas, and Anjte, to name a few, have all helped guide me in their own way during my graduate career.

Finally, I want to express my greatest thanks to my mother Cindy, my father James, my sister Amanda, all of the Jones and Putnam clans, closest friends, and the others around the world for their personal support during this challenging yet exciting time in my life.

Thank you all so much for providing me balance during this endeavor.

TABLE OF CONTENTS

LIST OF FIGURES

LIST OF TABLES

Chapter 1 The Green Rust Family: A Review

This review chapter summarizes the current state of knowledge about a family of materials known as 'green rusts'. First, both natural and synthetic routes to their production will be described. A critical aspect for the chemistry is the characterization of the product. It has a complex structure, and to fully describe both the iron oxide and intercalant material requires several different methods. Finally we detail the possible applications of green rust and its significance in natural environmental systems.

1.1 Green Rust - Overview

Green rusts (GR) have gained interest in recent years for their many applications in environmental remediation. This class of reduced iron oxides can degrade trichloroethylene (TCE),[1,2] reduce nitrate,[3] remove disinfection by-products,[4] and remediate radioactive waste.[5,6] Green rusts are a family of mixed-valent iron materials, composed of alternating layers of iron and oxygen that may intercalate ions of a range of sizes and characters (Figures 1.1). In this sense GRs are like a kind of iron-rich clay. Their reactivity in environmental systems is due to the high degree of iron (II) content. As iron oxides reduce, either naturally or through intentional synthesis, green rusts form (Figure 1.2) as an intermediate phase between more stable iron oxides and oxyhydroxides such as magnetite (Fe_3O_4) and lepidocrocite (γ-FeOOH).[7] Striking because of their deep green color, when exposed to air green rusts oxidize back to various iron oxide phases.[8,9,10]

Green rusts do occur naturally and have been recognized as a common material found alongside other iron minerals; however, they have only recently been named, “fougerite,” after their identification in a mineral deposit near Fougères, France (IMA 2003-057).[11,12] GR can also form in cast iron water pipes as they corrode, and the patina on sunken ships exhibit a form of green rust.[13] Finally, an area of great interest is the role of green rust in the activity of dissimalatory reducing bacteria. In these cases green rusts are formed by the anoxic bacterial reduction of Fe(III) (Figure 1.3).[14,15] Typically this can occur under any marine condition thanks to scaling that protects lower corrosion layers.[16,17,] Such chemistry may have also played an important role in Earth’s ancient ocean as observed in deep, anoxic lakes such as Lake Matano in Indonesia.[18]

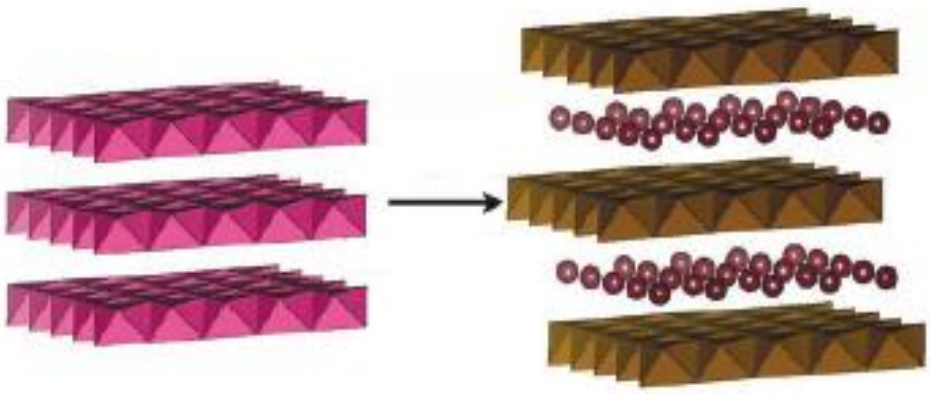

Figure 1.1. Green rust, a layered double hydroxide (LDH), is composed of repeating iron oxy-hydroxide planes interspaced by an intercalant layer. Adapted from Ma. et al., *Journal of the American Chemical Society* 2007.[8]

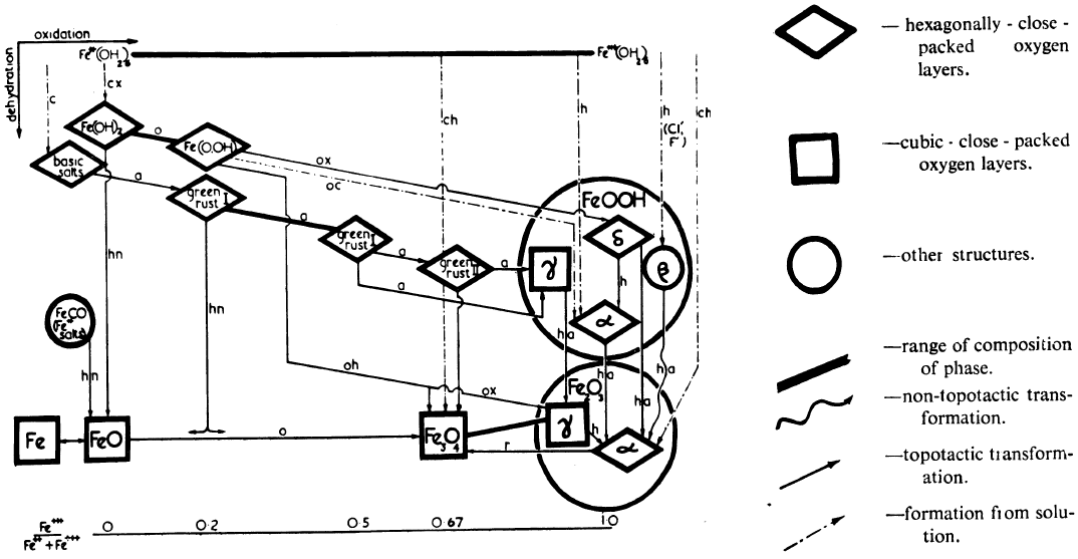

Figure 1.2. Historical iron oxidation observations show green rusts (GR) to be intermediates along oxidation/dehydration pathways. (a: exposure to air; c: in alkaline conditions; h: with heat; n: in nitrogen; o: on oxidation; r: on reduction; e: in excess) Adapted from Bernal et al., *Clay Min. Bull., 1959.* [7]

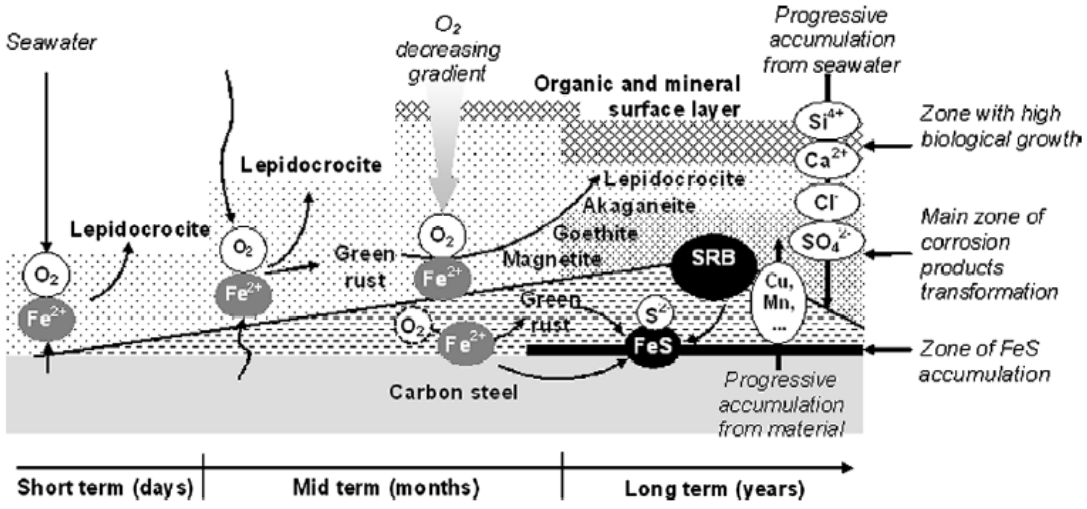

Figure 1.3. Green rust is one of many corrosion products found in nature, and often serves as a mediator between reduced iron species such as iron sulfides and more oxidized iron minerals such as goethite or lepidocrocite. Adapted from Pineau et al., *Corrosion Science,* 2007.[17]

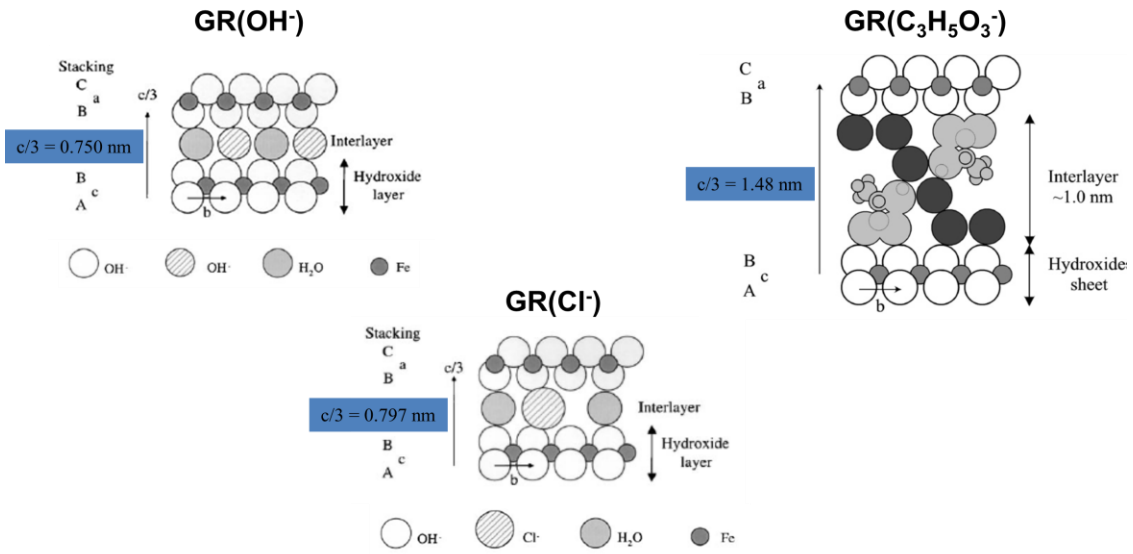

Figure 1.4 Many intercalants can be used to form GR. GR structure has sheets of $Fe(OH)_6$ octahedra with a portion of its Fe(II) replaced by Fe(III), giving rise to a positive charge and thus the accompanying anionic intercalant layer .[9] Varying anions small and large have been incorporated, resulting in changes of lattice d-spacings. Adapted from Genin et al., *App. Geochem.,* 2000[11] and Sabot et al., *Corrosion Science.,* 2007,[10] respectively.

Synthetic green rusts have emerged as an interesting material in their own right, and dozens of types have been reported. Most of these have structural features shared with natural green rusts, such as the iron(II)-rich oxyhydroxide layered clays. Their difference lies in the intercalants that can be incorporated into the material. Ions such as chloride,[19,20,21] sulfate,[22,23,20,24] and carbonate,[25,26,27,28] are commonly seen in synthetic products, but even more unusual are the intercalation of fluoride,[3] selenate,[29] lactate,[10] oxalate,[30] and even large alkyl chains over 4 nm in size (Figure 1.4).[31] GRs are

capable of anion exchange, making them possible delivery agents for their intercalants, in addition to providing reactive iron for remediation.[32]

1.2 The synthesis of green rusts

1.2.1 Strategies for forming green rusts

Green rust can be produced in laboratories, and there is remarkable convergence among the strategies.[33] They begin with the dissolution of some solid-to-semisolid iron mineral, often with iron(II) character. Next, the material is oxidized to form a mixed valent species which is then precipitated as a green rust (Figure 1.5).[34,33] One interesting alternative recently developed is topotactic: namely, the original crystal structure of the iron(II) starting product is preserved during the oxidation process. As a result, final product bears some resemblance to the final green rust structure, and such a mechanism may be responsible for core/shell GR samples.[35]

1.2.2 Oxidation of Iron(II) oxides

Oxidation in a green rust synthesis is a crucial step, and researchers have adopted two distinct approaches. In the first more common method, $Fe(OH)_2$ is oxidized by the dissolved oxygen present in an aqueous solution, and if an appropriate intercalant is present this oxidation leads to green rust.[25,30,24,36] Alternatively, Fe(II) and Fe(III) salts such as iron chloride or iron sulfide can also be co-precipitated by NaOH base addition into a green rust structure that contains the anions.[22,19,37,38,28,] (Figure 1.6). Alternative approaches to GR production have evolved, including more rapid

coprecipitation, but in these cases air exposure must still be controlled and limited.[22,39,40]

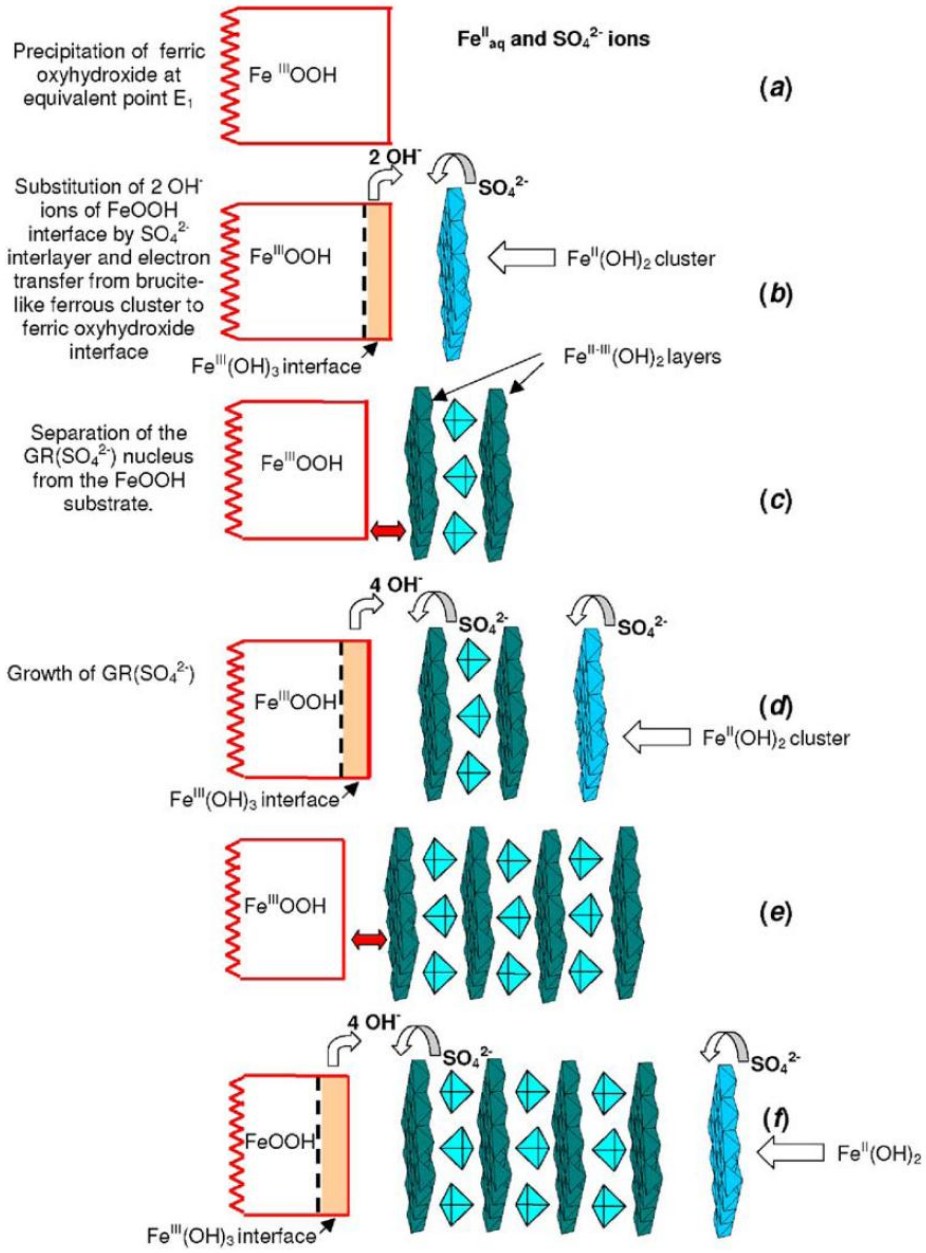

Figure 1.5. Detailed **s**chematic of the dissolution/recrystallization mechanism of formation for GR. Adapted from Ruby et al., *Comptes Rendus Geoscience,* 2006.[34]

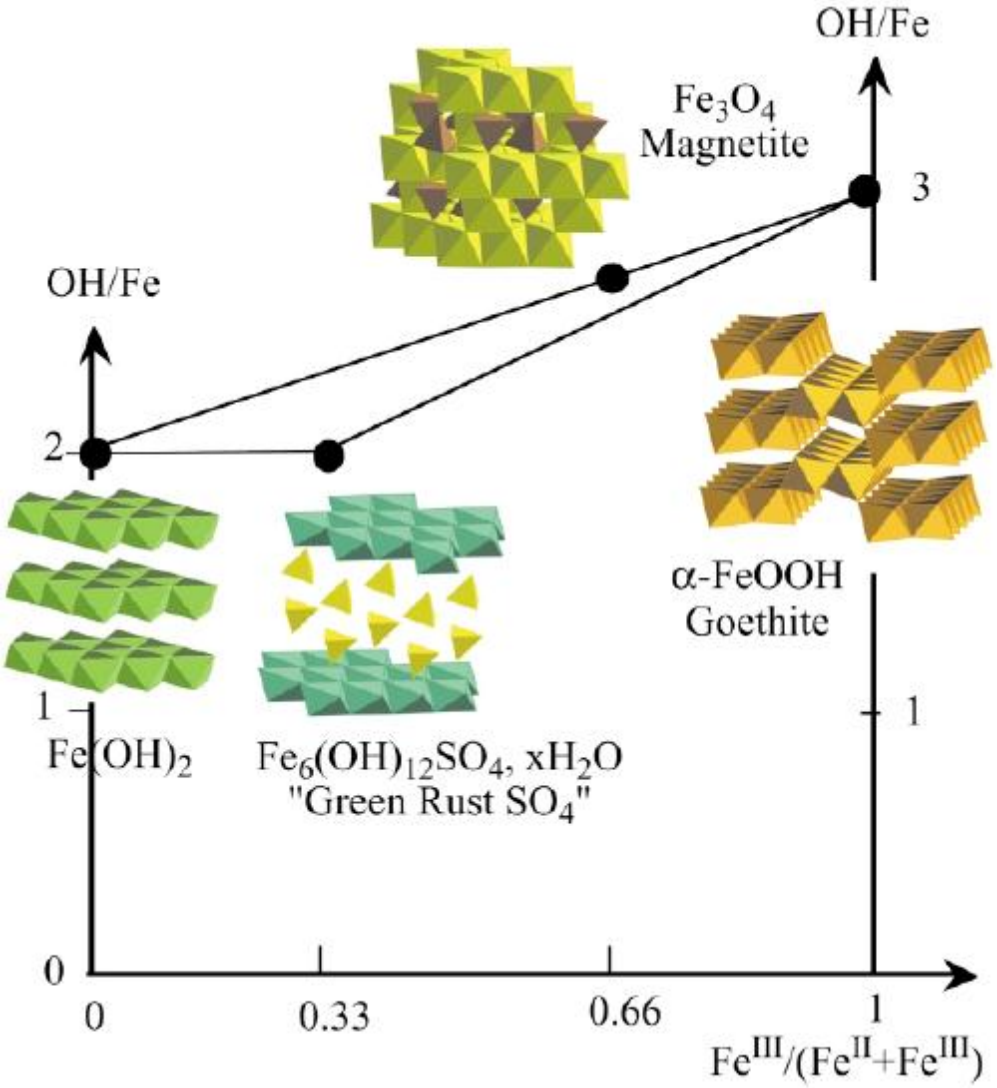

Figure 1.6. Synthesis of GR is typically an oxidative process. Iron (II) hydroxide layers are given partial charge by oxidation of iron (movement to the right), leading to anions stabilizing the entire neutral-charge compound. To date, only biomediated syntheses are known to produce GR from a reductive process (movement to the left) rather than oxidative. Adapted from Jolivet et al., *Chem. Comm.,* 2004.[41]

1.2.3 Electrolysis

Electrochemical oxidation of iron is another known mechanism for producing green rust.[27,21,20,] A Fe(II) containing solution, often $FeCl_2$, is injected into a sealed, deaerated $NaHCO_3$ solution, while the entire reaction is monitored by recording the pH and redox potential (Eh) of the sample. Electrochemical methods provide useful thermodynamic data and related Pourbaix diagrams.[33]

1.2.4 Biological reduction of iron oxides

Sulfur-reducing bacteria offer a unique pathway to form green rust. Several such microbes have been observed to produce GR, some of which almost exclusively such as the *shewanella putrefaciens* strain.[42] Bacteria use ferric oxyhydroxide as an electron acceptor for the oxidation of organic matter.[27,17,28] To date, this is the only method known to produce GR from a reductive process rather than oxidative. Bacteria forming GR are also known to occur around the world naturally in standing soil solutions, or so-called "gley" soils.[28,26]

1.2.5 Post Synthesis GR Oxidation

Several variables control the stability, oxidation, and transformation of GR. These variables include (a) the presence and/or rate of flow of oxygen or some other oxidizer (e.g. H_2O_2), (b) the ratio of another anion present in solution ([anion]/[GR solid]), (c) the pH of the solution, and (d) the presence of interfering ions such as phosphates and silicates that have been observed to inhibit GR dissolution.[43,44, 45,46]

Depending on these parameters, green rust can oxidize via two different pathways (Figure 1.7). One process uses a topotactic solid state pathway, and requires fast oxidation as mentioned previously. Oxygen must be abundant during these reactions, and sometimes the synthesis is conducted in air.[45] The result is a Fe(II)-depleted "ferric" GR which retains the layered green rust crystal structure.[36] Direct spectroscopic evidence via X-ray photoelectron spectroscopy demonstrates that hydroxyl oxidation accompanies bonded Fe(II) oxidation.[37] After much aging, transformation occurs into stable, fully oxidized end products such as goethite (α-FeOOH), lepidocrocite (γ-FeOOH), and sometimes hematite (α-Fe_2O_3).[43]

The second mechanistic pathway is a dissolution/reprecipitation pathway. Here, the iron starting material is dissolved into a soluble, mixed-valent species, and oxidation occurs (whole or partial) from Fe(II) to Fe(III). Finally precipitation occurs upon reaching concentration saturation.[43,47] If this reaction is allowed to proceed to completion, the products such as goethite and lepidocrocite (γ-FeOOH) are observed.

1.3 Characterizing Green Rust (GR)

Characterization of these materials must provide diverse information including:

- The bond distances between iron and oxygen in the layers
- The spacing between iron-oxyhydroxide layers
- The chemical identity and loading of intercalated molecules

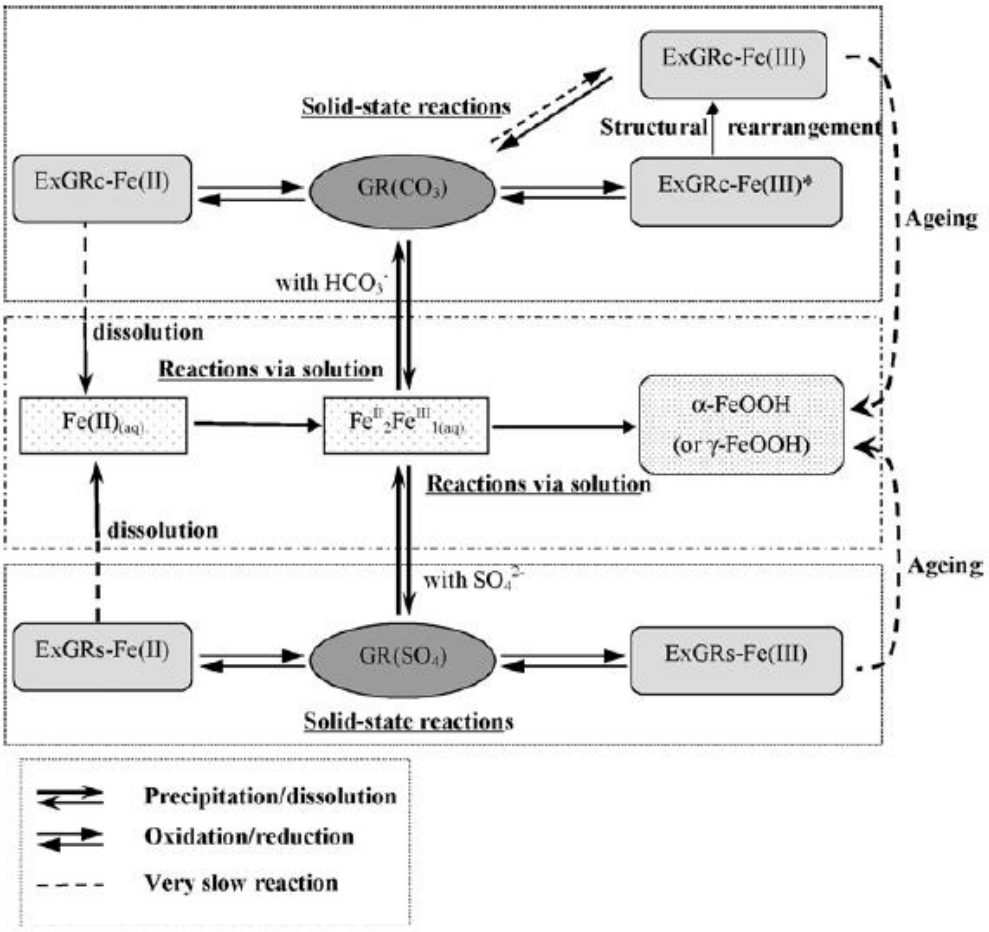

Figure 1.7. Routes to and from GR depend on many factors. Solid-state reactions, or topotactic changes that occur without dissolution and reorganization, are one pathway and can occur under certain conditions and often bear crystallographic relation to the former structure, such as in the "ferric" GR shown about. Dissolution/recrystallization is another pathway, and can result in a variety of different arrangements before reaching the end oxidation products, such as in the final transformation into goethite and lepidocrocite. Adapted from Antony et al., *Electrochimica Acta,* 2008. [47]

- The structure of the iron-oxydyroxide layers
- The oxidative state of the iron
- Overall material morphology on a micron and nanoscale.

A battery of non-destructive techniques must be used to tackle each of these questions. These can include X-ray diffraction (XRD), Mossbauer, X-ray photoelectric spectroscopy (XPS), Raman spectroscopy, UV-Vis spectroscopy, transmission electron microscopy (TEM) and X-ray absorbance spectroscopy (XAS).

1.3.1 X-Ray Diffraction (XRD)

XRD is a definitive characterization technique for solid state structure, and it can specify precisely the bond distances and structure of a material. Because green rust is a form of a layered double hydroxide, the XRD spectrum can be used to both measure layer spacing as well as the lattice of the layers. Indeed, XRD has been applied as a fingerprint tool for interpreting green rust species found in nature, or used as a key comparison to identify new synthetic GR types.[47,48]

Perhaps the most critical piece of information in an XRD pattern is the quantification of the d-spacing along the *c* axis; this low angle feature provides an indication of the size of the intercalated molecules. A very large d-spacing, for example, indicates the incorporation of larger anions. Typically GRs (natural and synthetic) possess d-spacings between 0.7 – 0.9 nm (Figure 1.8). Several recent publications have

developed new synthetic GRs with much larger d-spacings, incorporating large organic anions such as oxalate and lactate. The most bulky anion incorporated into the GR crystal structure are alkyl groups which result in an interlayer spacing of 4.2 nm.[31]

1.3.2 Mossbauer and Iron Oxidation State

Mossbauer absorption spectroscopy is a uniquely specific probe for the ^{57}Fe species. Noise or potential interference in the sample studied is reduced to near zero regardless of impurities in the material in question. This is especially useful with regard to natural minerals which are bound to have organic substances that might interfere with other methodologies. Unlike in XRD where different intercalants changed the low angle peaks, most green rusts have nearly identical Mossbauer spectrum. This is because bonding in the planes of the cationic Fe-O layer will remain mostly the same regardless of anion. Almost all green rust species have an easily identifiable doublet with both a large isomer shift (δ) and quadrupole splitting (QS), shown in Figure 1.9. Isomer shifts in this range are solely due to a Fe(II) species, while large QS values of this nature indicate a distortion in bonding.[49]

1.3.3 Raman Spectroscopy for Green Rust Identification

Raman spectroscopy can be used to characterize both the solid state structure and the molecular composition of green rust, and is among the most important tools used for studying green rusts. First used in 1991 to identify a “well-crystallized” material with a “gelatinous appearance,” it was not until 1997 that the exact peaks derived from

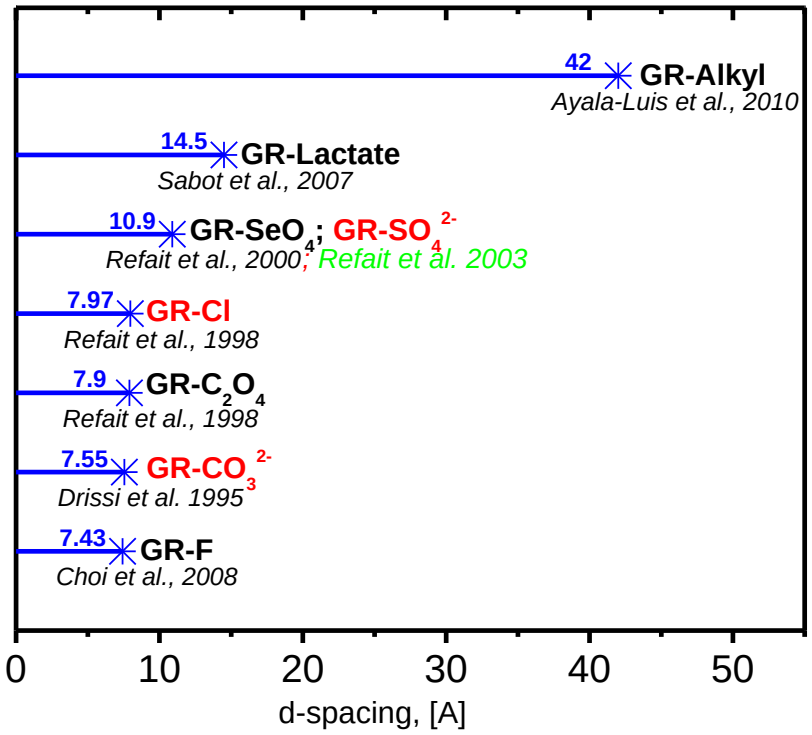

Figure 1.8. The range of intercalant size varies greatly, and especially so for the synthetic GRs. Collated d-spacings (blue text) are from a range of reported GRs with different intercalants. Red texts are GR types that can be found in nature, and the citation in green is an XRD spectrum from a natural source (note natural spectrum was recorded as 11.0 Å).

green rust were clearly identified. These are located at 427 and 518 cm^{-1}, corresponding to both Fe(II)- O and Fe(III)-O stretches, respectively (Figure 1.10a).[35,14] Thus the various ratios of these peaks provides corroboration as to the relative Iron(II) content of a material, and they are relatively insensitive to the anion. [35] In-situ Raman monitoring has also been applied in the field; it could detect GR formation due to marine corrosion

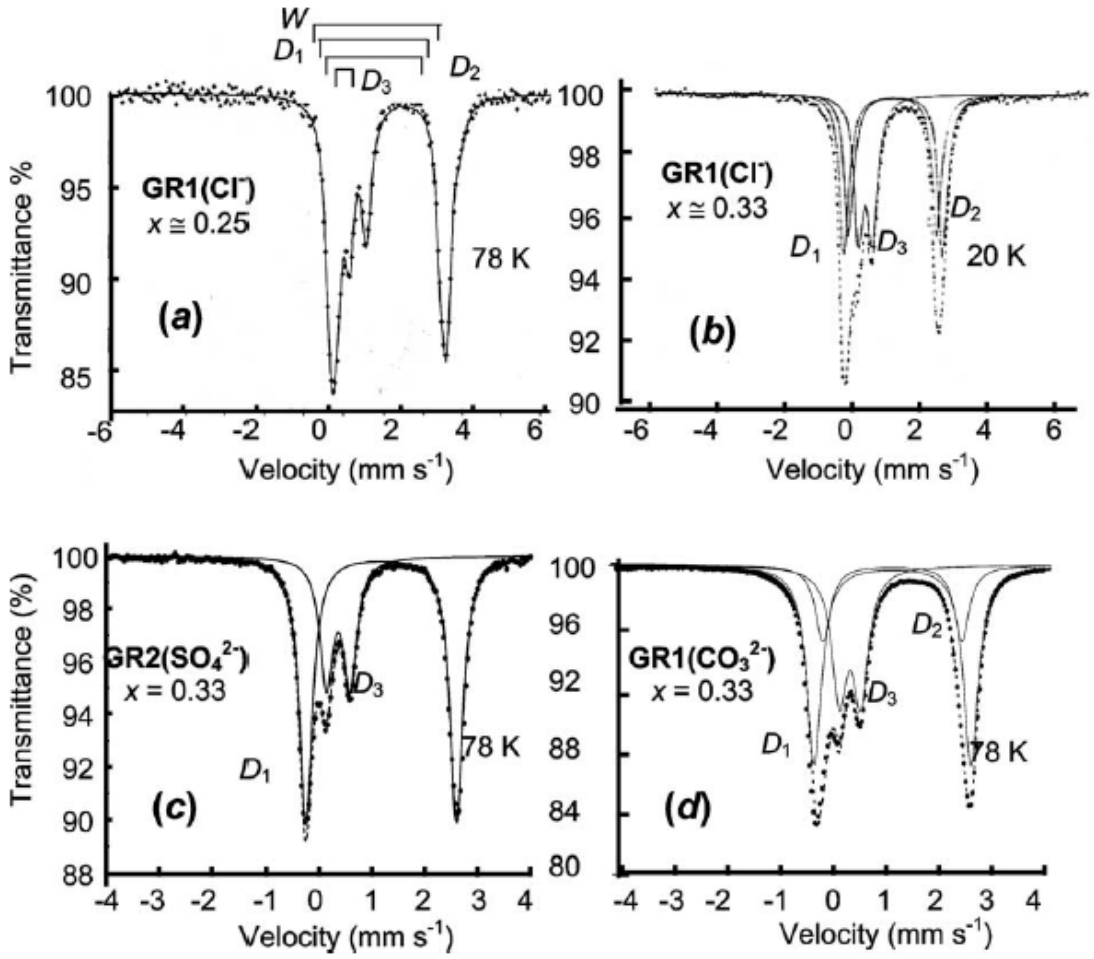

Figure 1.9. Intercalation of different anions does not perturb the bonding environment around iron in green rust. Mossbauer indicated relatively little change in peak structure between different anions. *x* is $(Fe^{III})/(Fe_{total})$, and measurements were taken at temperatures listed (78K for each anion). Adapted from Genin et al., *Solid State Sciences,* 2004. [50]

by sulfate-reducing bacteria, as well as the monitor the various iron species on the surface of steel.[17]

1.3.4 X-Ray Photoelectron Spectroscopy (XPS)

XPS is a surface characterization technique with many capabilities including multi-element surveys, single element high resolution analysis, and angle-dependent scans. Taken together these methods can allow for the top 5 nm of a material to be evaluated for metal composition and in some cases metal oxidation state. For GR, when care is taken to avoid oxidation of the sample, XPS analysis can be used to observe its mixed-valent state (Figure 1.10a) through the main Fe $2p_{3/2}$ XPS multiplet positions.[37]

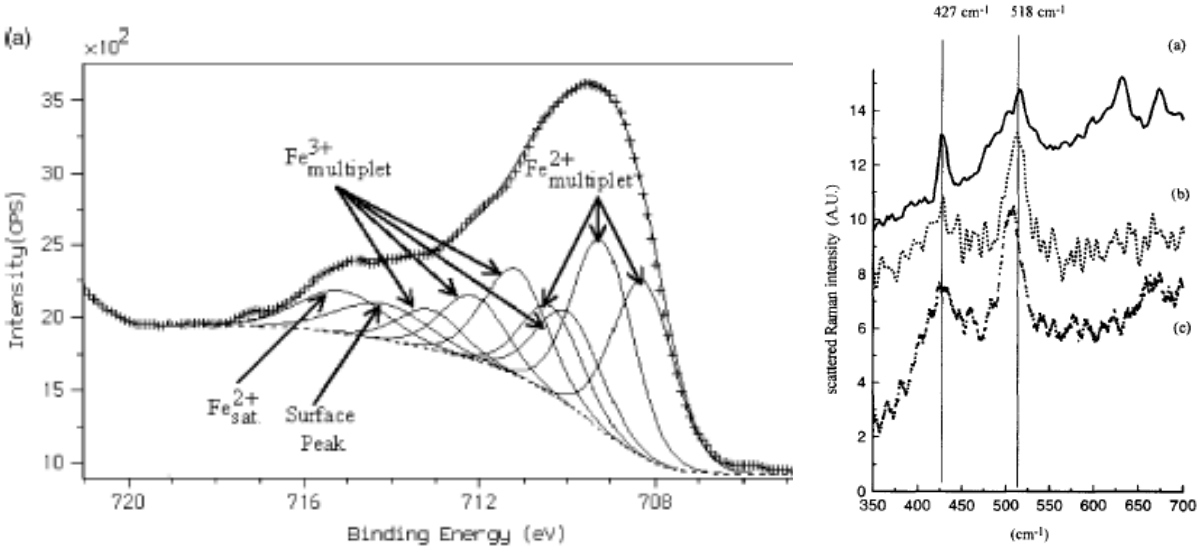

Figure 1.10. XPS and Raman spectroscopy are often used for GR identification. (a) GR XPS multiplets for Fe $2p_{3/2}$ show a mixed valent state with a predominance of Fe(II). Main Fe(II) multiplets are at 708.3, 709.2, and 710.4 eV. Similarly, (b) Raman peaks at 427 and 518 cm^{-1} are standard and consistent for GR. The top spectrum (a) is from a natural GR sample, the middle one (b) is GR-carbonate, and the bottom (c) is GR-chloride. Adapted from Mullet et al., *J. Solid State Chem.,* 2008[37] and Trolard et al., *Geochimica Et Cosmochimica Acta.,* 1997,[14] respectively.

1.3.5 Ultra-violet visible Spectroscopy

Absorption spectroscopy is an excellent tool for examining the electronic characteristics of a material, especially for those with striking visible colors such as green rusts. However, because of the fast oxidation of GR the green color can quickly disappear unless samples are sealed; additionally, synthetic and natural green rusts are not dispersed in water and often settle to the bottom of the solution (Figure 1.11).[24] For this reason, diffuse reflectance is the tool of choice.

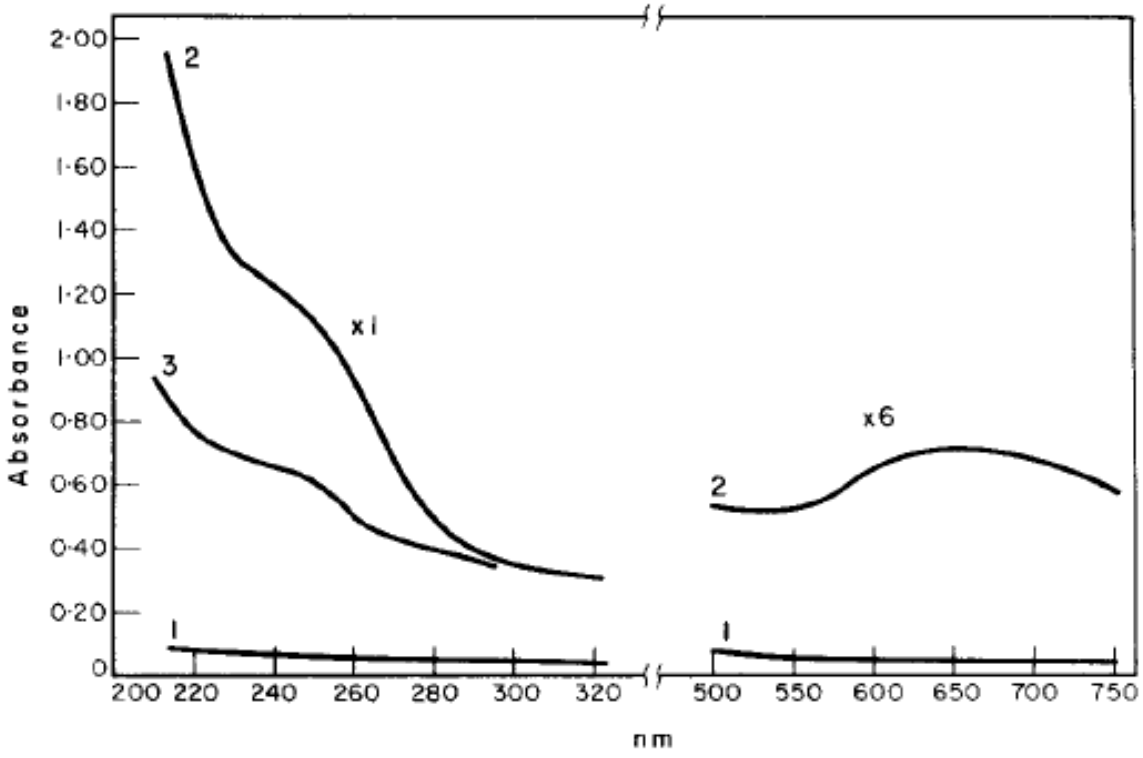

Figure 1.11. Absorption spectroscopy is only rarely applied to the insoluble and unstable green rusts. Misawa et al. shows a colorless solution (1) and gradual formation of the GR in aqueous solution (2); however, the intensity decreases as the material eventually forms a precipitate (3). Adapted from Misawa et al., *J. Inorg. Nucl. Chem.*, 1973.[24]

1.3.6 Electron Microscopies

Transmission electron microscopy (TEM) and scanning electron microscopy (SEM) are important imaging techniques in material science. In the case of green rusts, they provide researchers insights into the micron and nanoscale structure of the material. GRs can have either a rhombohedral or hexagonal crystal structure; typically they adopt a thin, plate-like hexagonal habit (Figure 1.12). These plates are strongly electron diffracting, and provide structural data comparable to that found through x-ray diffraction.[51] While high resolution imaging is possible, direct imaging of the d-spacing of these lattices has not yet been report. This may be due to the instability inherent in green rusts with respect to oxidation, which could lead to strong interactions with intense electron beams.

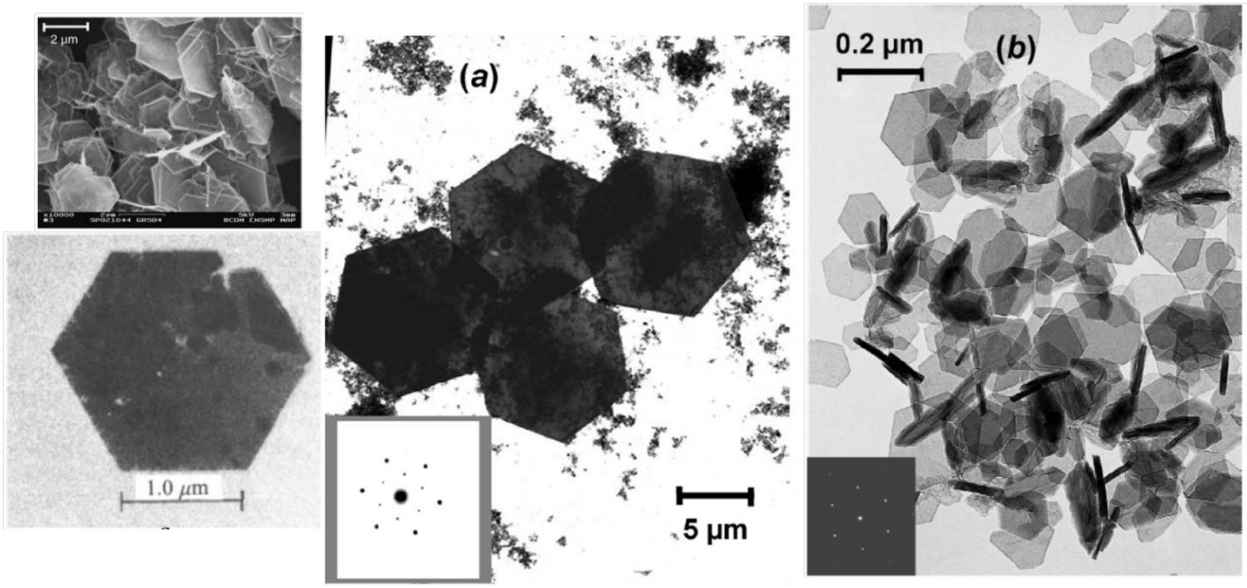

Figure 1.12. Micron-sized hexagonal platelets are the typical crystal habit of GR seen here by TEM. Adapted from Refait et al., *American Mineralogist,* 2003;[20] McGill et al., *Nature,* 1976;[51] Genin et al., *Solid State Sciences,* 2005,[28] respectively.

1.3.7 X-ray Absorption Spectroscopy (XAS)

XAS consists of two primary techniques: XANES (X-ray absorption near edge spectroscopy) and EXAFS (extended x-ray absorption fine structure). The former can characterize the oxidation state and electronic transitions in a solid state material while the latter is one of the few methods known for interrogating structure of the next-nearest neighbors in a crystal. Typical GR XANES spectra show GR situated between Fe(II)-bearing $FeCl_2$ and Fe(III)-bearing goethite (α-FeOOH), indicating a mixed valent state (Figure 1.13).[40] Further evidence can be seen from a broad peak between both Fe(II) and Fe(III) in the pre-edge region. Fe K-edge EXAFS information also provides valuable details about bond distances. Magnitude FT results for Fe-OH & Fe-Fe often lie at approximately 0.16 nm & 0.27 nm, respectively; actual interatomic distances are within 0.45 Å error from expected phase shifting in the data.[40,52,53]

1.4 Environmental remediation using green rusts

1.4.1 Dye remediation

Azo dyes are a class of hazardous contaminants that GR can react with. When disposed of, such compounds are chemically reactive contaminants (Figure 1.14) and potentially mutagenic.[54] Green rust can deactivate azo dyes rapidly, as observed by peak

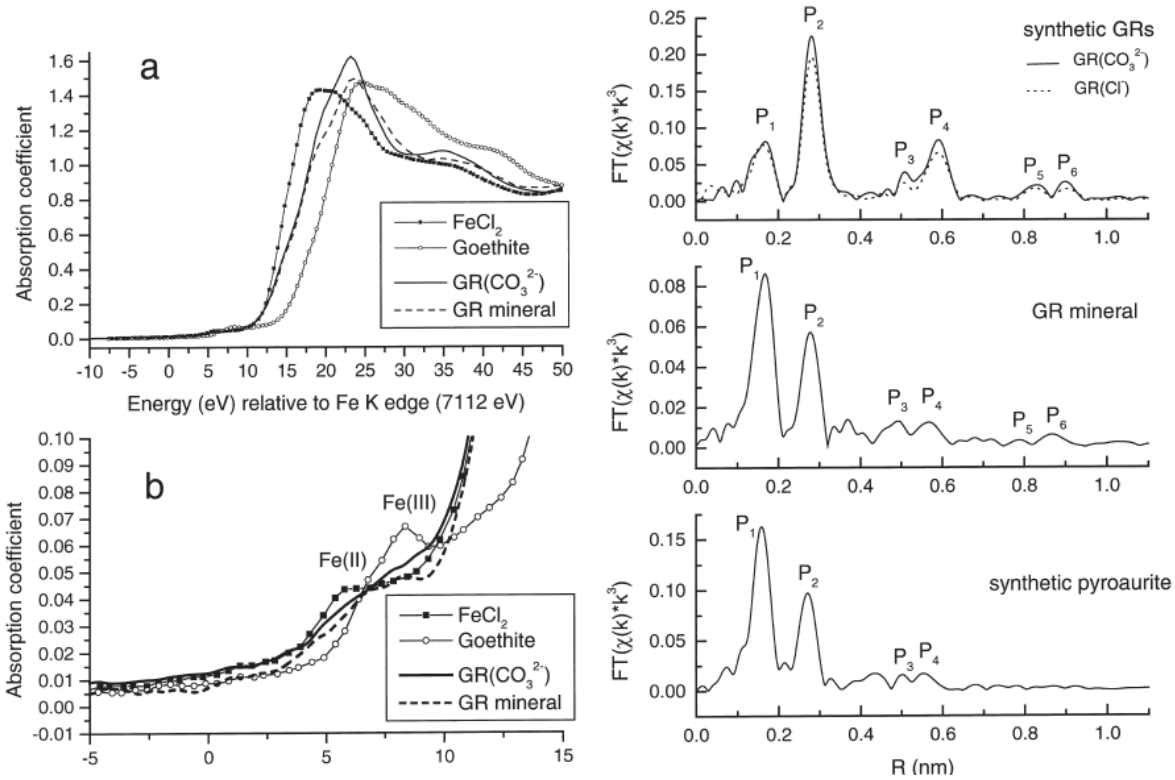

Figure 1.13. XAS information provides great insight into the bonding structure, oxidation state, and interatomic distances of green rust. Fe K edge XANES data shows green rust to be between iron chloride and goethite in oxidation, supporting a mixed-valent state. Fe K edge EXAFS information shows bonding distances for Fe-OH & Fe-Fe at approximately 0.16 nm & 0.27 nm, respectively. A common phase shift can affect the observed magnetite data; actual bond distances are within 0.45 Å of the peak maximum.[40,53,52] Adapted from Refait et al., *American Mineralogist,* 2001.[40]

loss via UV-Vis.[55] Subsequent mineralization afterwards via H_2O_2 resulted in 87% total organic carbon (TOC) removal within 60 minutes.

1.4.2 Arsenic

Arsenic is a class(I) non-threshold carcinogen responsible for a number of diseases or illnesses that will be addressed in a later chapter.[56] Green rust has been

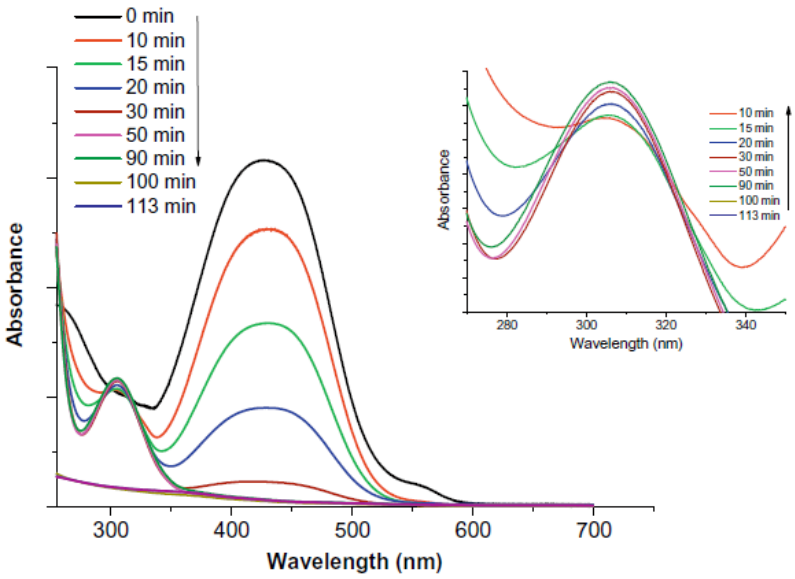

Figure 1.14. Green rust can decolor a dye solution in minutes to hours, depending on concentration. Dye peak loss is quickly observed via UV-Vis. Lack of TOC decay (not shown) indicates this is the result of conversion into inactive, colorless transition compounds rather than permanent sorption, however applying the oxidant H_2O_2 afterwards results in 87% TOC removal within 60 minutes. Adapted from Kone et al., *Chemosphere,* 2009. [55]

shown by Randall *et. al.* to adsorb and remediate large levels of As (ppm) from solution during GR synthesis (Figure 1.15).[57] Also interesting to note is the lack of reduction to As(III) and persistence of its +5 state, reinforcing the complex nature of GR chemistry.

1.4.3 Nitrate reduction

Nitrate contaminates are a serious health threat to both land and sea environments where an overdose can lead to "blue-baby" syndrome in children with potentially fatal effects.[3] Using GR-Fluoride, green rust produced via an air oxidation

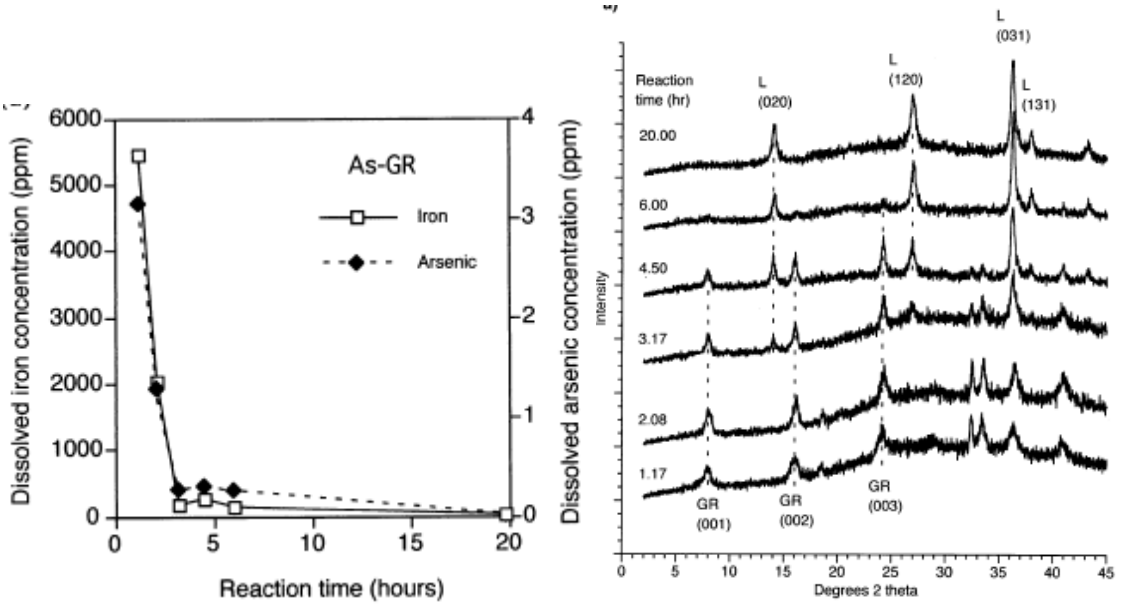

Figure 1.15. Green rust can adsorb arsenic. Green Rust sulfate was produced in the presence of As by Randall et al. [57] via Schwertmann and Fechter's oxidative coprecipitation method. [58] Arsenic eventually could not be detected, and the crystal structures present gradually changed from GR to lepidocrocite. Adapted from Randall et al., *Geochimica Et Cosmochimica Acta,* 2001. [57]

method by Refait *et. al.* was able to remove nitrate from solution (Figure 1.16), and could be applied over a range of basic pH (7.8-11).[3] Of note is that nitrate was removed from solution by both reduction to nitrite and ammonium as well as by incorporation via anion-exchange with fluoride into the GR crystal structure.

1.4.4 Uranium

One interesting feature of green rust is its ability to reduce and form UO_2 nanoparticles; this is pertinent in discovering how natural processes effectively mediate

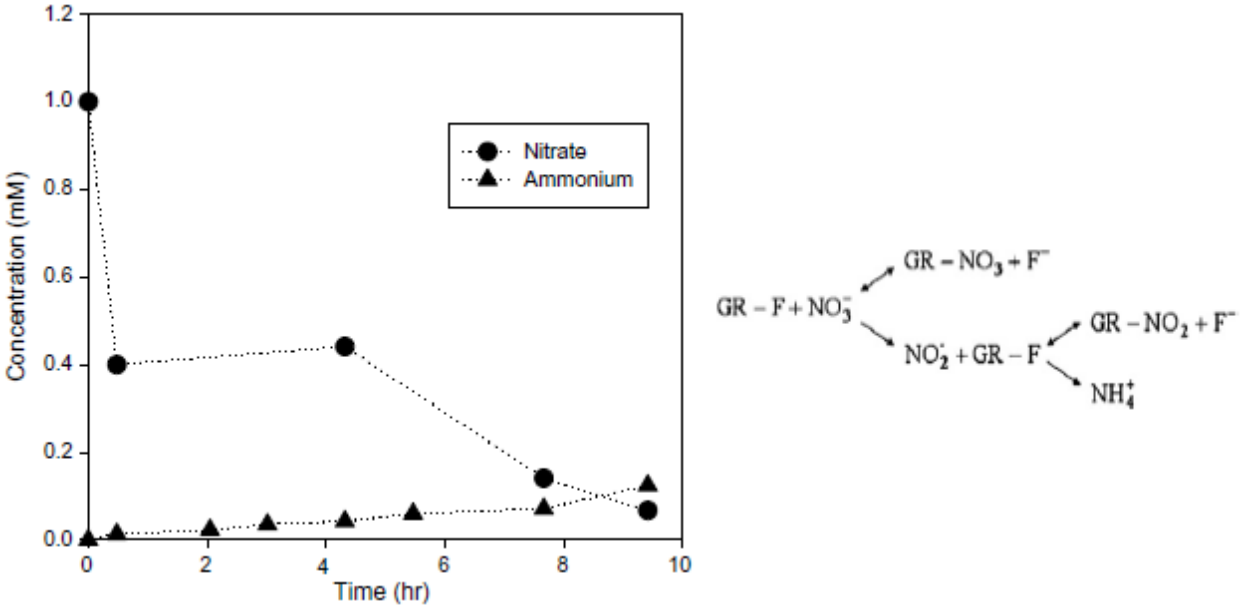

Figure 1.16. Green rust can remove nitrate from solution. Lack of equivalent ammonium concentration is due to incorporation of nitrate/nitrite via anion exchange into the GR crystal structure. Adapted from Choi et al., *Chemosphere,* 2008. [3]

such hazardous materials (Figure 1.17).[5] As U^{VI} is reduced to U^{IV}, green rust is concurrently oxidized to phases such as ferrihydrite, goethite, akaganeite (β-FeOOH), lepidocrocite, maghemite (γ-Fe_2O_3), or magnetite (Fe_3O_4). In the cited case magnetite was claimed to be the oxidation product.

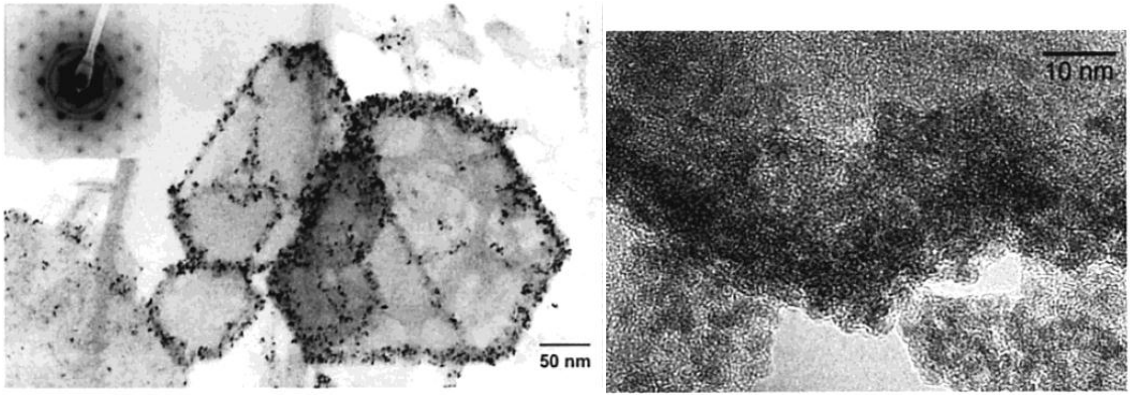

Figure 1.17. Green Rust may have use for radioactive contaminant fate and transport applications. Uranium (UO_2) nanoparticles nucleate on the surface of GR from insoluble U(IV). Adapted from O'Loughlin et al., *Environmental Science & Technology,* 2003. [5]

Chapter 2 Sulfide Green Rust on Iron Nanoparticle Scaffolds

This chapter details the synthesis of a reactive iron-sulfide green rust from iron oxide nanocrystals. Simple thiol-containing amines allowed for the facile reduction of the surface of iron oxides, forming a brilliant green suspension of nanocrystals that were easily dispersed in polar solvents and water. Electron microscopy and x-ray diffraction revealed two phases present in the nanocrystal products apparently arranged in a core-shell configuration; the core remained identical to the starting iron oxide. The treatment by the cysteamine yielded a surface which consisted of a layered iron-sulfide that resembled iron-oxyhydroxide green rusts. This previously unidentified phase was evaluated using X-ray diffraction, Mossbauer spectroscopy, vibrational spectroscopies and XANES/EXAFS. We verified the reactivity of the nanocrystals by applying them to the removal of a common but potentially mutagenic azo dye, Orange II.

2.1 Introduction

Reactive nanoparticles, particularly formed from reduced iron phases, have found wide application in environmental remediation. The most reactive of these are the fully reduced 'zero valent iron' nanoparticles (NZVI); as the iron oxidizes in water these materials produce potent oxidants that can remove dyes from water, dechlorinate halogenated contaminants, and other things.[59,60] Field trials of these materials have illustrated the great promise of the in-situ alternative to the pump-and-treat paradigm for treating heavily contaminated water. Alternatively, high surface area green rusts have also been applied as reactive sorbents for the removal of nitrate, disinfection

byproducts, and radioactive wastes such as technetium.[3,4,6] These materials also have high levels of iron(II) in their iron-oxyhydroxide layers and in addition offer the potential for intercalating anionic contaminants.[61,62,63] Finally, interest in reduced iron oxides, such as magnetite particles, have also shown environmental remediation capabilities, such as in the dechlorination of carbon tetrachloride,[64,65,66,67] activated sulfate oxidation,[68] uranium sorption,[69] and more.[70,71] Both of these classes of material illustrate the value of iron(II) as a reactive agent on nanoparticle surfaces.

The synthetic approach to iron(II)-rich nanoparticles generally follows one of two routes. In the case of zero valent iron nanoparticles, iron(III) salts are reduced by borohydride in water under vigorous mixing. Alternatively, reduced iron oxide particles are formed in coprecipitation routes where iron salts are moderately reduced by ammonia at temperatures between 50 – 60° C. Green rusts are produced in a variety of ways, including a similar coprecipitation of iron salts or bioreduction of oxidized iron.[26,72] In all cases, the final nanoparticles are generally not size-controlled or monodisperse. Additionally they are formed in their most reactive state. This presents challenges for handling and storage, not to mention the poor control over particle size and morphology from the aqueous synthesis. Unfortunately, routes to more monodisperse nanocrystals occur at high temperatures in organic solutions under conditions that do not easily favor the reductive environments necessary to form iron(II).[73]

The goal of this work was to examine the possibility of forming reduced iron (II) using an iron oxide nanocrystal as a starting material. Organic thiols for example are known to be able to reduce iron(III) though the reactions cannot proceed in water. If this could be applied to highly uniform nanoscale iron oxides, it would represent a novel approach to forming reactive iron(II)-rich nanoparticles. Additionally, it could be possibly useful as a relatively inert nanocrystal powder could be actuated at the point of use into a reactive material thereby minimizing the challenges of storage. If the reduction was only at the surface, then the magnetic and oxidized core would allow for magnetic separation to be used to remove and possibly recycle materials. Finally, the treatment could in principle be applied to spent particles allowing for their reuse in an environmental remediation problem.

2.2 Results and discussion

A novel nanoscale iron sulfide compound, termed here "sulfide green rust" or nano sGR, was formed by treating nanocrystalline magnetite with cysteamine. Iron-thiol chemistry is central to this reaction, specifically the reaction of sulfur from the cysteamine with iron from the nanocrystalline iron oxide. Similar chemistry has been observed from bulk starting materials, but the product was not water soluble or green.[74] Briefly, an alcoholic solution of cysteamine hydrochloride, a known metal ion scavenger, was added to an organic dispersion of nanocrystalline iron oxide.[75] After two to three hours of mixing in a sealed vial, a green color was observed in the alcoholic phase and the organic phase was nearly colorless. The optical absorbance of the aqueous sample

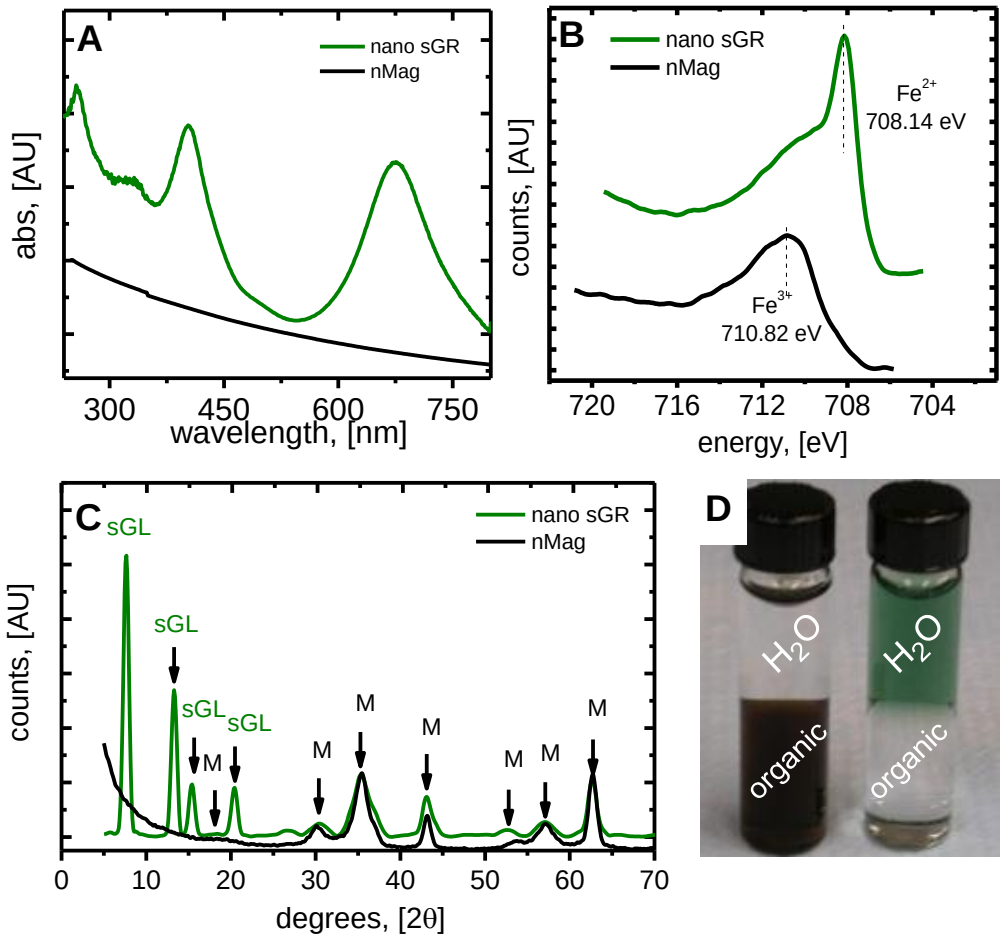

Figure 2.1. The sulfide green rust, or "sGR," was easily formed using an intercalated cysteamine-HCl and nanomagnetite precursor. Nanomagnetite was initially prepared in the organic phase and brown (a, black line) due to a lack of absorbance peaks in the UV-Vis. After the sulfide green rust synthesis, a transfer to the aqueous phase (d) and a brilliant green color (a, green line) was readily apparent; major optical absorbance peaks were present at 256, 400, and 675 nm. An increase of Fe^{2+} (b) coincided from the synthesis as observed by Fe $2p_{3/2}$ XPS. This reduced iron state was the result of a reaction with sulfur in the cysteamine with nanomagnetite, producing a unique XRD spectrum with low 2θ peaks (c). Magnetite persists after the reaction, as the diffraction pattern for both the sGR and nanomagnetite are visible.

showed two peaks at 400 and 675 nm (Figure 2.1A). Also, during this process the brownish-black nanocrystalline magnetite was transferred from the organic phase to the aqueous phase where it appeared green (Figure 2.1D).

2.2.1 Proposed structure

A variety of structural and molecular studies, described in the following sections, have revealed that the cysteamine treatment forms an iron-sulfur phase on the nanocrystal surfaces as summarized in scheme 2.1. In brief, when iron oxide is treated with cysteamine in alcoholic solvents, surface available iron(III) will react forming an iron-sulfide phase rich in iron(II). This is analogous to how green rusts form where reduced iron oxide layers intercalate basic anions; for that reason, reason we term the product a 'sulfide green-rust'. Here, cysteamine is the intercalant leading to low angle scattering peaks reflective of the relatively large distance (d ~ 11.49 Å) between iron-sulfide planes. Scheme 2.1B illustrates the proposed structure which is based on those of natural green rusts. We note that the intercalation of two cysteamines accounts well for the specific low angle d-spacing observed in X-ray diffraction.[10]

2.2.2 Physical and spectroscopic properties

An important feature of the final product is that the iron is reduced. The green color of the product (Figure 2.1A) suggests the presence of iron (II) and this was verified by X-ray photoelectron spectroscopy (XPS).[76,77,78] Figure 2.1B shows the Fe $2p_{3/2}$ XPS spectra of the starting iron oxide compared to the green product. A clear change in the iron oxidation state is evident: the iron peak position shifts from 710.82 eV which is iron

(III) to 708.14 eV which is iron (II).[37,79,80] These XPS results are not surprising, since cysteamine is a metal scavenger that can reduce iron(III) to iron(II)

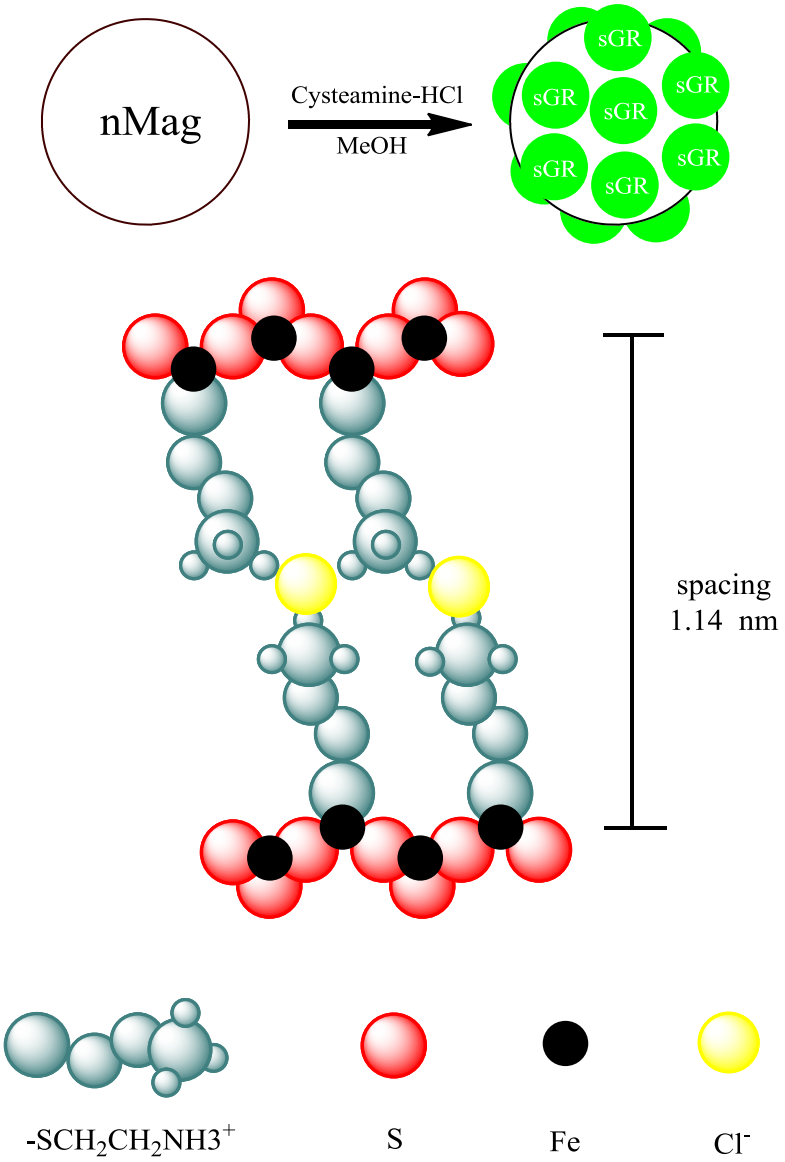

Scheme 2.1. Schematic representation of the described reaction and sulfide green rust crystal structure.

in water.[81, 78] Previous studies have shown this to occur via electron transfer from the sulfur to the iron.[78]

X-ray diffraction indicated the presence of two distinct crystallographic phases in the green product (Figure 2.1C). The data clearly shows that iron oxide is present both before and after the treatment. Because of the close similarity in scattering it is not straightforward to distinguish between magnetite and maghemite starting materials, a fact compounded by the peak broadening in these nanoscale samples.[82,83] After treatment with the cysteamine, new diffraction peaks are clearly visible at 7.69, 13.2, 15.37 and 20.21 degrees. The new pattern did not match to any known phase in either JADE or online RRUFF crystallographic databases. The strongest feature of these new peaks was a low 2θ peak at 7.69 degrees corresponding to a 11.4 Å d-spacing. Iron-containing clays such as those found in loess soils (e.g. smecite group) frequently are identified by these low angle peaks which arise from the Fe-rich layers that intercalate anions as large as 10 Å. [84] Of particular interest are green rusts which may incorporate large organic anions such as lactates, giving rise to d-spacings in excess of 10 Å (e.g. 14.8 nm and 44.4 Å, respectively).[10, 48]

2.2.3 Nanoparticle association

We evaluated whether this new phase was physically associated with the nanocrystalline magnetite using both electron microscopy and magnetic separation. Low magnification images show that nanocrystals are present in the green product solutions, and this is consistent with the x-ray diffraction of the solid product (Figures

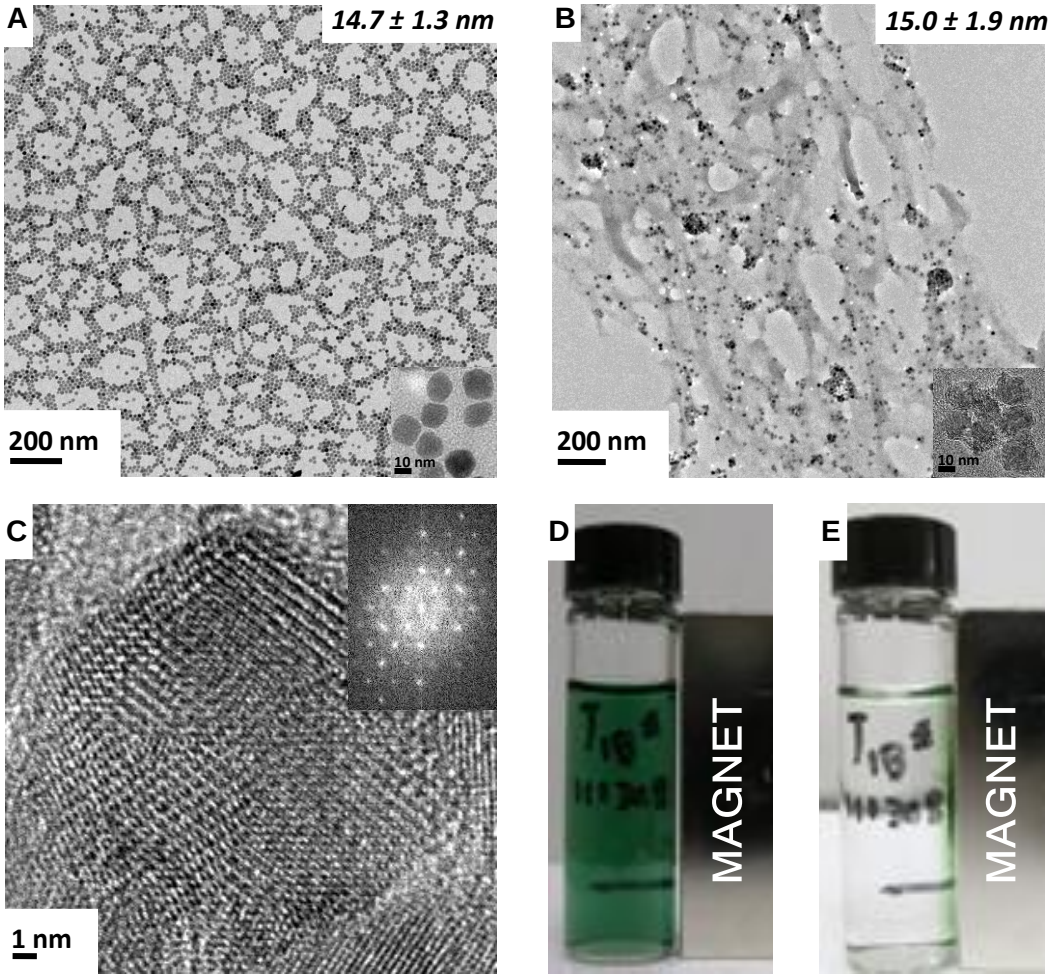

Figure 2.2. The sulfide green rust was associated with unreacted nanomagnetite, and the physical properties of the nanomagnetite were retained. Nanoparticle size was conserved as seen by TEM before (a) and after (b) the sGR synthesis, with size changing within standard deviation from 14.7 ± 1.3 to 15.0 ± 1.9 nm. Over 1000 particles were counted to be statistically accurate. Typical nanomagnetite nanoparticles (a, inset) obtained a more corroded particle surface (b, inset) after the reaction. High resolution imaging (c) and related FFT images (c,inset) confirmed the existence of a larger d-spacing that corroborates with X-ray diffraction data. Nanomagnetite's magnetite properties were preserved, as a hand-held neodymium magnet was observed to remove the nano sGR over 24 hrs (d,e).

Table 2.1. FFT d-spacing calculations.

Ave Distance from center, nm^{-1}	[Pixels/nm]	FFT d-spacings, [nm]	XRD d-spacings, [nm]	Intensity, [%]
22.65	25.95	1.146	1.148	100
40.08	25.95	0.648	0.670	86.7
60.63	25.95	0.428	0.437	70.1

2.2A,B). Analysis of over a thousand particles yields a particle size distribution very similar to the starting product; however, the surfaces of cysteamine treated particles appear more heterogeneous under higher magnification (Figures 2.2A,B, insets). High resolution imaging and related FFT images (Figure 2.2C; Table 2.1) of the overall particle confirmed the coincidence of a large d-spacing and the iron oxide crystal phase, corroborating the X-ray diffraction. Analytical electron microscopy of this product also revealed sulfur to be present at the nanocrystal interface (Figure 2.3). Additionally, the green product could be removed from solution using a hand-held neodymium magnet (Figure 2.2D,E). Since iron clays are not generally magnetic, this behavior is consistent with a structural model in which the cysteamine reacts with surface iron, resulting in a new phase that remains physically associated with the nanocrystal cores.[85]

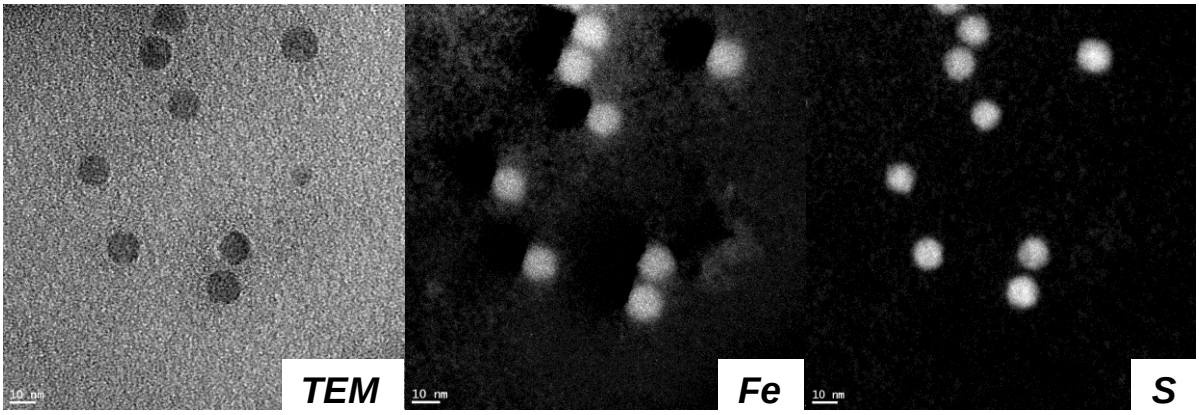

Figure 2.3. GIF TEM elemental mapping demonstrates that Fe and S atoms were concentrated mainly at the particle.

2.2.4 XAS and Mossbauer confirmation

To better evaluate the physical structure associated the modified iron oxides, we employed Mössbauer spectroscopy to examine the iron environments. The signature spectrum of nanocrystalline magnetite was observed in Figure 2.4A, illustrating two main sextets related to Fe^{2+} and Fe^{3+} below the Verwey transition.[82] A separate phase consisting of two doublets occur near the center of the spectrum (Figure 2.4B). Mössbauer isomer shifts (δ) of 0.147 mm/sec show close matches to the FeS_2 pyrite dimorph marcasite (δ =0.149 mm/sec), respectively, as well as a close match to iron dithiolates (δ = 0.15 mm/sec). [86,87] Quadrupole splitting (QS) of 1.98 mm/sec was much higher than literature values for marcasite (QS = 0.504); this could be due to distortion caused by the large organic ligand in the crystal structure or possibly a closer match to the iron dithiolate (QS = 1.98). The second doublet observed for the green product was assigned to an oxidized Fe(III) derived from the iron-sulfur phase. Neither of these peaks have either the isomer shifts or quadrupole splitting characteristic of either synthetic and natural green rusts (Figure 2.4C).[88] Conventional green rust has iron-oxygen layers; our Mössbauer data suggests that in this structure iron is bonded predominantly to sulfur.

Additional confirmation of iron-sulfur bonding can be seen via Fe K-edge X-ray absorption measurements (Figure 2.5A). A critical first step for analyzing multiple phases in EXAFS data is to acquire calibration materials which are pure single phases. This was straightforward for the iron oxide component as the unreacted

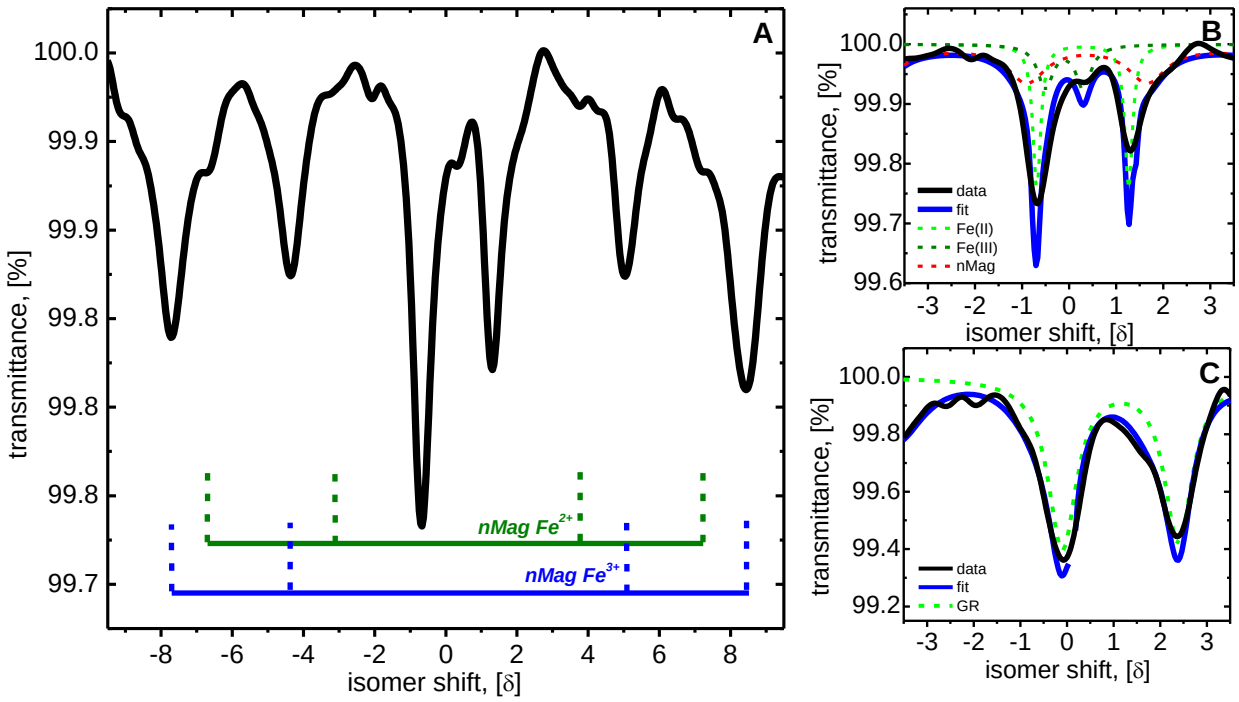

Figure 2.4. Both sulfide green rust and magnetite were still present after complexation. The 77K Mössbauer spectrum of nano sGR (a) illustrates two phases: the multiple overlapping sextets related to magnetite and two doublets assigned to sGR. Magnetite's two resulting sextets are indicative of Fe^{2+} and Fe^{3+} typical of magnetite below the Verwey transition. Isomer shifts (δ) of 0.147 mm/sec for the sGR was similar to iron sulfide minerals (b) such the Fe(II) in bulk FeS_2 marcasite (δ = 0.149 mm/sec), and certain iron dithiolates (δ = 0.15 mm/sec); quadrupole splitting (QS) of 1.98 mm/sec for the sGR was more like that of Samples of GR-Cl were also were prepared and measured (c) for comparison. Lack of the characteristic large isomer shift (δ =1.1) and quadrupole splitting (QS =2.2) observed in the GR-Cl confirmed that our sGR had a unique crystal structure and was not a classical green rust.

nanocrystalline iron oxide was readily available. However, to form the iron-sulfur clay phase required that we develop a reaction that mimicked our cysteamine treatment without the nanocrystals. Towards that end, we found that if we treated the precursor

to the nanocrystal, iron oleate, with cysteamine in methanol it was possible to generate a green product with identical X-ray diffraction features to that seen in Figure 2.1. Using this pure phase it was possible to assign the features in the X-ray absorption spectrum (Figure 2.5).

Shown compared to the data is a fit that assumes 2.24 Å for Fe-S, 3.40 Å for Fe-Fe, and 1.86 Å Fe-O with an excellent R-factor (0.03; 0.05 is the maximum allowed value for a good fit). Peaks found at 2.29 Å and 3.41 Å using our control phase further confirm our model with an improved fit of 0.01 (Figure 2.5B). Contributions of Fe-S and Fe-Fe are from the sulfide green rust, with the additions of Fe-O generated from nanocrystalline iron oxide (Table 2.2). For comparison, marcasite, the compound which matched well to the Mössbauer data, was run on EXAFS with strikingly similar results for Fe-S (2.26 Å) and Fe-Fe (3.82 Å) distances; also we note that the second phase matched very closely to magnetite, with a bulk Fe-O bond distance of 1.89 Å. Conversely, fits for other green iron complexes with hypothetical Fe-Cl or Fe-O bonds were poor; visual inspection of XANES data also suggests a better match to Fe-S (Figure 2.5C).

Taken together the data indicate that the cysteamine treatment produces a clay-like iron-sulfide material at the nanocrystal interface (Scheme 2.1). It is termed here 'sulfide green rust' or sGR so as to distinguish it from green rusts that possess iron-oxygen frameworks. The material is a layered structure with alternating planes of marcasite-like Fe centers that intercalate cysteamine molecules. Simple energy minimization exercises via ChemDraw (not shown) also found that two cysteamines

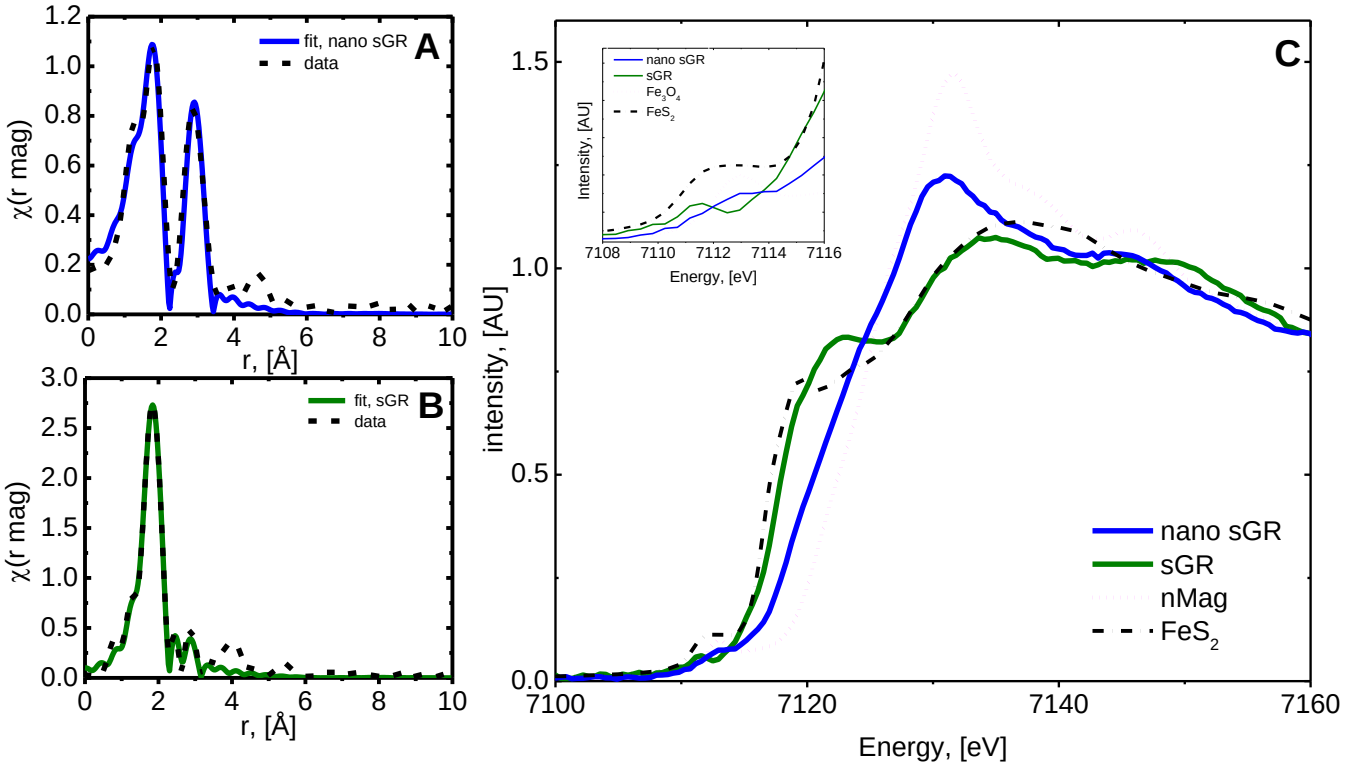

Figure 2.5. The sulfide green rust was composed of Fe-S bonds similar to the iron sulfide mineral, marcasite. Fe K-edge EXAFS magnitude FT data (a) demonstrated both sulfur and oxygen atoms bound to iron. Fitting included contributions of Fe-S at 2.24 Å (bulk marcasite FeS_2: 2.26 Å), Fe-Fe at 3.41 Å (bulk marcasite FeS_2: 3.82 Å), and Fe-O at 1.86 Å (magnetite Fe_3O_4: 1.89 Å) respectively, with a good R-factor fit of 0.03. Control experiments (b) were also conducted on a homogenous sample synthesized from dissolved iron, with contributions only from sulfur resulting; the atomic distances for Fe-S and Fe-Fe were 2.29 Å and 3.41 Å, respectively (see Supporting Information for details). Fe K-edge XANES spectra of the sGR (c) compared standard compounds containing Fe in various oxidation states and geometries, further corroborated a good match for Fe-S bonding, and indicated a general increase in Fe(II) from precursor nMag levels (c, inset).

stacked as shown provide a d-spacing comparable to that observed. This chemistry occurs at the surface of the nanomagnetite and enriches the material in reactive iron(II).

Table2.2. Fit parameters for the Fe k –edge fit of the nano sGR.

Sample info	*Paths*	*Bond length R, (ang)*	*Coordination Number (n)*	*Deby Waller Factor (ss)*	*Energy Shift (ev)*
sGR/nMag	Fe-S	2.24 ± 0.02	3.4 ± 0.6	0.008	-7.9 ± 2.9
k = 2.8 – 11 $Å^{-1}$	Fe-Fe	3.40 ± 0.03	5.9 ± 2.7	0.01 ± 0.005	
r = 1.1 – 3.3 Å	Fe-O	1.86 ± 0.07	1.5 ± 0.7	0.008	

Such a feature combined with the ability to recover the materials via magnetic separations suggests some promise as agents for environmental remediation.

2.2.6 Potential Applications

To demonstrate feasibility for potential water purification purposes, we compared nano sGR against polymer coated water-soluble nanomagnetite for the chemical degradation of a water soluble dye. As a model system we used the potential mutagen Orange II which has an azo functional group used in GR studies as a benchmark

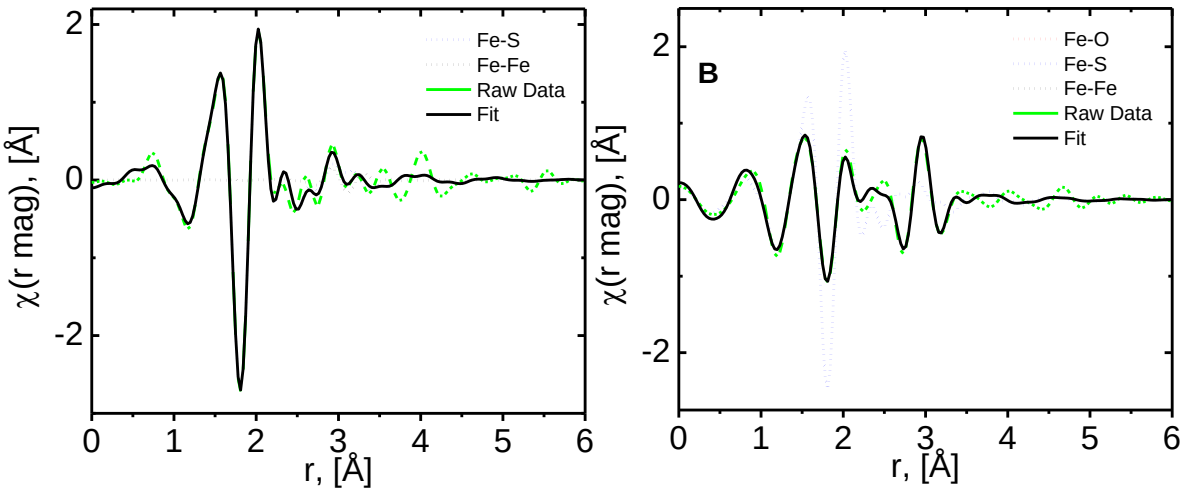

Figure 2.6. Fitting paths of the sGR (a) and the sGR/nMag (b) used for plotting radial distances in EXAFS fit.

Table 2.3. Fit parameters for the Fe k –edge fit of the bulk sGR.

Sample Size	*Paths*	*Bond length R, (Å)*	*Coordination number, (n)*	*Debye Waller factor, (ss)*	*Energy shift, (eV)*
sGR	Fe-S	2.29 ± 0.01	5.1 ± 0.4	0.004 ± 0.001	2.26 ± 0.93
k = 3.3 – 11 Å	Fe-Fe	3.41 ± 0.05	0.7 ± 0.5	0.004 ± 0.001	
r = 1.1 – 3.6 Å					

for remediation of organic contaminants.[55] Nano sGR quickly remediated the dye as measured by the disappearance of key absorbance features (Figure 2.6A). After

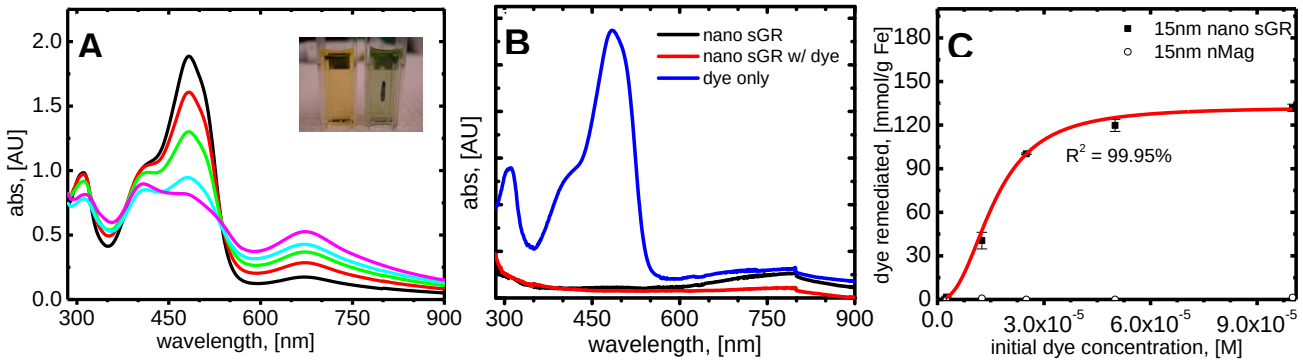

Figure 2.7. Sulfide green rust has potential for use. Remediation of an azo dye was observed via UV-Vis with fast reaction rates (a) also observable to the naked eye (a, inset). Controls tested the sample filtrate after passing through a 0.22µm PES membrane filter (b); no color was present in the samples after each filtration. Close to 100% removal can be achieved consistently (c), with a ratio of 22.46 dye molecules removed per Fe atom.

filtration through a 0.22 PES µm syringe membrane filter, all of the green material and dye was removed from the solution as observed via UV-Vis analysis (Figure 2.6B). Perhaps due to the extent of iron(III) reduced in the new material, sGR performed

consistently well against the water soluble nanomagnetite. 4.45×10^{-6} M of iron remediated nearly 1.0×10^{-4} M of dye resulting in about a 22.46 dye/Fe M ratio, and accounting for only surface iron would improve this ratio. There was no observable change in the nanocrystalline magnetite as indicated by the absorbance of the solution. Additionally, longer term studies were undertaken to demonstrate reaction kinetics and observe any possible desorption over time (Figure 2.8).

2.3 Conclusions

A historically difficult-to-characterize green iron sulfide can be synthesized around nanomagnetite cores. EXAFS and Mössbauer analyses both specifically confirm the existence of a Fe-S bond, and XRD identifies it as dissimilar from anything in the literature. Synthesis of the material is simple, fast, and utilizes the common organothiol cysteamine; the result is material with reactive properties due to a high iron(II) content. The sulfide GR is associated with the nanoparticle, making it possible for the magnetite to serve as a "scaffold" for reactive chemistry. Potential applications for the material match well with other reactive Fe^{2+} iron compounds, including fast dye sorption. This enhanced reactivity suggests a useful material, perhaps including other typical iron sulfide applications such as corrosion alleviation, catalysis, or hydrotreating.[89,90]

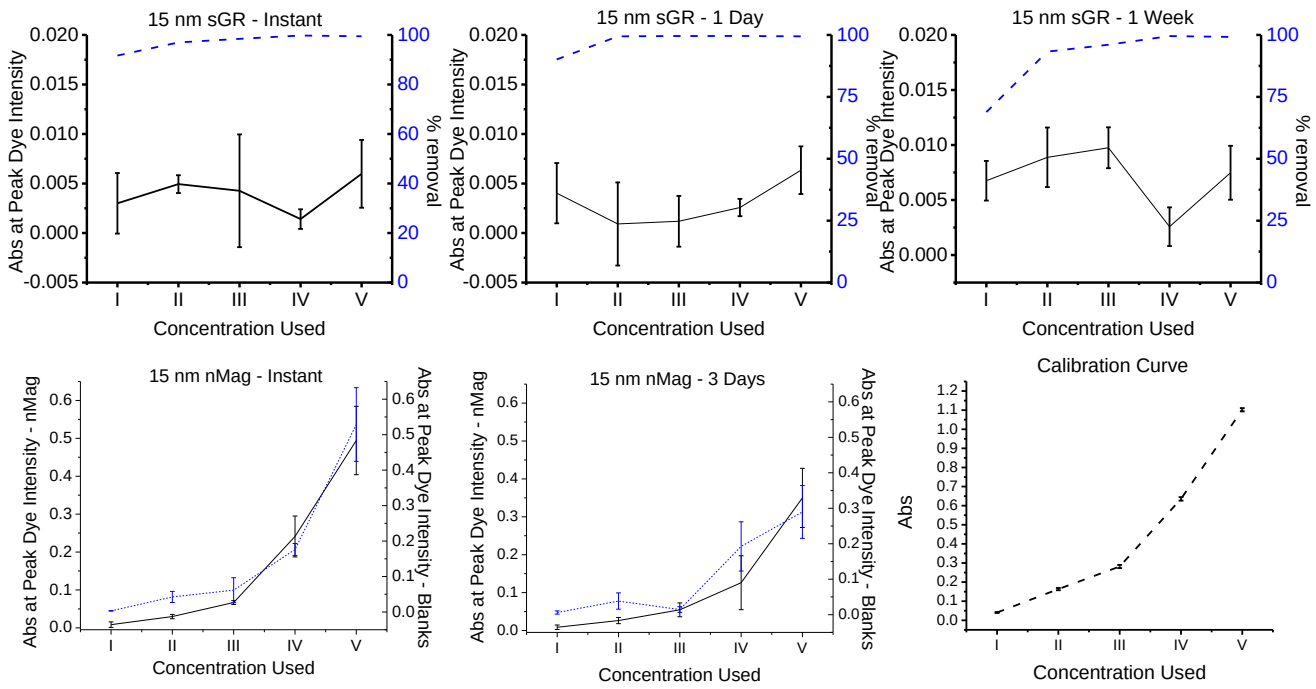

Figure 2.8. All sGR samples show near zero values for Orange II's main peak of 485 nm (*top*), regardless of the time allowed for possible desorption of the dye. Meanwhile, in comparison, the water-soluble nMag did not show any significant removal characteristics (*bottom*). Dye removal was also completed before measurement by UV-Vis. Dye concentrations I-V are between 2.5 x 10^{-6} and 1.0 x 10^{-4} M, and a calibration curve is provided (*bottom right*).

2.4 Methods and materials

Nanomagnetite synthesis. Iron oxide nanocrystals were made through established literature methods that form crystalline iron oxide through the thermal decomposition (T=320 ^{o}C) of iron carboxylate intermediates in mixtures of oleic acid (OA) and octadecene (ODE).[91] The resulting solutions were provided in hexanes and appear dark brown to reddish depending on the iron concentration and reaction conditions. These iron oxide nanocrystal solutions were purified to remove unreacted

oleic acid and other by-products of the nanocrystal formation reaction. Using an autopipette (Eppendorf), 4 ml of the solutions were transferred into a 50 ml centrifuge vial; 4 mL each of methanol then acetone (EMD, 99.9 %; EMD, 99.8 %) were added and the resulting suspension centrifuged (Thermoscientific Sorvall Legend RT+ Centrifuge) at 4,500 rpm for 30 min. This resulted in a dark brown or black pellet along with a clear or sometimes pale yellow supernatant; in some cases, this process was repeated to ensure the complete removal of any impurities. After disposing of the supernatant, the pellet was redispersed again in 4 ml of hexane (Fisher, 99.8 %); dispersion was readily observed after shaking the tube with a Scientific Industries Vortex Genie 2-T vial shaker at the lowest setting for 10 minutes. This yielded a clear and brownish or red solution which can be subjected to several more centrifugation and redispersion cycles. The purification process was generally complete once a clear supernatant was observed. In the final purification step, the nanoparticle pellet was redispersed in ODE (Sigma, 90%) as solvent. Brief probe sonication (Dr.Hielscher Up100h Ultrasonic Processor) for around 1-3 seconds may be required to help solubilize the magnetite pellet in ODE.

Sulfide green rust reaction. 0.56 mL of the nanomagnetite solution in hexanes was dispensed into a 2 mL centrifuge vial. Solvent was redispersed in ODE to prevent evaporation during synthesis, usually aided by brief bath sonication (FS6 sonicator from Fischer Scientific). Next, 0.44 ml of a 2.0 M solution of aminoethanethiol*HCl (Sigma, 98 %) in methanol (EMD, 99.8 %) was added to the reaction vial to obtain a reactant/Fe ratio of 30 (increasing the ratio is necessary for heavy characterization but risks aggregation; decreasing may lead to no reaction). This solution, which appeared

increasingly green and cloudy, was shaken for 3 h with an Eppendorf Minispin + at 1100 rpm. A dark green precipitate formed during this time. Then, 1 ml of ultrapure water (Millipore, 18.2 MΩcm) was added to the solution and briefly shaken by hand to full dispersion, followed by 1 mL each of ethanol then ether (Decon Labs, 200 proof; Fisher, 99.9 %). This mixture was shaken well by hand and then centrifuged at 4,500 rpm for 30 min to form a very dark green supernatant and pellet. The supernatant was decanted and the pellet saved. 1 mL each of ultrapure water, ether, then ethanol was added again and the purification was repeated several more times, saving subsequent pellets and purifying them. The resulting samples were inverted onto a paper towel from five to ten minutes to dry and aid removal of any other leftover reactants and organics. The green solids were easily redispersed in 0.1-1 mL ultrapure water, although a brief 1-3 second bath sonication sometimes aided in this. Upon visual inspection the solutions were a brilliant emerald green.

Orange II dye remediation tests. Dye samples were prepared by mixing 10uL of sulfide-GR/Fe_3O_4 with 15uL of the azo group-containing Orange II dye (Acid Orange 7) (Aldrich, CAS 633-95-5) and diluting with 1975mL water. 5 increasing concentrations of dye were prepared and used in triplicate. Standards were also prepared in triplicate with 15uL of dye and 1985uL of water. The solutions and standard were then mixed and filtered through a 0.22 um PES syringe filter to remove the sulfide-GR/Fe_3O_4. UV-Vis was then used to determine the exhaustion point of the material; additional experiments over several weeks found no change in the basic observations.

Sulfide green rust reaction, without nanoparticles. Synthesis is mostly identical to the procedure without nanoparticles, except with iron oleate monomer replacing the nanomagnetite as the iron source.

Preparation of iron oleate monomer. Iron oleate monomer was prepared by combining iron oxide hydrated (FeOOH, catalyst grade, 30-50 mesh; 1 mmol, 0.09 g), oleic acid (OA, technical grade, 90%; 4 mmol, 1.12 g) and 1-octadecene (ODE, technical grade, 90%; 15mmol, ~4g) and heating at 240 ^{o}C for 1h. The resulting black precipitate was purified using acetone, methanol, and hexane. 5ml of the resulting precipitate was washed using 25 mL of acetone and 25 mL of methanol and centrifuged at 4500 rpm for 30 min. The purification was repeated 3 times, then the black colloid was dissolved in 15 mL of hexane. The Fe concentration measured by ICP-AES to be 3 mg/mL.

Characterization. The Fe K-edge (7112 eV) EXAFS measurements were done at MRCAT 10-ID beamline at the Advanced Photon Source, Argonne National Laboratory. [92] Fe edge measurements powder samples were mounted in plexiglass sample holders (5 mm diameter and 0.2 mm thick) for the fluorescence measurements. The iron standards needed for this experiment ($FeCl_3$, FeS pyrite, and Fe metal foil) were measured in transmission mode. The powders were spread on kapton tape and several layers were stacked so that the thickness x of the samples corresponded to $\Delta\mu x = 0.5$, where $\Delta\mu$ is the edge step of the absorption coefficient at the Fe k-edge energy. Both for transmission and fluorescence measurements with ionization chambers, the Si(111) double crystal monochromator was scanned continuously so that the data was collected

in quick EXAFS mode. 10 EXAFS scans were taken and then averaged for the liquid sample. The undulator parameters (taper and gap) were optimized to obtain a large photon flux with nearly constant intensity within the scanned energy range of 6900 to 8100 eV for the Fe edge. A Rh harmonic rejection mirror was used to eliminate X-Rays of higher harmonic energies. The incident ion chamber was filled with 20 % nitrogen mixed with 80 % helium gas whereas the transmission ion chamber was filled with nitrogen gas for proper adsorption. A reference ion chamber filled with the same gases as the transmission ion chamber was mounted behind the latter so as to record a standard spectrum of Fe foil with every scan to ensure that there is no energy shift between each scan. For fluorescence measurements, Lytle detector was filled with Argon gas. The size of the incident X-ray beam on the sample was 300 µm by 300 µm. The data was processed using Athena by extracting the XAFS oscillations $\chi(k)$ as a function of photoelectron wave number k following standard procedures.[93] The theoretical paths were generated using FEFF6 and the models were done in the conventional way using the fitting program called Artemis.[94 95] Artemis was used to refine the fitting parameters used for modeling each sample in R-space until a satisfactory model describing the system was obtained. Data sets were simultaneously fitted in R-space with k-weights of 1, 2 and 3.

X-ray Diffraction was collected on a Rigaku D/Max Ultima II Powder Diffratometer. Solid green liquor/nanomagnetite powder samples were deposited onto a round, 5 mm diameter x 0.2 mm deep indented Rigaku zero-background holder. The sample was then scanned for 5 h with the following settings: 0.5° 2θ divergence and

scattering slits, a 10 mm divergence height limiting slit, a 0.15 mm receiving slit, a 0.1° 2θ step size, and a 21.1 s per step rate. Jade 9.0 was then used to analyze the resulting spectrum.

UV-Vis Spectroscopy was carried out using a Varian Cary 5000i UV-VIS-NIR Spectrophotometer. 20 µL of the sulfide-GRsolution was added to 0.98 mL of water. This was then placed inside the spectrometer measuring a range of 225 to 800 nm. Measurement speed was 600 nm/min.

X-ray Photoelectron Spectroscopy was carried out on a PHI Quantera XPS using a substrate of indium foil at 140 eV (low resolution) for survey scans and 26 eV (high resolution) for elemental scans. 0.15 uL of sample was dropped onto the substrate an hour before introduction into the sample chamber. All scans utilized electron and ion neutralizers. Using PHI Multipak 7.0, the spectrum was corrected using the adventitious carbon peak (284.5 eV) and peak multiplets were assigned.

High-resolution transmission electron microscopy images were obtained using a JEOL 2100 field emission gun TEM at 200 kV with a single-tilt sample holder using 400 mesh ultra thin carbon-A type copper grids from Ted Pella Inc. Energy-filtering transmission electron microscopy (EFTEM), along with Gatan Imaging Filter (GIF) mapping and Energy-Dispersive X-ray Spectrometry (EDXS), provided the chemical composition information for the complexes observed.

Sizing images were acquired via a JEOL 1230 High Contrast Transmission Election Microscope at 80kV with a single-tilt multi-sample holder using the same grid type. 150

µL of sample was dried onto the grid about an hour before use of the machine. Image interpretation and sizing calculations were obtained by counting over 1000 individual nanocrystalline particles using Media Cybernetics ImagePro Plus 5.0.

Mössbauer data was collected via a SeeCo (Edina, Minnesota) instrument. Samples were deposited onto kapton film and sealed together for measurement. Spectra were then recorded with constant acceleration mode at 77 K. Final data was both smoothed and calibrated versus an α-iron foil standard.

Raman Spectroscopy was carried out on a Renishaw InVia Raman Microscope using a 633 nm laser with a 1800 lines/mm filter. Around 0.25 mL was dropped onto a glass slide and allowed to dry over the course of a few hours. Spectra were taken using a 50x lens with the laser set at 50% power for 20 s and averaged over 3 scans.

Infrared Spectroscopy was collected in a Jasco FT-IR 660 Plus Spectrometer using an ATR setup with a diamond substrate. 100 uL was dried onto the cleaned substrate and blown with nitrogen for 30 min to purge interferences. Spectra were run with a resolution of 4 cm^{-1} with averaging over 16 scans.

Chapter 3 Sulfide Green Rust in Focus

In this chapter, further attention is placed on characterizing and describing the sulfide green rust. Additionally, the formation of a bulk sulfide green rust is described. Generating a bulk, as opposed to nanocrystalline, sulfide green rust was vital in order to definitively characterize the mixed phase nanomaterial via EXAFS as seen in chapter 2. The synthetic process proceeds in a slightly different manner from the generation of sulfide green rust on the surface of nanoparticles. Specifically, the reduction occurs not on iron oxide nanocrystals but using iron oleates. Characterization of the material using a similar battery of tools was applied as in the case of the mixed phase nanocrystals, providing a clear picture of the solid state structure of this interesting material.

3.1 Introduction

Before green rust was known, a similar category of little-understood iron sulfur compounds collectively coined "green liquor," had evaded concrete identification for centuries. First identified in 1801, this material was a mystery to most who encountered it and was consistently overlooked in the literature.[76] Mellor cites it again in 1935 as a ferrous sulfide forming a dark green mass that dissolved in water, and eventually turned to a dark brown solution with exposure to air.[96,97] It was then in 1978 that Taylor shed more light on the subject by specifically examining the green liquor, coining it a green alkaline iron sulfide.[96] Most recently, Pavelko discovered a set of green precipitates from a similar reaction in 2006, and termed the material an iron dithiolate.[98]

Definitive identification of colored iron compounds such as sulfide green rust or the green liquor cannot rely on color alone. The chemistry of iron is diverse, especially with regard to color due to its status as a transition metal and energy of the Fe d-orbitals. Indeed, many iron species carry a green color when combined with certain anions as seen with iron hydroxides, chlorides, cyanides, sulfates, and the growing green rust family (Table 3.1). Oxidation and morphological changes can also contribute to characterization difficulties, and clearly the color of a compound does not specify very much about the oxidation state of iron much less its structure.

A variety of characterization techniques and experiments were used to better explain the nature of sulfide green rust. Electronic interpretations of UV-Vis, time-lapse Fe and S XPS, infrared and Raman spectroscopies, high temperature XRD, cryo-electron TEM (CRYO-TEM), and reexamination of the collected XAS data were all used to better define the sGR. Possible structural interpretations and a hypothetical mechanism of formation for the sulfide green rust were also outlined and discussed.

Table 3.1. Select Colored Fe-X compounds.

Compound	*Discovered*	*Reference*
$FeCl_3$ (iron chloride)	antiquity	Penfold et al. (1959) [99]
$FeSO_4$ (vitriol)	antiquity	Listy et al.(2002) [100]
original green liquor	1801	Vauquelin et al[76]
green rust, various	1948	Keller; Yoshioka et al. (1948) [77]
Fe-EDTA	1997	Rao et al. (1997)[78]
Fe dithiolate	2006	Pavelko et al (2006)[101]

3.2 Results and Discussion

3.2.1 Iron Oleate-Sourced sGR Formation

Homogeneity is sometimes needed when investigating a material's properties, so a new synthesis method was created for this purpose. In this process, cysteamine was used to reduce the iron oleate complex prior to its thermal decomposition for nanoparticle magnetite synthesis. Specifically, an alcoholic solution of cysteamine hydrochloride, a known metal ion scavenger, was added to an organic dispersion of prepared iron α-FeOOH oleate solution. After two to three hours of mixing in a sealed vial, a green color was observed in the alcoholic phase and the organic phase was nearly colorless. The optical absorbance of the aqueous sample showed two peaks at 400 and 675 nm (Chap. 2, Figure 2.1A). Also, after this process the brownish-black iron oleate solution transferred from the organic phase to the aqueous phase where it appeared green. The green material that formed was a sulfide green rust (termed here sGR), identical to the second phase formed in the nanocrystal reaction described in Chapter 2 (Figure 2.1).

3.2.2. UV-Vis Evidence of Charge Transfer

Electronic spectra like those of sulfide green rust contain vital information about the electronic transitions of the main iron bonds, and can be indirect evidence for structure. To decipher the sGR spectrum, we must examine the types of transitions possible in iron complex absorption spectra. Complexes whose electrons exhibit a change of electron spin or symmetry type upon excitation may or may not have highly

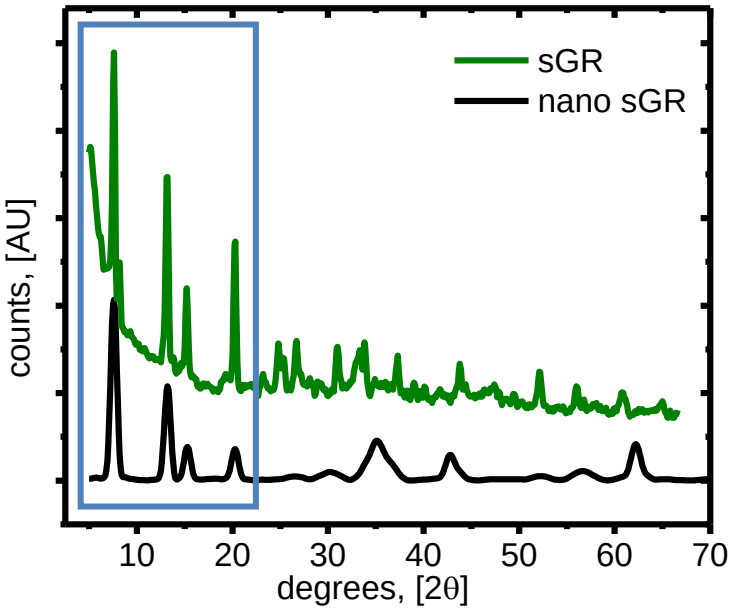

Figure 3.1. Sulfide green rust is capable of being synthesized without the iron oxide cores. Iron oleate was used as a reactant to form sGR, and the result maintained the same definitive d-spacing found in the nano version. The blue box above indicates the major overlap of the two sGR types.

absorbing features depending on the crystal structure and electronic configuration of the system.[102] Certain symmetries have more allowed transitions than others, as seen in the octahedral example in Table 3.2. Allowed transitions will result in intense adsorption bands, while forbidden transitions can be very small and sometimes hidden under more intense features. Lastly, charge transfer (CT) transitions, where an electron is donated from a ligand to a metal with a formal reduction of the latter, can be extremely strong transitions orders of magnitude more intense than d-d* transitions. [103]

In the case of the sGR, the spectrum clearly shows marked absorption at 400 and 675 nm in the red and blue regions (Figure 3.2) of the UV-Vis spectrum consistent with its green appearance. Such intense absorption bands must correspond to either spin-

Table 3.2. Allowed and forbidden transitions in an octahedral environment. All calculations were executed via the Lancashire TS tool. [104]

Compound	*Spin state*	*# of spin-allowed transitions*	*ligand field strength to match peak ratio (Δ/B)*
I_5	low	many	strong *(~41)*
	high	none	none
I_6	low	3	moderate *(~20)*
	high	1	none
I_7	low	3	none
	high	3	moderate *(~20)*

allowed d-d* or ligand-to-metal, S *p* π -> Fe d-orbital charge transfer transitions. Using the Tanabe-Sugano (TS) diagram for the expected Fe(II) d^6 octahedral configuration, there is a reasonable match to the observed peaks.[104] Allowed calculated d-d*

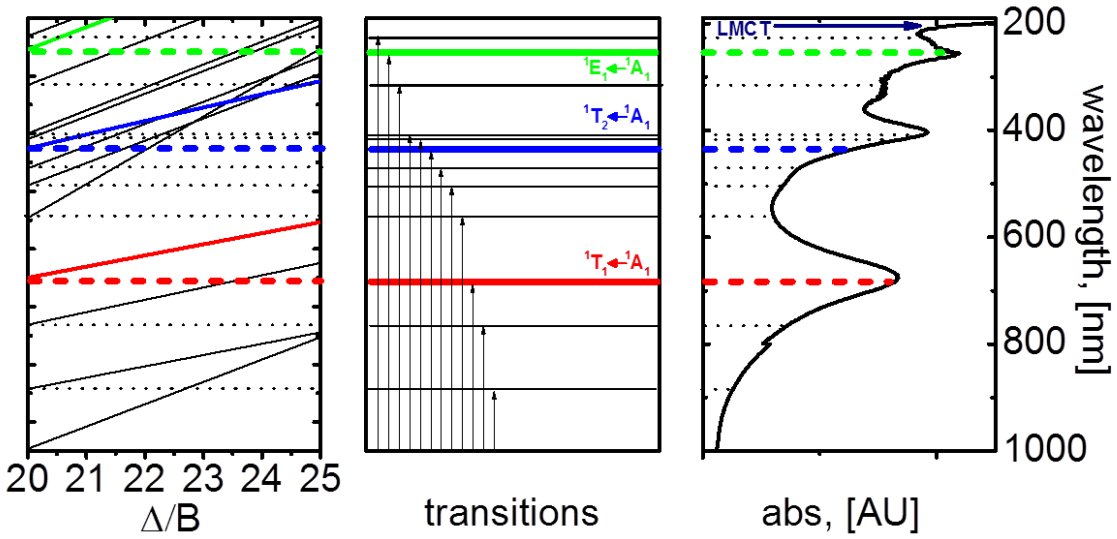

Figure 3.2. Moderate field strength ligand in Fe(II) low-spin complexes (~20, left panel) exhibit electronic transitions (center panel) that occur remarkably close to observed absorptions in sulfide green rust (right panel). Calculated from an online TS tool created by Lancashire, and with similarities to Kondo. Adapted from Lancashire's Online Tanabe-Sugano tool (2003), [104] Kondo et al., (2003), [105] and Nassau (1980).[106]

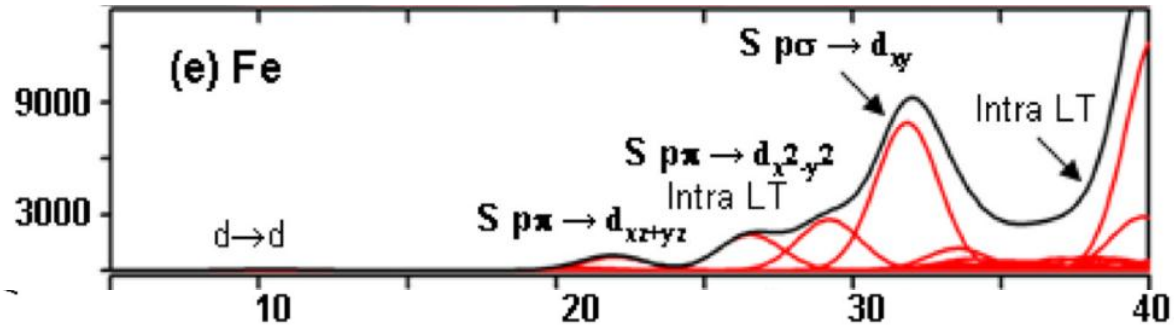

Figure 3.3. Simulated electronic spectra of the similarly bound [ML(SC6F5)] from the TD-DFT calculations. Contributions from individual electronic transitions are shown in red. D-d* transitions are limited to anything above 500 nm (20000 cm-1), while LMCT transitions dominate from 500- 250 nm (40000 cm-1). "Intra LT" stands for contributions that exist between the ligand itself. Adapted from Gorelsky et al., (2005).[107]

transitions of similar intensity appear very near the physical values, while the final peak below 200 nm is far above the scale we see here and therefore labeled a LMCT.

Different conditions were also examined. A Fe(III) d^5 configuration would require a moderately strong field ligand to maintain the ratio needed to match the observed electronic spectrum, while a less common Fe(I) d^7 state is too small to match. These data thus lend support to a conclusion of a Fe(II) low spin d^6 compound. Interestingly, Figure 3.3 offers an alternative view of electronic assignment; however, this is for a tetrahedrally coordinated compound.[107]

Also interesting to note is excitations by light into higher d orbitals results in a temporary high-spin state. This is because Δ_{CFT} is small enough for light just above the visible wavelength to readily excite numerous electrons from a low-spin, diamagnetic

state into a pseudo paramagnetic state. This suggests the material may have interesting opto-magnetic properties.

3.2.3 **Fe(II) Surface Chemistry via X-ray Photoelectron Spectroscopy**

X-ray photoelectron spectroscopy (XPS) provides information about the elements at the surface of a bulk material as well as their oxidation state. Typical penetration depths for electrons are on the order of 1 – 2 nanometers. The sulfide green rust Fe $2p_{3/2}$ spectrum shows the characteristic features of any iron containing substance: a Fe^{2+} 2*p* and Fe^{3+} 2*p* transition within the 700-720 eV range. The specific location of the peaks suggests iron-sulfide as opposed to iron-oxide bonds dominate in the near-surface of the material (Figure 3.4). Typical Fe-S materials listed in Table 3.3 indicate its higher energy peak matches well to Fe(II). Additionally, oxidation over time with exposure to air caused this peak to diminish almost completely (Figure 3.5); this instability further supports the assignment of the peak to a Fe(II) species reverting to its oxidized Fe(III) form.

3.2.4 **Sulfur Oxidation via XPS**

Given the suggestion in the iron XPS data that iron is bound to sulfur, we examined the sulfur peaks also present in XPS. The sulfide green rust S $2p_{3/2}$ spectrum reveals both iron-sulfur bonding and a concurrent oxidation of the sulfur (Figure 3.6). Bound thiol groups are noted to exist at the highest energy, near 161.5 to 162.7 eV. Additionally, the presence of original unbound thiol or disulfides is also apparent, though

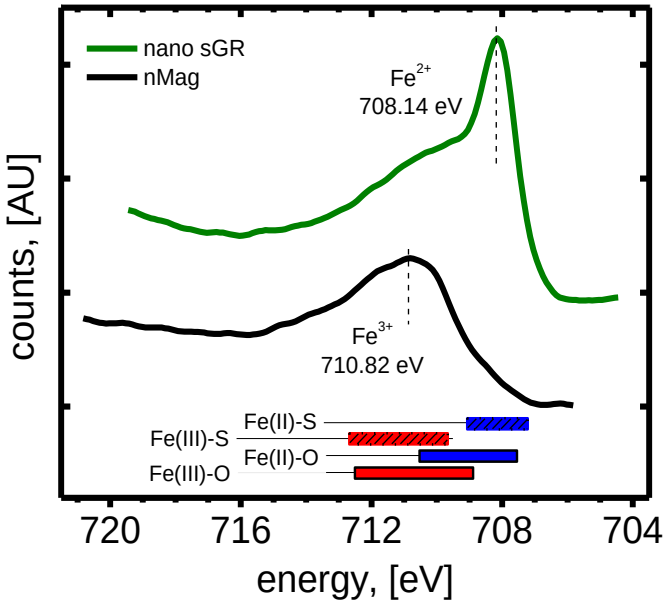

Figure 3.4. sGR's Fe $2p_{3/2}$ XPS main peak shows resemblance to Fe(II)-bearing iron sulfide compounds listed in Table 3.3. Note that the main Fe shift for both the nano and bulk versions of this material are the same. Reference bands courtesy of the free NIST XPS online database.[108]

quantification is challenging due to overlap in their spectra at 163-164 eV. Finally, the high oxidation state (+6) sulfate group is observed in low quantities near 168 eV. [109]

Table 3.3. Typical FeS XPS values. Adapted from Lennie and Vaughan.[110]

Compound	*Mineral type*	*Energy*	*Reference*
FeS_2	pyrite	707	Buckley and Woods (1997) [80]
		707.2	Lennie and Vaughan (1996) [110]
		707.5	Buckley and Woods (1987) [80]
$Fe_{1-x}S$	marcasite	707.25	Lennie and Vaughan (1996) [110]
$Fe_{0.89}S$	pyrrhotite	708	Buckley and Woods (1985) [80]
		708.5	Buckley and Woods (1985) [80]
Fe_7S_8	pyrrhotite	707.45	Pratt et al. (1994) [111]
		707.8	Jones et al. (1992) [112]
$Fe_{1-x}S$	mackinawite	707.8	Lennie and Vaughan (1996) [110]
Fe_9S_{11}	greigite	707.3	Herbert et al. (1998) [113]
sGR		708.14	(this work)

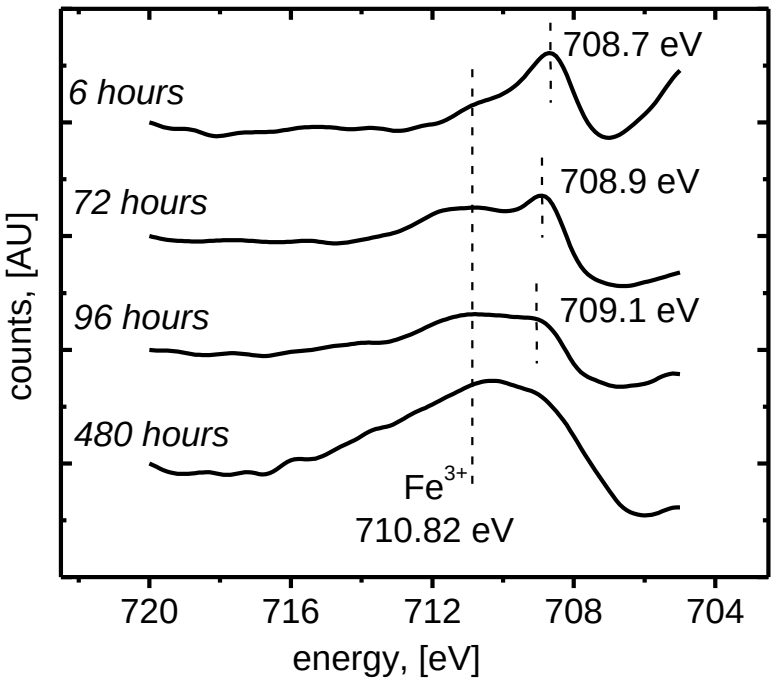

Figure 3.5. XPS Fe spectra over time left out to dry in air. A shift back to a more oxidized form is apparent within 3 days, and only a shoulder remains after nearly 3 weeks.

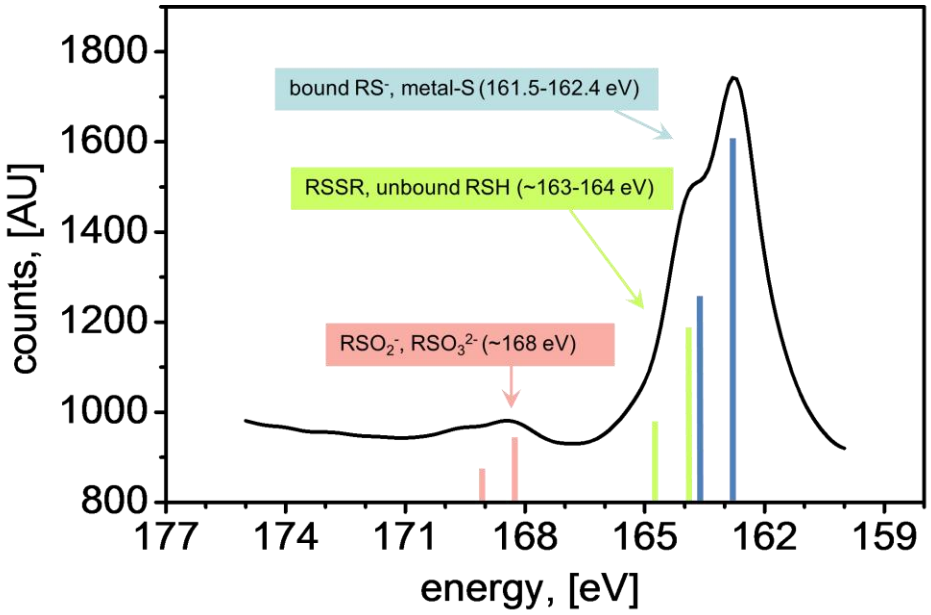

Figure 3.6. XPS *S* $2p_{3/2}$ spectrum showing bound thiol, unbound or disulfide, and oxidized/oxygenated peaks. This is a clear indication of gradual oxidation and oxygenation of the thiol. Values taken from Volmer et al. (1992). [109]

3.2.5 **Cysteamine presence confirmed via Infrared Spectroscopy**

Infrared spectroscopy (IR) allows us to observe cysteamine thiol group directly. Figure 3.7 illustrates the persistence of the thiol group, as well as the similarity between unmodified cysteamine before synthesis and sGR. Note that thiol C-SH stretch in infrared absorption is relatively weak due to a weaker dipole compared to analogs like oxygen.

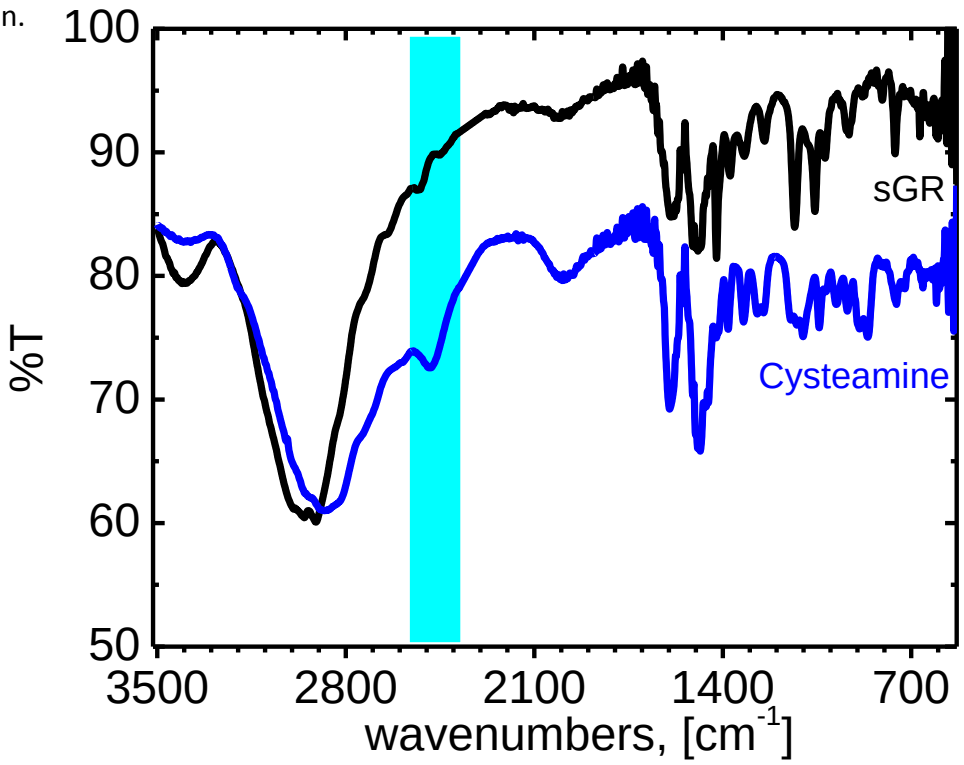

Figure 3.7. The thiol group is removed enough from the fingerprint region of IR to be observed. Note the similarity between the spectra, indicating cysteamine presence in the product. The blue band indicates the typical –SH region.[114]

3.2.6 **Sulfur bonding observed via Raman Spectroscopy**

Raman spectroscopy confirms the formation of an iron sulfide with the sGR. Highly polarizable bonds such as C-S and S-H are excellent specimens for Raman and

produce higher intensity peaks than in IR spectroscopy.[114] Possible cis- and trans-cysteamine present within the structure and on the iron surface seem to also be visible (Figure 3.8).[115,116,117,118,119]

Identification is made using existing literature descriptions of Fe-S compounds (Tables 3.4-5); while there is not a perfect match to mineral spectra, some of the peaks

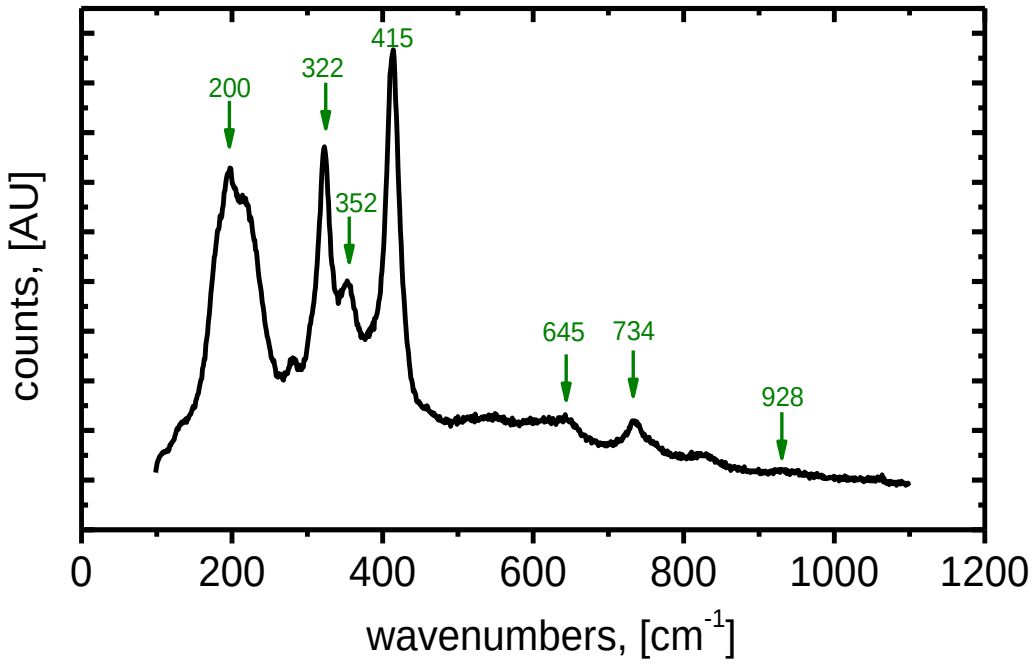

Figure 3.8. Raman spectroscopy suggested Fe-S bonding, as well as the cis- and trans-cysteamine on the iron surface; a perfect match to mineral literature values (see Table 3.5.) was not observed.

Table 3.4. Raman peak assignments.

Wavenumber	Strength	Peak	Reference
198	strong	δ(FeSC)	Dave, 2005[116]
322,352	strong, medium	Fe-S stretch	Johnson, 1981[115]
415	strong	FeS_2, S-S stretch	Descostes, 2002;[117] Descotes, 2010[119]
645	weak	ν(C-S)-gauche AET bound	Wrzosek, 2005[118]
734	weak	ν(C-S)-trans AET bound	Wrzosek, 2005[118]
928	weak	ν(C-C), ν(C-N) AET stretch	Wrzosek, 2005[118]

Table 3.5. Typical Fe-S Raman parameters.

Compound		*Peaks*	*Reference*
FeS_2	pyrite	353-342, 377-387, 446	Mernagh et al. (1993) [120]
FeS_2	marcasite	324, 387, 532	Mernagh et al. (1993) [120]
Fe_3S_4	greigite	138, 190, 247, 350, 365	Remazeilles et a. (2010) [121]
Fe_9S_{11}	smythite	262, 267, 326, 329, 358, 394	Bon 2012[122]
Fe_7S_8	pyrrhotite	no record;not raman active	Mernagh et al. (1993) [120]
FeS	troilite	weak raman scatterer	White et. al 2009 [123]
$Fe_{1-x}S$	mackinawite	206, 256, 296, 310, 322, 355	Remazeilles 2010 [121]
traditional Fe-O GR		427, 518	Trolard et al. (1997) [14]
sGR		198, 322, 352, 415, 645, 734, 928	this study

are close to known values such as the 415 cm^{-1} peak for Fe(II)-S_2 or the 198 cm^{-1} peak for the δ(Fe-S-C polarizable bend.[117,116] This continues to support the likelihood of a unique FeS-like material that maintains its organic portion after synthesis, namely sulfide green rust.

3.2.7 **Fe-S-like Instability from HT XRD**

XRD provided a very unique diffraction pattern for the sGR defined by its low 2θ peak. These peaks did not match any known compound and high-temperature XRD saw a change in this peak structure. The largest feature was removed (and the green color lost) as temperature reached around 90°C (Figure 3.9). In comparison to the values in Table 3.5, this fits into the general trend for many metastable Fe-S compounds having been known to decompose above 75-100 °C.[110] Another interpretation of note is that 90°C is about the cysteamine melting point temperature, which also suggests the newly formed sGR may include this molecule.[75]

Table 3.6. Iron sulfides: structure and stability. Adapted from Lennie and Vaughan. [110]

Compound		*Stability*
eS_2	pyrite	stable (<742 °C)
eS_2	marcasite	metastable
e_3S_4	greigite	metastable
e_9S_{11}	smythite	metastable (~75°C)
e_7S_8	pyrrhotite	metastable, (~100°C)
e_9S_{10}	pyrrhotite	metastable, (~100°C)
$e_{10}S_{11}$	pyrrhotite	metastable, (~100°C)
$e_{11}S_{12}$	pyrrhotite	metastable, (~100°C)
e_9S_{10} - $Fe_{11}S_{12}$	pyrrhotite	metastable, (~220°C)
eS	troilite	stable, (<138°C)

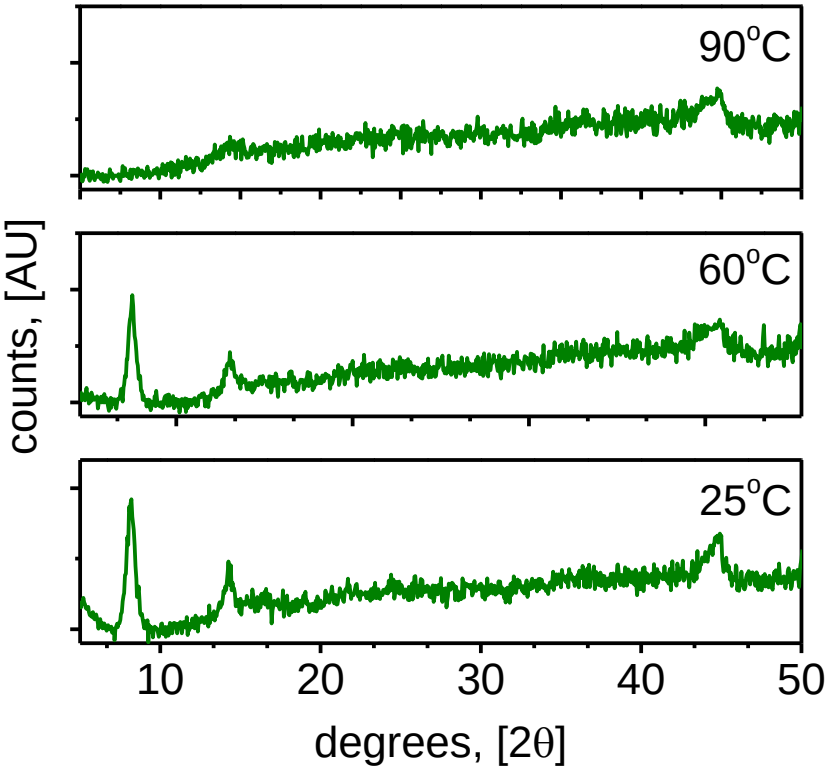

Figure 3.9. High temperature changes in the diffraction pattern suggest similarity to other metastable FeS compounds. All color was lost as the temperature was gradually increased to 90° C. Peaks matching to the sulfide green rust spectrum can be seen in low 2θ region, and were lost as temperature increases close to the cysteamine boiling point of 90° C. The peak near 2θ = 45 was from the Mylar film filter required by the instrument for high temperature XRD.

3.2.8 **Crystallinity Confirmation via Cryo-TEM**

The sGR is not a salt, but a metastable iron compound matching well with other iron sulfide compounds. Cryo-TEM is capable of examining the materials natural state in solution, alleviating oxidation or other changes that may occur upon drying. Since XRD demonstrated clearly defined peaks for the material, Cryo-TEM functioned to support this information and crystallinity was confirmed (Figure 3.10).

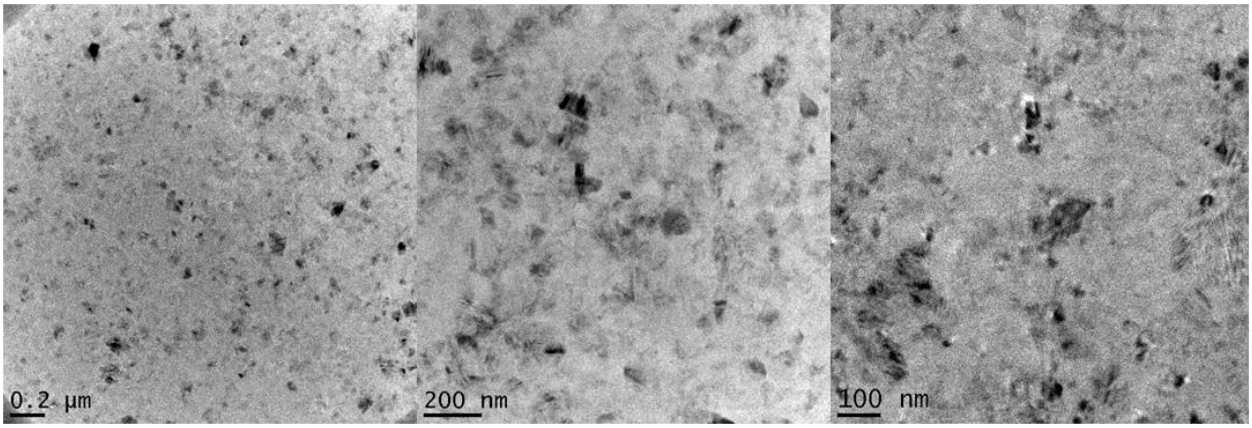

Figure 3.10. Cryo TEM images, showing that the sulfide green rust is a crystalline solid in a suspended state. Sample was sourced from FeOOH, and no nanoparticles were used for synthesis in these images.

3.2.9 **Examination of α-FeOOH sGR via X-ray Absorption Spectroscopy**

Iron-sulfur bonding is further confirmed by examining the Fe K-edge X-ray absorption measurements (Figure 3.11A). In this X-ray Absorption Near Edge Spectroscopy (XANES) figure, standards were measured alongside our sGR for comparison. Similar to data shown in Chapter 2, we see that the sGR is most similar to that of Fe-S_2 marcasite, while matches to the iron foil and iron chloride are unlikely.

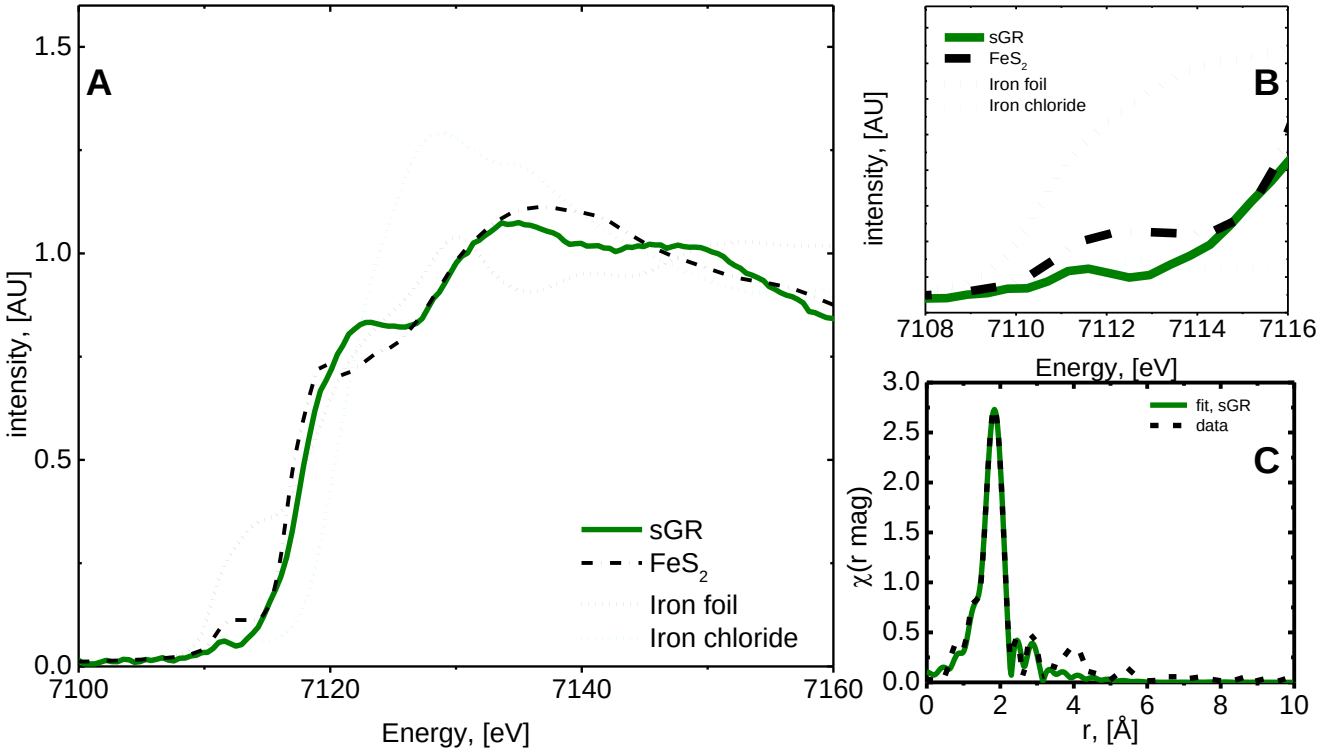

Figure 3.11. Sulfide green rust synthesized from α-FeOOH (goethite) iron oleate complexes resulted in a more homogenous compound with which to study, thus aiding in XAS bond distance measurements. Fe K-edge XANES spectra of the sGR (a) compared standard compounds containing Fe in various oxidation states and geometries, further corroborated a good match for Fe-S bonding, and indicated an increase of Fe(II) over any other material tested thus far (b). Fe K-edge EXAFS magnitude FT data (c) demonstrated Fe-S bonds similar to the iron sulfide mineral, marcasite. The atomic distances for Fe-S and Fe-Fe were 2.29 Å and 3.41 Å, respectively. Bulk marcasite FeS_2 standards measured are quite close with Fe-S at 2.26 Å and Fe-Fe at 3.82 Å, with an excellent R-factor fit of 0.01.

Close to the main peak at 7120 eV, information here is often specific to oxidation state; we see the sGR may be the most reduced of the samples tested. (Figure 3.11B).

Fe K-edge Extended X-ray Absorption Fine Structure (EXAFS) magnitude FT data demonstrated Fe-S bonds similar to the iron sulfide mineral, marcasite. The atomic distances for Fe-S and Fe-Fe were 2.29 Å and 3.41 Å, respectively. Bulk marcasite FeS_2 standards measured are quite close with Fe-S at 2.26 Å and Fe-Fe at 3.82 Å, with an excellent R-factor fit of 0.01. (Figure 3.11C).

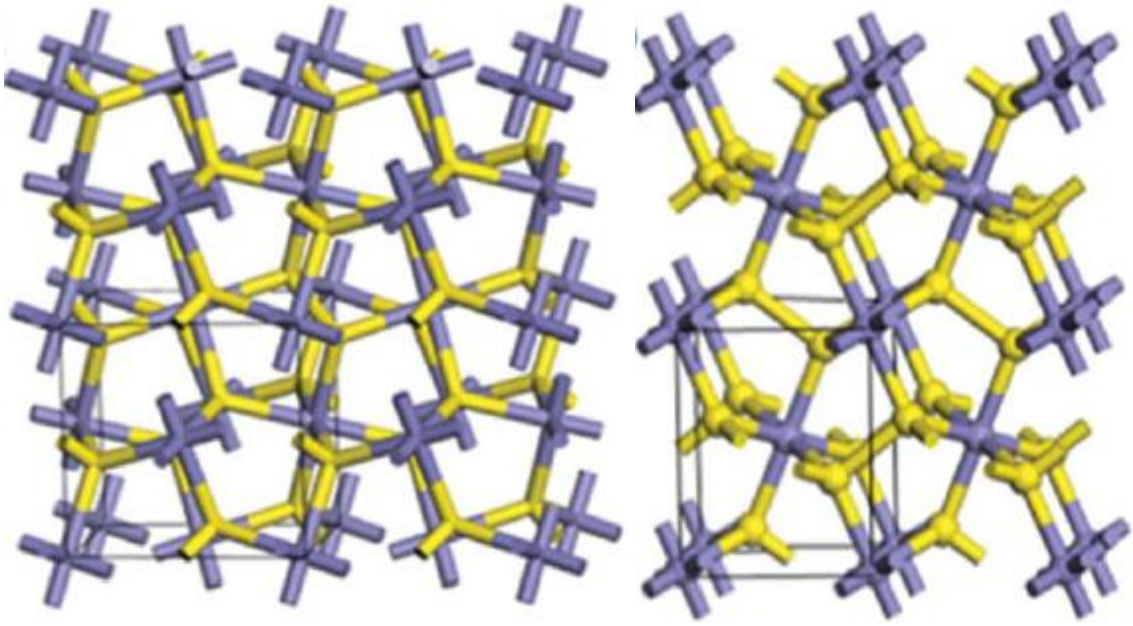

Figure 3.12. Pyrite (*left)* and marcasite (*right*) are dimorphs of FeS_2; the former is a cubic while the latter is orthorhombic (i.e., stretched cubic unit cell). Courtesy of Zhu et al., 2012.[124]

3.3 Analysis

Sulfide green rust demonstrates both mineral and coordination compound characteristics. Table 3.7 collates the most vital thiol/sulfide identification data collected with established literature values.

3.3.1 Experimental Verifications

Investigations on reactant concentration dependence, type of reactant, size of nanoparticle, as well as acid used were conducted. UV-Vis was used as an excellent, quick indicator for determining if a successful transformation to sGR occurred; the culmination of this work can be seen in Figures 3.13-3.17. A blind experimental test was then conducted by a lab colleague where 14 random nanomagnetite batches from 5 different synthesizers were chosen throughout the lab for testing of the method described (Figures 3.16,3.17). Obstacles to formation of the green liquor were overcome, as all 14 samples were successful.

acids / reactants	citric acid	benzoic acid	hydrogen chloride	hydrogen bromide
ethylamine	×	×	×	×
ethylthiol	×	×	×	×
cysteamine (AET)	×	×	✓	✓
cysteamine HCl (control)	×	×	✓	✓

Solvents
- methanol
- ethanol
- propanol

Figure 3.13. Various reactants and environments were tested to experimentally determine the nature of the reductant. Only cysteamine dispersed in an alcohol with an accompanying halide produced a green color. Any addition of water before synthesis resulted in no reaction.

Table 3.7. Various related FeS bond parameters.

Compound/Mineral Type	*Structure*	*Bond distance*	*Bonding Energy*	*Mossbauer Temperature*	*Isomer shift*	*Quadrupole split*	*Coordination Number*	*Reference*
FeS_2 (pyrite)	orthorhombic/cubic Fe(II)	S: 2.26; Fe: 3.82	707 707.2	300 300 81	0.59 0.088 0.181	0.61 0.614 0.62	6	Morice et al., 1969[125] Temperly et al., 1965[86]
FeS_2 (marcasite)	orthorhombic Fe(II)	S: 2.25; Fe: 3.38	707.25	300 81	0.051 0.147	0.506 0.504	6	Vaughan et al., 1991[110]; Morice et al., 1969[125]; Temperly et al., 1965[86]
Fe_3S_4 (greigite)	spinel (cubic)	S: 2.14; 2.46; Fe: 3.49					4:6	Morice et al. 1969[125]
$Fe_{1-x}S$ (mackinawite)	PbO-type (tetragonal)						4	Vaughan et al., 1991[110]; Morice et al., 1969[125]
$Fe_{0.89}S$ (pyrrhotite)	NiAs; superstructure	S: 2.47; Fe: 2.94	708 707.45				6	Morice et al., 1969[125]; Pratt et al., 1994[111]
$[Fe(CO)_3((CF_3)_2C_2S_2)]_2$	mononuclear, Fe(II)	S: 2.28-2.29;μ-S 2.33; Fe: 3.363		298	-0.01	0.35	6	Berry et al., 1988[126]
$[Fe(CO)_2(PPh_3)\{(CF_3)_2C_2S_2\}]$				298	-0.10	1.29	5	Berry et al., 1988[126]
$[Fe(CO)(PPh_3)_2\{(CF_3)_2C_2S_2\}]$				298	0.00	1.18	5	Berry et al., 1988[126]
$[Fe(CO)(dppe)\{(CF_3)_2C_2S_2\}]$				298	-0.10	1.45	5	Berry et al. 1988[126]
$[Fe_2(CO)_6(SPh)_3]_6$	binuclear, 3 μ-L			298	0.01	0.29	6	Berry et al., 1988[126]
$[Fe_2(CO)_6(SPh)_2]$	binuclear, Fe(I)			298	-0.04	1.09	6	Berry et al., 1988[126]
$[Fe_2\{S(CH_2)_2NH_3\}_2(NO)_4]^{2-}$	distorted tetrahedral 2 μ-S	S: 2.24; Fe: 2.65 - 2.682		294	-0.0595	1.098	-	Rudneva et al., 2009[127]
$Fe(S_2C_2Ph_2)_2$	Fe-bis-dithiolate;		708.6	77	0.15	1.98	-	Blomquist et al., 1983[87]
$(Et_4N)Fe(S_2C_2(CN)_2)_2$	Fe-bis-dithiolate;		707.9	77	0.24	2.72	-	Blomquist et al., 1983[87]
$(Et_4N)_2Fe(S_2C_2(CN)_2)_3$	Fe-tris-dithiolate;		708.4	77	0.14 0.37	1.52 0.77	-	Blomquist et al., 1983[87]
$(Ph_4P)_2Fe(S_2C_2(CN)_2)_3$	Fe-tris-dithiolate;		708.5	77	0.14 0.37	1.57 0.63	-	Blomquist et al., 1983[87]
$[Fe\{S(CH_2)_2NH_3\}_2]^{2+}$	sulfide green rust	S: 2.29; Fe: 3.41	708.14	77	0.149 -0.182	1.98 0.749	Fe-S: 5.1	this work

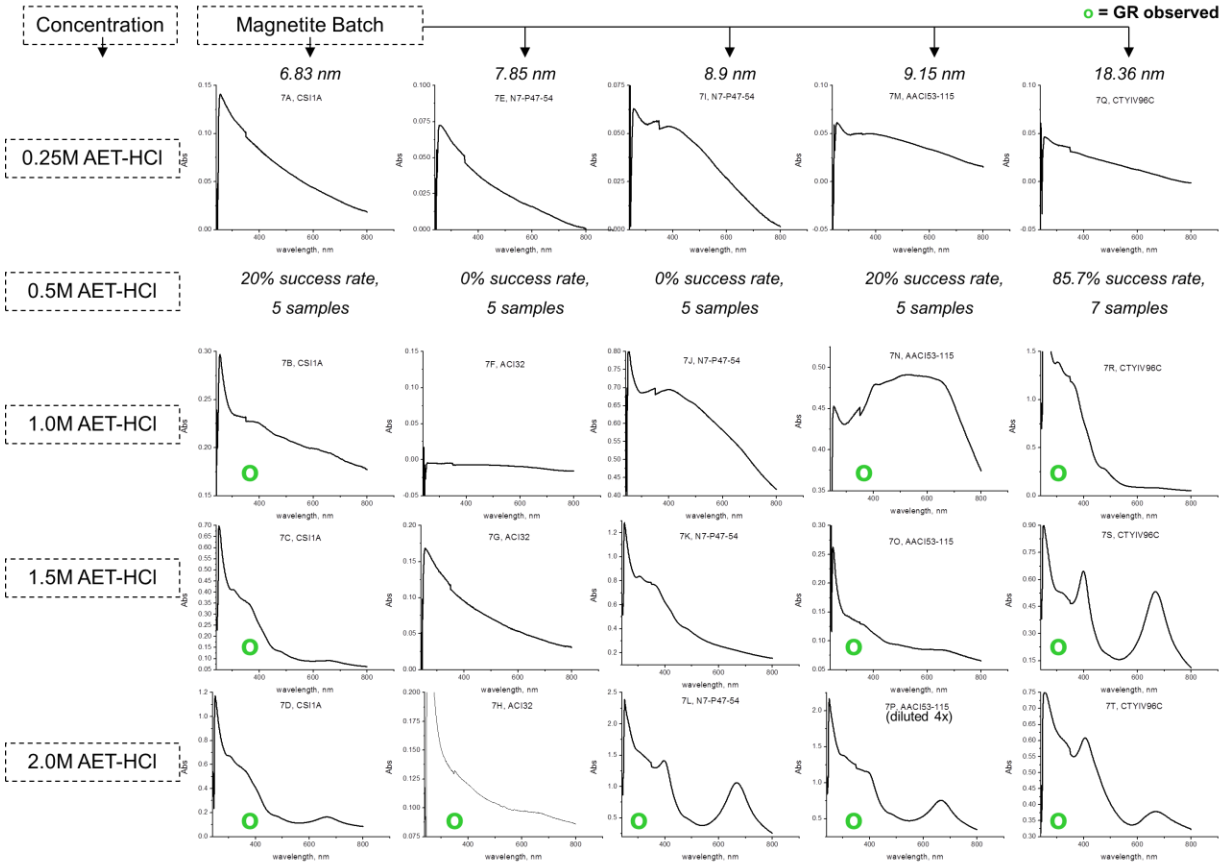

Figure 3.14. Initial attempts to produce sGR were inconsistent, so both a concentration and size study was conducted. Size did not have an overwhelming effect on synthesis, while reactant concentration seemed to be the determining factor in sGR synthesis.

3.3.2 Fe-S Structural Interpretation

The thiol used to form sGR in this study, cysteamine hydrochloride, ([HSCH2CH2NH3]Cl), has shown variable bonding modes to metal centers in the literature (Figure 3.18). Bidentate coordination is common, bridging clusters at the sulfur atom can occur, and linear monodentate examples have all been reported.[128,127,129,81] Additionally, the hydrochloride salt of cysteamine has been shown to use the Cl^- ion as a 4-fold acceptor of H-bonds from the surrounding cysteamine molecules, even when concurrently bonded to a metal center.[81]

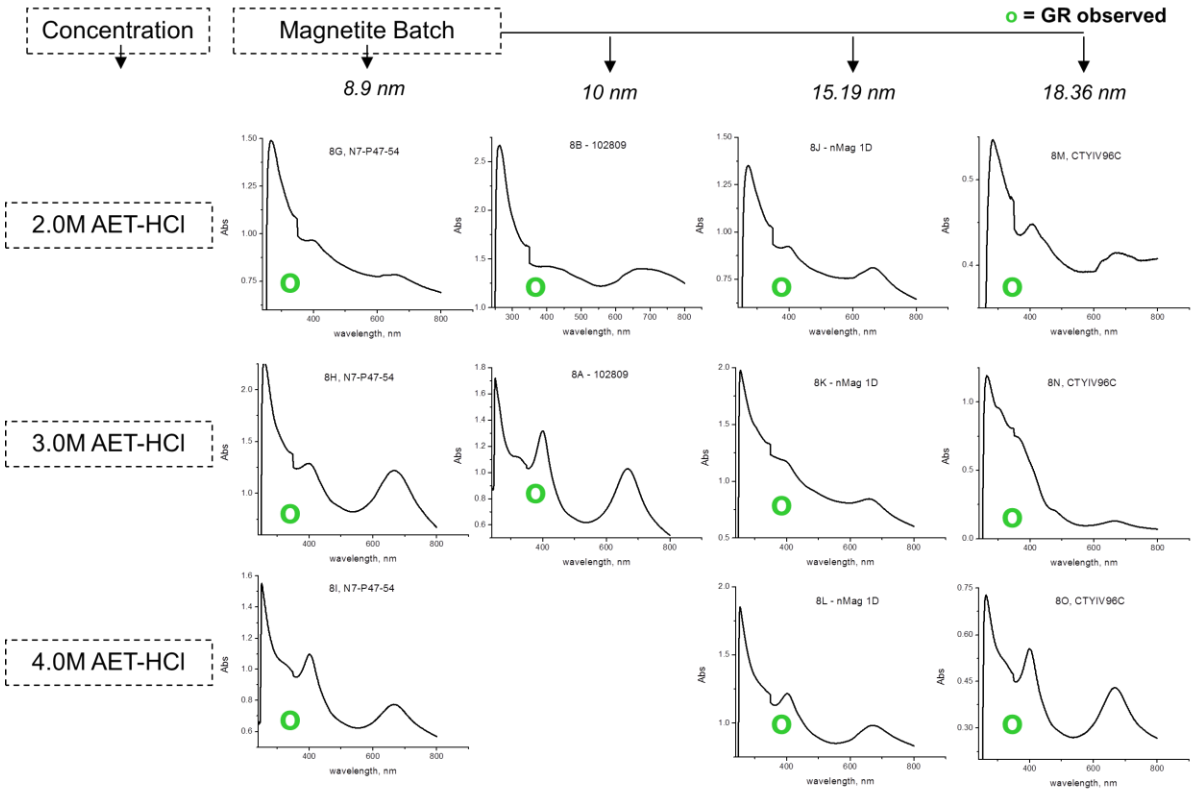

Figure 3.15. New tests were conducted with some of the same samples in the previous test and under the same conditions, however reactant concentration was drastically increased. All samples transformed into sGR.

3.3.3 Hypothetical Proposed Formation Mechanism

Initially the process to form bulk sGR began by suspending granular α-FeOOH (goethite) via iron oleate. This complex has three oleate groups attached to the Fe center in a bidentate configuration as shown below, while in the latter oleate groups similarly encapsulate the entire nanoparticle (Figure 3.19).[130]

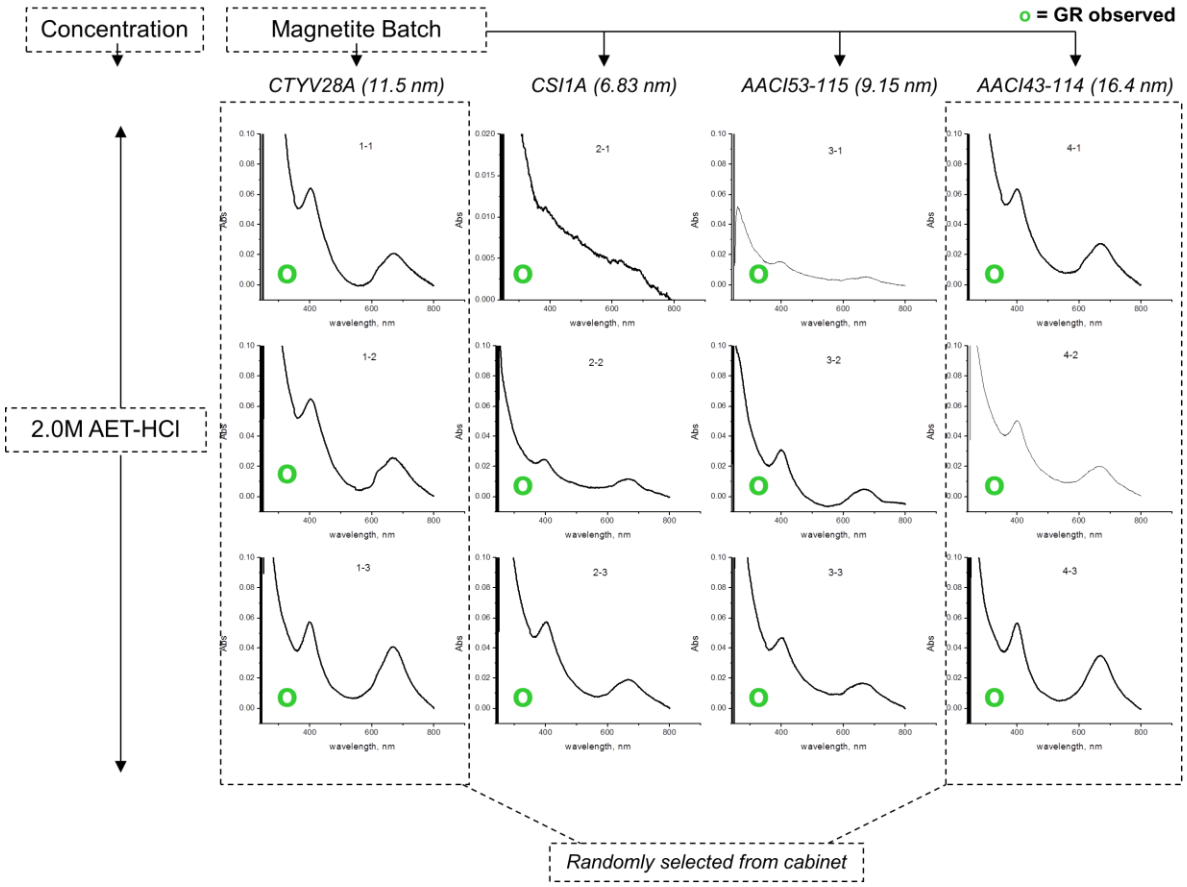

Figure 3.16. A blind test conducted by a colleague resulted in 100% success in sGR reaction consistency. Random magnetite samples from around the lab, made through unknown methods, and of different size were chosen by him as a starting material.

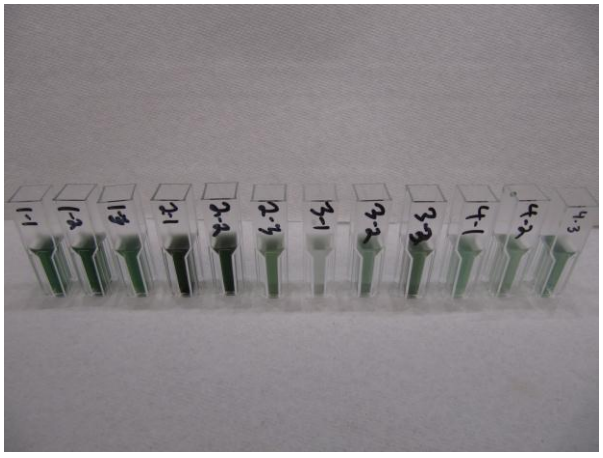

Figure 3.17. Visual to the naked eye, all 14 samples were transformed into sGR.

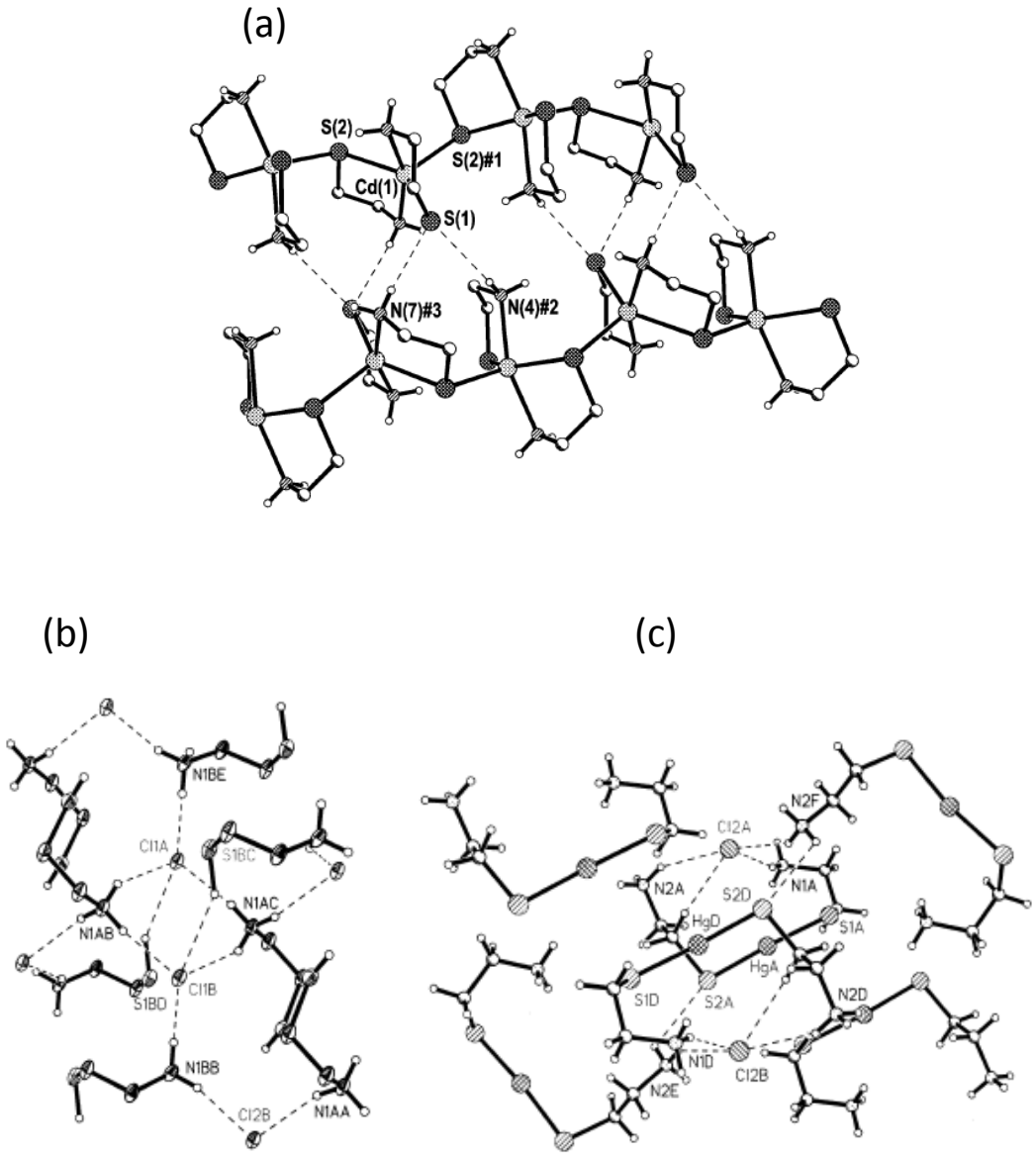

Figure 3.18. Various cysteamine compounds in the literature, with and without chloride presence. M-cysteamine bonding can occur in some cases without Cl-, as seen in (a) with cadmium. Chloride can completely change this structure; however, (b) does not contain a metal but hydrogen bonds to the Cl-. Once mercury is added, linear Hg-S bonds form but maintain a 4-fold h-bonding coordination. Adapted from Kim et al. (2001) and Fletcher et al. (2005).[75 81]

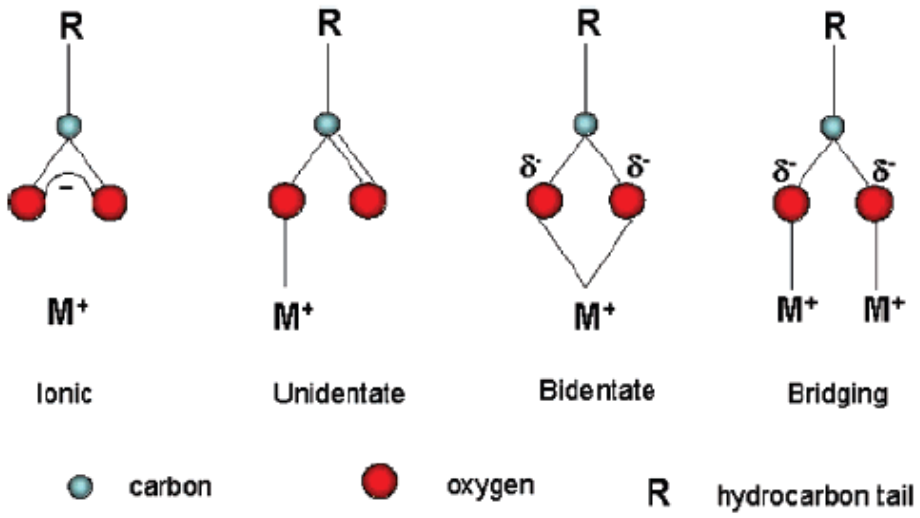

Figure 3.19: Different possible configurations of iron-oleate complex. Adapted from Bronstein et al. (2006).[130]

From there, a multistep process follows:

(1) protonation of coordinating oleic acid hydroxyl groups in a protic environment

(2) reduction of iron from Fe(III) to Fe(II) via thiol oxidation & creation of thiyl radical

(3) thiyl reaction with other thiyl species forming disulfides

(4) ligand exchange with sulfur species and C-S bond breakage

(5) cyclic repetition of steps 2-5 to form sulfide green rust

The synthesis begins in a solution with a large concentration of protons. No other green rust has been formed via an acidic mechanism and without introduction of a base, however Genin in 2006 stated one possibility for green rust synthesis beginning with the dissolution of Fe(III) in an acidic medium.[33] In our case, this occurred due to complete

disassociation of the HCl added as a part of the salt reactant, cysteamine HCl. HCl's pKa (a value only truly pertinent in water) is quite low; concurrently, amine's pKa is relatively high, leading to complete protonation to RNH_3^+. It is this difference that results in a "pseudo-acidic" protic methanol solution. An additional effect could include protonation of the oleic acid carboxyl group in the iron oleate monomer (Equation 1). Altogether, this would ultimately result in weakened interaction between iron and the carboxylic acid functional group.

(1)

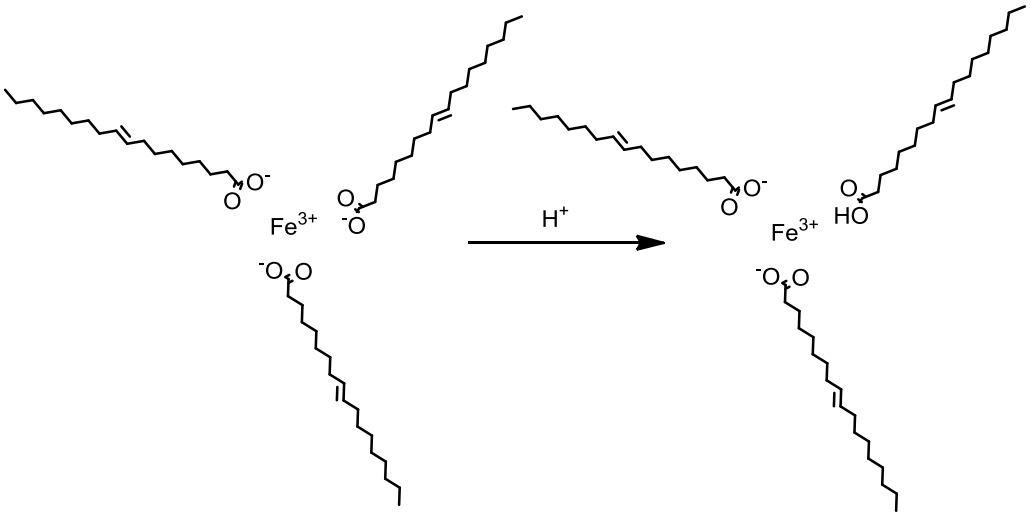

In the next step, focus is on the sulfur for Fe-S bonding and iron reduction to occur. As with their carboxylate analogs, the mechanism could possibly proceed through its reduced form, the comparatively reactive species of thiolate, RS^-. This is however unlikely due to the acidic conditions during the synthesis; thiols typically have a range of pKa's near 8.5 A good example of thiol reactions with Fe in an acidic medium has been studied by Kolthoff (Figure 3.20).[131] Any thiol consumed > pH 9 converted Fe(III) to Fe(II) with expected first-order kinetics and quick reaction times; the

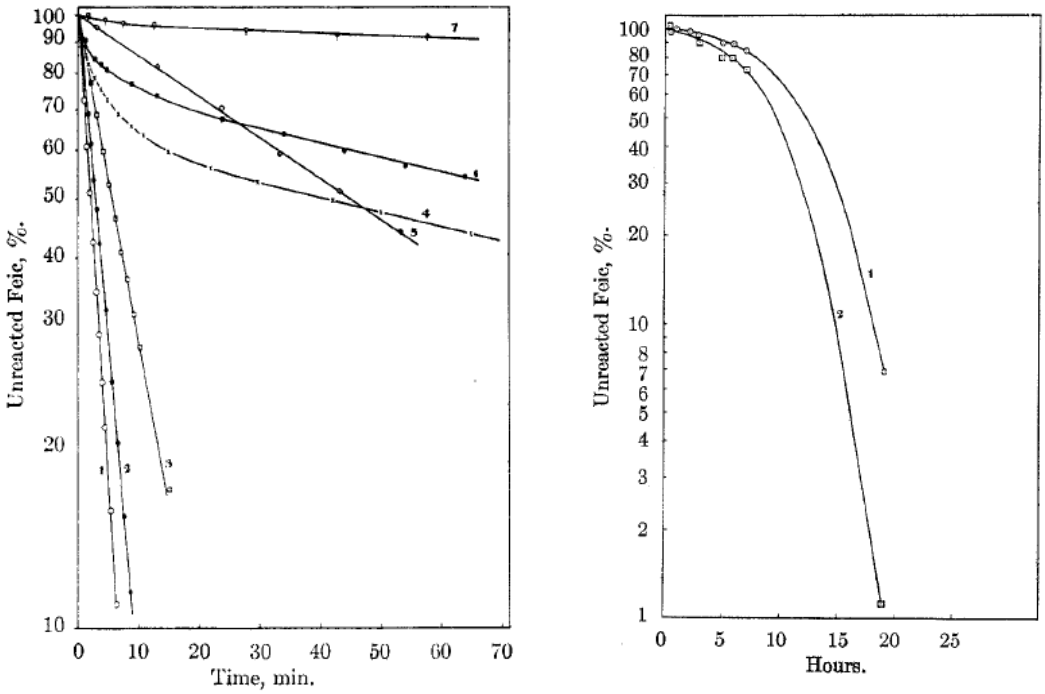

Figure 3.20. Reduction of Fe(III) via thiol in basic and acidic environments. Reduction follows a clearer pathway in more basic environments (1,2 and 3, *left*) around pH 11 via the reactive sulfur species dominating under such conditions, i.e. the thiolate. Acidic environments (*right*) between pH 3 and 5.5 still result in a reduction of the iron, however more slowly and from a more second-order pathway. Adapted from Kolthoff et al. (1961).[131]

pKa of thiols is around 8.5, so some species of nucleophilic and reactive thiolate would be present. Contrast this with solutions of pH < 6: typical reaction times for producing Fe(II) were measured in hours and with a second-order pathway.

One way to explain this alternative means for iron reduction is through the thiyl radical. In comparison to oxygen, sulfur can engage in radical chemistry, specifically RS*, due to the stabilization provided by sulfur's d-orbitals.[132,133] A thiyl pathway for reduction would be multistep (Equation 2), not first-order, and taking more time than the thiolate pathway; this is similar to our sGR reaction conditions and time frame.

(2) 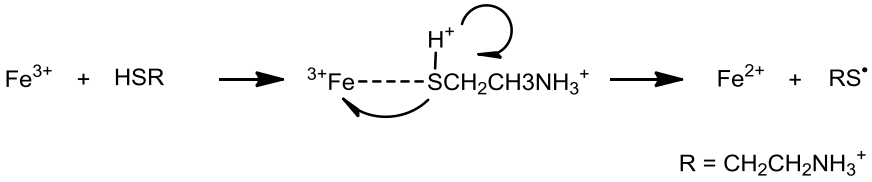

Literature has already indicated that metal reduction will result in thiyl formation and subsequent disulfide formation (Equation 3); indeed, various oxidation species are present after sGR synthesis as observed in the S XPS data from Figure 3.6.[134]

(3) 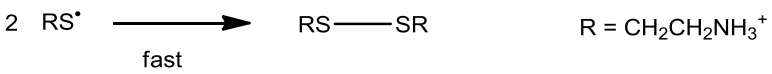

Mechanisms for disulfide formation imply the formation of the thiyl radical first.[132] Therefore, the proposed one-electron ligand-to-metal charge transfer is a natural step in the oxidation of sulfur.[132]

Organic disulfides, once formed, can then in turn bond with iron to form Fe-S_2. C-S cleavage is also required to form a Fe-S backbone, since XAS data in Figure 3.11 suggests, the final form of this material is one similar to the iron sulfide mineral marcasite. In order to achieve an iron center similar to the mineral, carbon must be removed from the core of the sulfide green rust. This occurs via a documented process of oxidative cleavage leading from M(II) to M(III), removing sulfur from the rest of the ethylamine.[135]

(4) 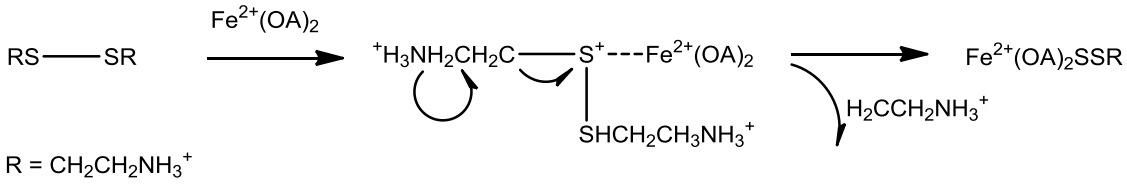

Finally, a catalytic reaction between the Fe(III) and the thiol occurs, repeating until the iron is completely bonded to sulfur and our sulfide green rust results.

(5) 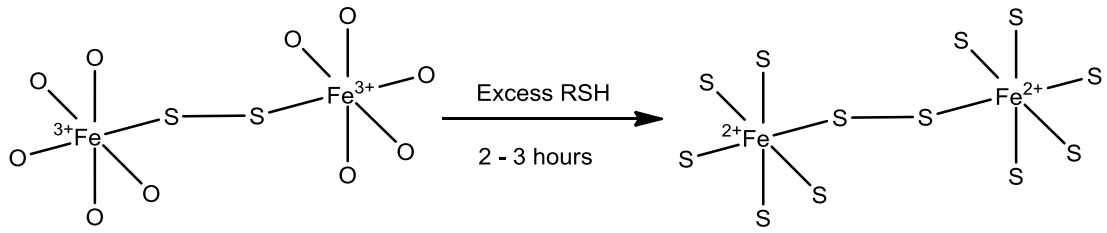

3.4 Conclusion

Iron sulfides are a diverse and complex material that have an interesting historical significance.[74] Using known literature FeS parameters for comparison, results from X-ray diffraction, Ultraviolet-Visible Spectroscopy, X-ray Photoelectron Spectroscopy, Raman spectroscopy, Cryo-TEM, and X-ray Absorption Spectroscopy suggest that sulfide green rust is an analog to the iron-oxyhydroxide green rusts. Structural and previously unknown mechanistic insight into the nature of the sGR are also presented, altogether providing another chapter in the history of reactive "green liquor" compounds formed when iron reacts with thiols.

3.5 Methods and Materials

Sulfide green rust reaction. 0.56 mL of the nanomagnetite solution in hexanes was dispensed into a 2 mL centrifuge vial. Solvent was redispersed in ODE to prevent evaporation during synthesis, usually aided by brief bath sonication (FS6 sonicator from Fischer Scientific). Next, 0.44 ml of a 2.0 M solution of aminoethanethiol*HCl (Sigma, 98 %) in methanol (EMD, 99.8 %) was added to the reaction vial to obtain a reactant/Fe

ratio of 30 (increasing the ratio is necessary for heavy characterization but risks aggregation; decreasing may lead to no reaction). This solution, which appeared increasingly green and cloudy, was shaken for 3 h with an Eppendorf Minispin + at 1100 rpm. A dark green precipitate formed during this time. Then, 1 ml of ultrapure water (Millipore, 18.2 MΩcm) was added to the solution and briefly shaken by hand to full dispersion, followed by 1 mL each of ethanol then ether (Decon Labs, 200 proof; Fisher, 99.9 %). This mixture was shaken well by hand and then centrifuged at 4,500 rpm for 30 min to form a very dark green supernatant and pellet. The supernatant was decanted and the pellet saved. 1 mL each of ultrapure water, ether, then ethanol was added again and the purification was repeated several more times, saving subsequent pellets and purifying them. The resulting samples were inverted onto a paper towel from five to ten minutes to dry and aid removal of any other leftover reactants and organics. The green solids were easily redispersed in 0.1-1 mL ultrapure water, although a brief 1-3 second bath sonication sometimes aided in this. Upon visual inspection the solutions were a brilliant emerald green.

Sulfide green rust reaction, without nanoparticles. Synthesis is mostly identical to the procedure without nanoparticles, except with iron oleate monomer replacing the nanomagnetite as the iron source.

Preparation of iron oleate monomer. Iron oleate monomer was prepared by combining iron oxide hydrated (FeOOH, catalyst grade, 30-50 mesh; 1 mmol, 0.09 g), oleic acid (OA, technical grade, 90%; 4 mmol, 1.12 g) and 1-octadecene (ODE, technical

grade, 90%; 15mmol, ~4g) and heating at 240 ^{o}C for 1h. The resulting black precipitate was purified using acetone, methanol, and hexane. 5ml of the resulting precipitate was washed using 25 mL of acetone and 25 mL of methanol and centrifuged at 4500 rpm for 30 min. The purification was repeated 3 times, then the black colloid was dissolved in 15 mL of hexane. The Fe concentration measured by ICP-AES to be 3 mg/mL.

Characterization. X-ray Diffraction was collected on a Rigaku D/Max Ultima II Powder Diffratometer. Solid green liquor/nanomagnetite powder samples were deposited onto a round, 5 mm diameter x 0.2 mm deep indented Rigaku zero-background holder. The sample was scanned for 5 h with the following settings: 0.5° 2θ divergence and scattering slits, a 10 mm divergence height limiting slit, a 0.15 mm receiving slit, a 0.1° 2θ step size, and a 21.1 s per step rate. Jade 9.0 was then used to analyze the resulting spectrum.

UV-Vis Spectroscopy was carried out using a Varian Cary 5000i UV-VIS-NIR Spectrophotometer. 20 µL of the sulfide-GR solution was added to 0.98 mL of water. This was then placed inside the spectrometer measuring a range of 225 to 800 nm. Measurement speed was 600 nm/min.

X-ray Photoelectron Spectroscopy was carried out on a PHI Quantera XPS using a substrate of indium foil at 140 eV (low resolution) for survey scans and 26 eV (high resolution) for elemental scans. 0.15 uL of sample was dropped onto the substrate an hour before introduction into the sample chamber. All scans utilized electron and ion

neutralizers. Using PHI Multipak 7.0, the spectrum was corrected using the adventitious carbon peak (284.5 eV) and peak multiplets were assigned.

Raman Spectroscopy was carried out on a Renishaw InVia Raman Microscope using a 633 nm laser with a 1800 lines/mm filter. Around 0.25 mL was dropped onto a glass slide and allowed to dry over the course of a few hours. Spectra were taken using a 50x lens with the laser set at 50% power for 20 s and averaged over 3 scans.

Infrared Spectroscopy was collected in a Jasco FT-IR 660 Plus Spectrometer using an ATR setup with a diamond substrate. 100 uL was dried onto the cleaned substrate and blown with nitrogen for 30 min to purge interferences. Spectra were run with a resolution of 4 cm^{-1} with averaging over 16 scans.

For CRYO TEM the Vitrobot was employed to prepare samples. 3 µL of the concentrated solution was applied each time in the Vitrobot to Quantumfoil 2x2 micron carbon grids, with a blotting time of 2.5 seconds. Cryo samples were then transferred to the Gatan 626 Cryo sample holder and observed in a TEM, specifically a JEOL 2011 with FasTEM operation software in MDS mode operating at 200KV.

The Fe K-edge (7112 eV) EXAFS measurements were done at MRCAT 10-ID beamline at the Advanced Photon Source, Argonne National Laboratory. [92] Fe edge measurements powder samples were mounted in plexiglass sample holders (5 mm diameter and 0.2 mm thick) for the fluorescence measurements. The iron standards needed for this experiment ($FeCl_3$, FeS pyrite, and Fe metal foil) were measured in transmission mode. The powders were spread on kapton tape and several layers were

stacked so that the thickness x of the samples corresponded to $\Delta\mu x = 0.5$, where $\Delta\mu$ is the edge step of the absorption coefficient at the Fe k-edge energy. Both for transmission and fluorescence measurements with ionization chambers, the Si(111) double crystal monochromator was scanned continuously so that the data was collected in quick EXAFS mode. 10 EXAFS scans were taken and then averaged for the liquid sample. The undulator parameters (taper and gap) were optimized to obtain a large photon flux with nearly constant intensity within the scanned energy range of 6900 to 8100 eV for the Fe edge. A Rh harmonic rejection mirror was used to eliminate X-Rays of higher harmonic energies. The incident ion chamber was filled with 20 % nitrogen mixed with 80 % helium gas whereas the transmission ion chamber was filled with nitrogen gas for proper adsorption. A reference ion chamber filled with the same gases as the transmission ion chamber was mounted behind the latter so as to record a standard spectrum of Fe foil with every scan to ensure that there is no energy shift between each scan. For fluorescence measurements, Lytle detector was filled with Argon gas. The size of the incident X-ray beam on the sample was 300 μm by 300 μm. The data was processed using Athena by extracting the XAFS oscillations $\chi(k)$ as a function of photoelectron wave number k following standard procedures.[93] The theoretical paths were generated using FEFF6 and the models were done in the conventional way using the fitting program called Artemis.[94] [95] Artemis was used to refine the fitting parameters used for modeling each sample in R-space until a satisfactory model describing the system was obtained. Data sets were simultaneously fitted in R-space with k-weights of 1, 2 and 3.

Chapter 4 Drinking Water Arsenic Removal Technology Assessment

In this chapter, focus is moved from the laboratory bench to a more holistic view of arsenic removal. Determining the best technology for a particular region and its unique water chemistry can sometimes be challenging, especially when financial constraints arise. A technology assessment is detailed, with environmental, technological, and economical information incorporated into the discussion. Social and cultural associations are also briefly illuminated.

4.1 Introduction

4.1.1 Arsenic health concerns

Long-term, human exposure drinking water studies have shown that arsenic is associated with liver, lung, kidney, skin, and bladder cancers. Additionally, other non-cancerous health effects include induction of micronuclei or chromosomal aberrations, DNA damage, sister chromatid exchange, peripheral vascular disease, diabetes mellitus, hypertension or ischaemic heart disease. [136,137] High groundwater concentrations of arseni are not a problem confined to only a few countries. Indeed, it is a public health issue in diverse communities including Argentina, Bangladesh, Canada, Chile, China, Hungary, India, Japan, Mexico, Poland, Taiwan, Thailand, USA, and Vietnam. [138,139] In rare cases arsenic contamination in water is anthropogenic; more common is the

contamination of drinking water through interaction of well water with arsenic-rich rocks.[140]

4.1.2 Hungarian situation

Hungary has one of the most alarming arsenic problems in Europe (Figure 4.1). As of 2001, around 1.5 million people consumed drinking water above 10 µg/L arsenic concentration, meaning an elevated arsenic concentration affects 14 % of the total Hungarian population and 13 % of all settlements.[141] This is because the country draws water resources from a deep confined aquifer in which arsenic levels are defined from natural interactions.[142] Here, arsenic is mostly found as arsenite (As(III)) due to the

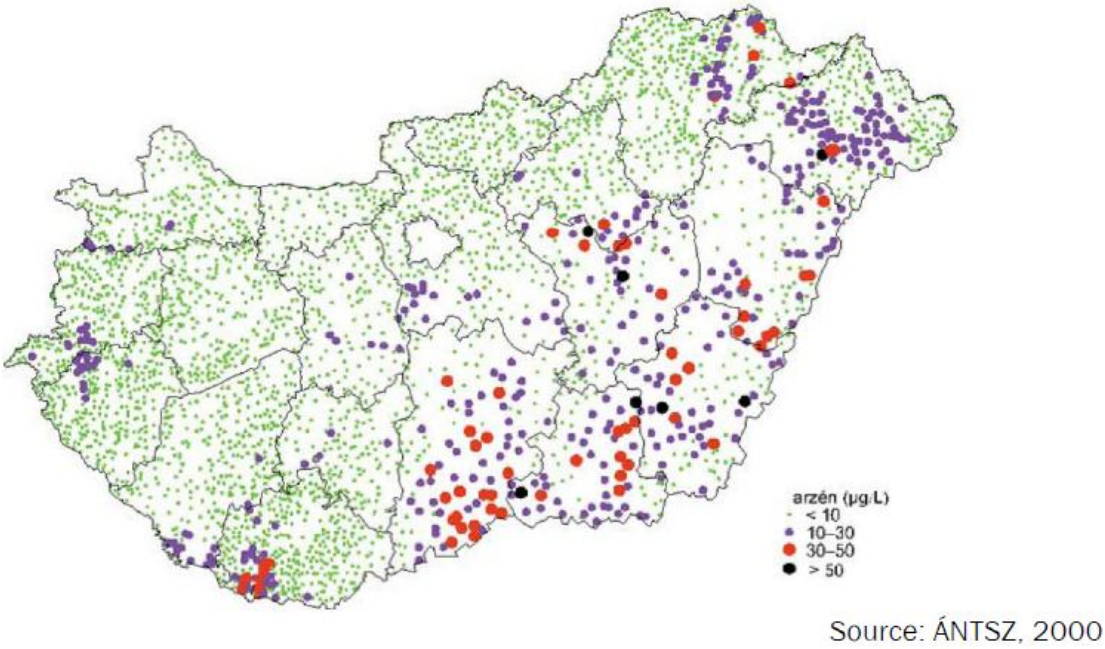

Figure 4.1. The majority of arsenic hotspots exist in the southeast of Hungary, in what is known as the Great Hungarian Plain Adapted from ANTSZ, (2000).

reducing conditions present. In 2001, new drinking water standards were introduced in Hungary that lowered the existing 50 μg/L arsenic standard to the corresponding 98/83 EU Directive (1998) level of 10 μg/L.[143,144] At many settlements, compliance with this standard is challenging. New drinking water treatment technology must be put into operation or existing systems have to be upgraded in the near future to provide a lasting and permanent solution for arsenic removal.

4.1.3 Technologies available

There are several existing technologies to remove arsenic. The most common in Hungary is the conventional coagulation-filtration method.[145,146] The technology consists of three steps: the oxidation of arsenite (As(III)) to arsenate (As(V)); the conversion of soluble arsenate to insoluble form by addition of metal salts (usually Fe(III) or Al(III)); and the subsequent removal of the solid particles from the water by sedimentation, rapid sand filtration or microfiltration.[147,148,146] Alternatively, adsorption may be used to reduce arsenic levels. In this technology, water passes through a media that binds to arsenic, thereby lowering arsenic in the water and concentrating it on the filter surface. Arsenic adsorbents available on the market or under investigation include both alumina and iron containing materials. According to the review of Mohan and Pittman (2007), iron based materials are usually capable of removing arsenic without pre-oxidation, while As(III) → As(V) conversion is needed for the alumina-based adsorbents.

Arsenic removal in Hungary currently proceeds via coagulation combined with rapid sand filtration; this is achieved through introduction of iron salts into the water or simply the reliance on the high *in-situ* concentrations of iron found in some areas. However, recent attention has been paid to other methods such as adsorption due to ease of operation, diminished chemical demand, and lower waste stream. However whether these benefits offset the costs of operation, infrastructure and sustainable processes are not apparent. Any insight into how these differences compare with regard to technical efficiency, financial burden, and environmental impact would aid decision makers in selecting the most suitable technology for a given location. Therefore, a methodology to compare and contrast such technological solutions for the Hungarian arsenic problem is of great value.

4.1.4 EU Directive

Beyond the health and technical issues of drinking arsenic-laden water are issues surrounding the EU Directive 10 μg/L arsenic level limit. The limit has not been met and is having additional adverse social effects, as seen in a recent study.[149] In short, while things are improving, settlements had not always been privy to convincing information behind the current arsenic limit and therefore saw it as a foreign mandate being imposed upon them. This has led to a certain pushback against infrastructure improvement. Another problem is that many Hungarians see their water as a historical resource of their region or municipality; some even claim beneficial, medicinal, or healing properties linked to their water. Indeed, in some regions people have refused to

drink water that has been purified of hazardous contaminants, claiming the water is "cloudy" or "tasting weird" and so therefore full of chemicals or bad for one's health, or simply unpalatable.[149] In one case, government officials in Hungary even acknowledged allowing the use of a clearly-marked, contaminated well by its people, not wanting to deny access to a historical resource. [149]

Aware of Hungary's financial burden associated with solving this problem, significant funds (in the millions of Euros) have been available for years in something called the "EU Water Improvement Fund." This fund was established to aid Hungary, without fear of accruing interest or even repayment, toward reaching its agreed-upon accession requirements in terms of water quality, including ammonia, arsenic, and other contaminant levels. Initially this fund required a small percentage of municipality financial support which, after difficulty in meeting the established goal timeline, has since been covered by the state of Hungary.

Currently the only financial burdens municipalities must withstand are those of the operation and maintenance required for any new technology installed. These costs are very much still relevant; however, the economic downturn of the last few years has made it more difficult to justify infrastructure upgrades. Municipalities and decision makers must make hard calls about how to spend limited funds.

4.1.5 Holistic comparison and the Life cycle analysis of (LCA)

A life cycle analysis, or LCA, methodology is one approach to comparing water treatment technologies and their overall impact and value. Similar studies have been

undertaken for comparing other water systems, including work on technologies for arsenic in wastewater and domestic water use in the US.[150,151] However, the LCA methodology has yet to be utilized to compare various arsenic technologies in drinking water.

A holistic analysis of two Hungarian arsenic removal technologies was conducted by employing the LCA methodology. This research addresses important questions about these technologies regarding the trade-offs with respect to cost, waste disposal, electricity consumption, global warming effects, and other environmental factors. Utilizing PE International's GaBi 5 software for database and organizational support, and incorporating detailed, quantitative data from manufacturers, it was possible to evaluate the systems-level impact of product production, use, and end-of-life phases. By providing a good comparison between products, with Hungarian wells and water parameters as a model, we demonstrate the benefits and drawbacks to each potential solution to the arsenic issue.

4.2 Methods

4.2.1 Goals and scope

The purpose of this LCA was to model and compare different strategies for removal of arsenic at a given site, with known given water quality conditions and demand. Two arsenic removal technologies were modeled: coagulation-filtration and a cerium based adsorption technology. The exact design of a drinking water treatment plant depends on a region's water chemistry, water demand and other conditions or

circumstances at that specific settlement. Therefore, in this study, realistic flow rates, arsenic concentrations, and initial raw water chemistry were important inputs. Calculations were completed for three different but realistic scenarios: a best, average, and worst-case with varying design parameters of favorable and less-favorable conditions for the technology at hand. In short, the best case scenario assumed optimum conditions for the removal of arsenic, e.g., few contaminants such as silicate or phosphate that interfere with removal, ideal pH, maximum lifespan performance of products used, etc.; the worst case assumed the maximum functional opposite values, while the average case sought a middle-ground between the two extremes.

4.2.2. Assessment Software

A number of LCA-related software exist, each with their own pros and cons. BEES (Building for Environmental and Economic Sustainability) and SimaPro, for instance, are two other prominent assessment tools available. BEES was available for free online, however its specificity to building products and lack of training support made this less feasible.[152] SimaPro might have been a good choice, however it was more expensive (one year license: $2354 for SimaPro, $1463 for GaBi) and other papers had already used GaBi with success for water-related studies.[153,154] GaBi 5 was therefore chosen for its ease of adaptability to our purposes, location of training centers in nearby Germany, large cache of environmental data, low cost, and efficient professional network.

4.2.3. Choice of Modeled Technologies

Several companies were contacted requesting a collaboration and data for an academic study. Unfortunately, all but one refused to engage us citing company policy regarding academic studies. Proprietary information was of great importance, and the one company that did choose to work with us required reassurances that exact production information would not be used.

4.2.4. Treatment Technologies

A schematic diagram of coagulation-filtration and adsorption methods is found in Figure 4.2. Coagulation technology consists of the following steps: water intake, aeration, oxidation by $KMnO_4$, coagulation by $FeCl_3$ salt, rapid sand filtration, and final disinfection. Aeration is often applied in deep confined aquifers where reductive conditions are dominant, and dissolved gases (methane or aggressive carbon-dioxide) might also be present in the water. Moreover, iron and some manganese can also be oxidized by dissolved oxygen. For arsenic removal a strong oxidant (e.g. $KMnO_4$) is needed; this is unlike iron oxide nanoparticle removal, where data indicates oxidation is not a necessary prestep$KMnO_4$ is also able to oxidize iron and manganese if these compounds were not efficiently oxidized by oxygen. $FeCl_3$ is used as a coagulant, and after mixing the chemical, the water is directed to the rapid sand filters, where iron, manganese and arsenic are filtered out. Backwash of the rapid sand filter is often required every 1-2 days to remove arsenic containing iron flocs, together with manganese and other contaminant flocs. The last step of the technology is final

disinfection (usually chlorine or sodium-hypochlorite is used) in order to prevent microbial growth in the water supply network.

Adsorption technology makes use of these steps in a similar manner. Following aeration, oxidation, and a small capacity rapid sand filter to remove excess iron and manganese, water is passed through adsorption columns. NaOH, NaClO and HCl are used for regeneration after saturation of the adsorbent; the regenerate must to be treated as hazardous waste while backwash water can be treated as normal sewage.

4.2.5 Modeling scenarios

Uniformly two important quantities were initially set for each scenario: a 500 m^3/day treated water volume to distribution, as this water quantity was near the average needed for affected Hungarian settlements, and a 50 μg/L arsenic level that agreed with the maximum allowable concentration according to the previous Hungarian arsenic standard.[141,143] All other design parameters and calculations were made according to typical Hungarian values and based on experiences of full and pilot-scale treatment plants; see Table 4.1 and 4.2 for coagulation and adsorption technology details, respectively. Important to note: both technologies were required to face common interferences found in Hungary equally, most importantly those of natural iron, manganese, phosphate, and humic content. Note that interferences will be addressed further in section 4.2.3. Best case scenario calculations for coagulation, for example, were based on raw water containing negligible iron and manganese; low-level potassium-permanganate oxidant and $FeCl_3$ levels (0.5 mg/L) were therefore sufficient

to convert the soluble arsenic to particulate form. To accurately determine backwash frequency and total flow, these values were then used to calculate a hypothetical tank design and filtration area based on the Hungarian Technical Guidelines (MI-10-135-4: 1981) and Mészáros G. (1998).[155,156] Low amounts of particulate iron and manganese generate a relatively low 1.25 mg/L floc density, so a 8 m/h filtration velocity was assumed, resulting in 2.5 m^2 filtration area. The loading capacity of the filter was assumed to be 1000 g/m^2. These values resulted in a backwash frequency of 100 hours; however, it is recommended that the filters are backwashed at least every second day, so a 48 hour of backwash frequency was applied.[155] Backwash was carried out with around 15 m/h intensity and lasts about half an hour. Besides water, the rapid sand filters were backwashed with air of 60 m/h intensity for 10 minutes.

Subsequently, the average and worst case scenarios increased their modeled interferences. In the average scenario, 1 mg/L natural iron and 1 mg/L natural manganese content were assumed with 2 mg/L added iron coagulant; the worst case scenario contained 3 mg/L natural iron and 2.5 mg/L manganese. In the latter case we assumed that an additional 3 mg/L iron was needed due to the level of arsenic and unfavorable quality of the water, in spite of the fact that 3 mg/L of *in-situ* coagulant was already present in the water as coagulant. A relatively high oxidant demand (10 mg/L $KMnO_4$) was also assumed, which is not rare to use in Hungarian waters due to the high humic and phosphate content found at many water sources.[157] Finally, due to the high floc density in this scenario and in order to achieve the required minimum backwash frequency of 24 hours, the filter depth was increased and dual-density sand having a

high 1700 g/m^2 loading capacity was used to mimic a two-tank solution using a double-layered rapid sand filter.

Scenario design for the adsorption technology proceeded similarly. For the best case scenario, cost and shipping was calculated based on the assumption the adsorbent is produced in Hungary, while in the other scenarios production abroad was assumed. All water conditions were identical: aeration, rapid sand filtration, and chemical oxidation were applied for iron and manganese removal for the technology to be "functional and feasible" in the average and worst case scenario, while the best case scenario did not include this prefiltration. Adsorbent regeneration would also vary depending on the arsenic content of the well and presence of other competing ions, e.g. phosphate ion concentration. More frequent regenerations may be required, therefore the industry suggested the best and average case scenarios include 3 regenerations a year, while the worst case assumed 4 regenerations. Backwash for the adsorbent filter was also recommended weekly.

Waste was handled almost identically for each scenario, aside from the resulting quantity. In the case of coagulation-filtration, backwash water was directed to a sedimentation tank and allowed to reach a 1% total mass, arsenic-containing hazardous sludge was remaining. The supernatant from the sedimentation tank was directed to a nearby river or urban drainage system (collecting rainwater), while the hazardous waste (1 % sludge) was stored at a hazardous waste disposal site. In the case of adsorption, no concentration process has yet been applied from the industry data source. Additionally,

any rapid sand filtration in the adsorption model also used the 1% concentration method applied in coagulation-filtration to remove hazardous flocs.

4.2.6 LCA Methodology

Boundary conditions for the model included only steps necessary for arsenic treatment. Infrastructure, which is currently not an issue municipalities in Hungary are required to support, and spare parts were not considered in the model. Additionally, steps that are necessary but unassociated with arsenic removal, or identical in both technologies such as chlorination disinfection, were neglected. In Figure 4.2, blue boxes indicate steps which were included, and red boxes indicate the excluded steps. Some steps also relied on calculations from partially available or assumed data due to high financial cost for data or lack of information; their boxes are marked by diagonal cross-hatching, and detailed in Tables 4.1 and 4.2.

Technologies were studied using GaBi 5, a software made commercially available from PE International; its professional database was used as a source for datasets on production of chemicals, energy, and transportation as well as European environmental impact information. Inputs for the individual technologies, and details regarding their operation, are from industrial sources and pilot/full-scale systems. Variations in these scenarios listed in Tables 4.1 and 4.2 can be seen as error bars, illustrating the effects of dynamic water chemistries and technology differences

Impact analysis was conducted on categories of global warming, eutrophication, ozone layer depletion, acidification, human toxicity, terrestrial toxicity, freshwater

aquatic toxicity, and marine aquatic toxicity potentials, as well as abiotic depletion of elements and fossil fuels. Each of the categories use an equivalence method calculated

Figure 4.2. Coagulation-filtration (a) and adsorption (b) model scheme (blue boxes are included in model, red boxes are excluded, and cross-hatched boxes have partial data).

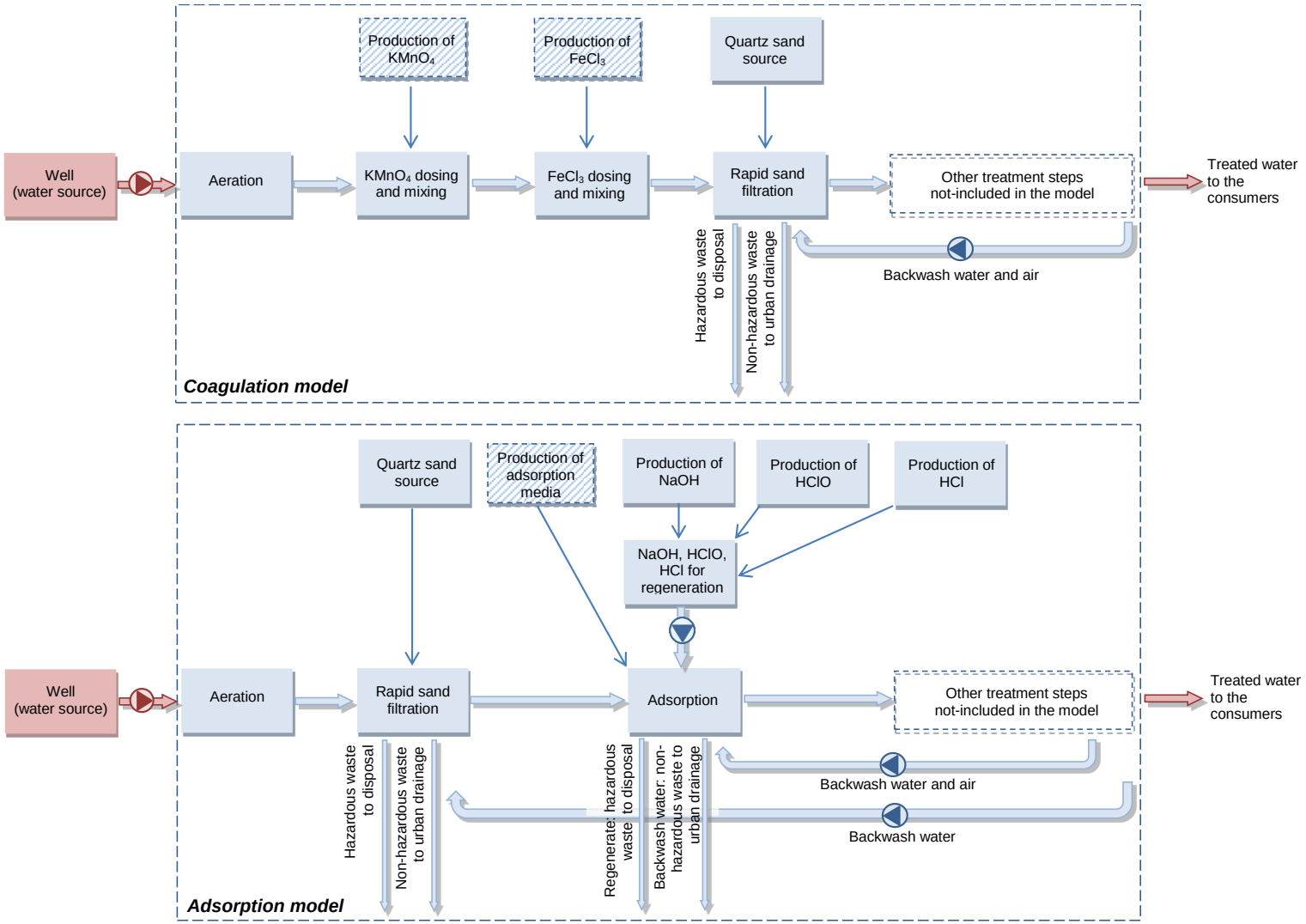

to evaluate potential environmental impact; this technique is then used to compare each chemical or material that is consumed or emitted in the model from cradle-to-grave. [158,159]

Table 4.1. Design parameters used in GaBi and scenario descriptions of the coagulation-filtration technology.

Design parameters	*Good scenario*	*Average scenario*	*Worst scenario*	*Unit*	*Parameter Comments*
Initial water quality					
Initial arsenic concentration	50	50	50	µg/L	Uniform initial value; municipalities already meant to meet this value
Initial (natural) iron concentration	negligible	1.0	3.0	mg/L	Uniform initial value
Initial (natural) manganese concentration	negligible	1.0	2.5	mg/L	Uniform initial value
Water quantity					
Input flow rate	509	539	553	m^3/day	Calculated by iteration; based on treated water flow rate & backwash demand
Treated water flow rate	500	500	500	m^3/day	Uniform initial value
Design parameters					
Air oxidant used	40.8	43.1	44.2	Nm^3/day	8% total flow
$KMnO_4$ dose	0.5	3.0	10.0	mg $KMnO_4$/L	Assumed; based on typical values; *partial data in model*
$FeCl_3$ coagulant dose	0.5	2.0	3.0	mg Fe/L	Assumed; based on typical values; *partial data in model*
Filtration velocity	8.5	4.3	3.3	m/h	Assumed; based on typical values
Filtration area	2.5	5.2	7.0	m^2	Calculated; input flow rate divided by filtration speed
Filter layer depth	1.5	1.5	2	m	Assumed; based on typical values; worst case assumes two layer, dual-density sand)
Sand filter volume	3.75	8.1	14.0	m^3	Calculated; filtration area multiplied by depth of filter layer
Floc concentration	1.25	9.5	23	mg/L	Calculated; 1 mg/L dissolved iron or manganese forms 2 mg/L Mn and Fe flocs; 1 mg/L added $KMnO_4$ forms 0.5 mg/L Mn-flocs
Filter sand loading capacity	1000	1000	1700	g/m^2	Assumed; based on typical values; worst case assumes two layer, dual-density sand)
Calculated RSF BW frequency	96	24	26	hours	Calculated; loading capacity of the filter divided by the filtration velocity and total concentration of flocs
Req'd backwash frequency	48	24	24	hours	Backwash is needed at least after 48 hours of operation
Req'd backwash volume per day	9.4	39.0	52.0	m^3/day	Calculated; filtration area x 15 m/h backwash intensity and 0.5 hours of backwash; BW req'd every 2nd day in best case
Backwash air used per day	25	52	70	Nm^3/day	Calculated; filtration area x 60 m/h backwash air intensity for 10 minutes; BW req'd every 2nd day in best case
Percent backwash of total purified water	1.8	7.5	9.4	%	Calculated; amount of backwash water divided by input flow rate

Hazardous waste annually	34.1	142.0	191.1	m^3	Calculated; 1 % of the amount of BW water per day multiplied by 365 days
Non-hazardous waste annually	3378	14054	18919	m^3	Calculated; 99% of BW per day
Energy demand					
Pumping of backwash water	412.02	824.04	824.04	MJ/year	Calculated*
Req'd mixing	226.59	353.15	396.4	MJ/year	Assumed TETRAMIX static mixer
Shipping distances					
$FeCl_3$ coagulant	negligible	210	2180	km	Assumed; shipping is 1, 2, and 4 times a year for the good, average, and worst, respectively
$KMnO_4$ oxidant	negligible	210	2180	km	Assumed; shipping is 1, 2, and 4 times a year for the good, average, and worst, respectively
Quartz sand	negligible	210	545	km	Assumed; 1 shipment; replacement in every eight years

*For the calculation of energy demand the following equations were used:
P(watts) = flow capacity (Q) x fluid density (p) x gravity (g) x height differential (ΔH) / time conversion; E(joules) = P x t

4.3 Results and Discussion

4.3.1 Environmental Observations

Each impact category is broken down into its greatest contributors in Figures 4.3-4.6.

A key observation would be the lack of effect caused by electricity use, both independently and relatively between the technologies. Electricity has been identified as one of the greatest contributors to the environmental impact of water treatment, however as seen in Figures 4.2-4.6, it does not appear once as a top factor in environmental impact.[160,154] This does not say electricity is without impact overall; pumping of water alone over a year is, for example, creates a huge electrical demand. Initial attempts at modelling included plant-wide electricity pumping demand, and here electricity demonstrated its expected majority impact contribution to categories such as

Table 4.2. Design parameters used in GaBi and scenario descriptions of the adsorption technology.

Design parameters	*Good scenario*	*Average scenario*	*Worst scenario*	*Unit*	*Parameter Comments*
Initial water quality					
Initial arsenic concentration	50	50	50	µg/L	Uniform initial value; municipalities already meant to meet this value
Natural iron concentration	negligible	1.0	3.0	mg/L	Uniform initial value
Natural manganese concentration	negligible	1.0	2.5	mg/L	Uniform initial value
Water quantity					
Input flow rate	502	524	532	m^3/day	Calculated by iteration; based on treated water flow rate & both backwash demands
Treated water flow rate	500	500	500	m^3/day	Uniform initial value; based on typical values
Design parameters					
Oxidant air used	0	43.3	44.4	Nm^3/day	8% total flow
$KMnO_4$ dose	0	2.5	8	mg $KMnO_4$/L	Assumed; based on typical values; *partial data in model*
Filtration velocity	0	7.52	5.52	m/h	Assumed; based on typical values
Filtration area	0	2.90	4.02	m^2	Calculated; input flow rate divided by filtration speed
Filter layer depth	0	1.5	2.0	m	Assumed; based on typical values; worst case assumes two layer, dual-density sand)
Sand filter volume	0	4.35	8.04	m^3	Calculated; filtration area multiplied by depth of filter layer
Floc concentration	0	5.25	15	mg/L	Calculated; 1 mg/L dissolved iron or manganese forms 2 mg/L Mn and Fe flocs; 1 mg/L added $KMnO_4$ forms 0.5 mg/L Mn-flocs
BW air used	0	52	70	Nm^3/day	Calculated; filtration area x 60 m/h backwash air intensity for 10 minutes; BW req'd every 2nd day in best case
Calculated RSF BW frequency	0	25.4	24.2	hours	Calculated; loading capacity of the filter divided by the filtration velocity and total concentration of flocs;
Chosen RSF BW frequency	0	7	24	hours	
Adsorbent BW frequency	7	5	7	day	Provided by industry
Req'd adsorbent BW volume	5	5	5	m^3	Provided by industry
Percent BW of total purified water annually	<1	4.5	6.0	%	Provided by industry and calculated
Regenerations annually	3	3	4	-	Provided by industry
Regeneration water demand	162	162	216	m^3/year	Provided by industry
NaOH (25%) for regeneration	14440	14400	19200	L/year	Provided by industry
NaClO (12 %) for regeneration	171	171	228	L/year	Provided by industry; *partial data in model*
HCl (35 %) for regeneration	267	267	356	L/year	Provided by industry
Regeneration Wastewater	99.6	99.6	132.8	m^3/year	Provided by industry

Hazardous waste annually	55.0	144.0	196.1	m^3/year	Provided by industry and calculated; 1% of RSF BW and all regen waste
Non-hazardous waste annually	698	8535	11596	m^3	Calculated; all adsorbent BW
Energy demand					
Pumping of backwash water	39.24	863.28	863.28	MJ/year	Calculated
Regeneration	151.35	151.35	201.4	MJ/year	Provided by industry
Req'd mixing	0	353.15	396.4	MJ/year	Assumed TETRAMIX static mixer
Shipping distances					
Adsorbent	210	9000	9000	km	Assumed; 1 shipment; replacement every 10 years (good and average scenario), 7 years (worst scenario);
Quartz Sand	negligible	210	545	km	Assumed; 1 shipment; replacement in every eight years
NaOH solution (25%)	negligible	210	2180	km	Assumed; shipping is 1, 2, and 4 times a year for the good, average, and worst, respectively
NaClO solution (12%)	negligible	210	2180	km	Assumed; shipping is 1, 2, and 4 times a year for the good, average, and worst, respectively
HCl solution (12%)	negligible	210	2180	km	Assumed; shipping is 1, 2, and 4 times a year for the good, average, and worst, respectively

global warming potential (GWP). However, as pumping is required for any plant to function regardless of the technology installed, this was treated as external to our LCA focus and neglected in the rest of the study. Electricity still has an effect from within production of materials involved in this study, but the point is that it was not as a direct consequence of arsenic removal technology.

Shipping and handling for products and the associated fuel production were major contributors in several impact categories (Figure 4.4, 4.5), leading to two observations. Firstly, coagulation-filtration had roughly half the impact of adsorption in several impact categories; this was due to the number of products and larger quantities required by the adsorption technology. These impacts can be greatly reduced by procuring materials near to a plant and within Hungary, shipping in bulk, and combining goods in one shipment. Secondly, it is worth noting that the total mass required for one

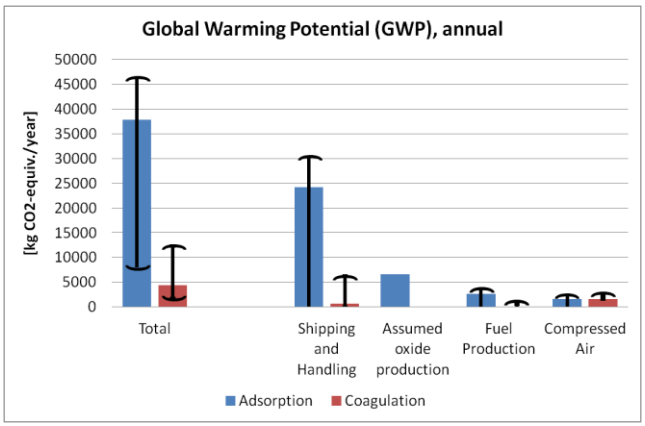

Substance	GWP_{100} CO_2-Equiv
CO_2	1
Methane	21
CFCs	4000

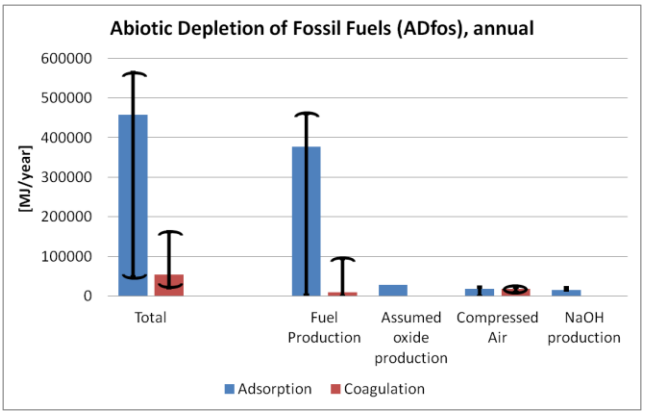

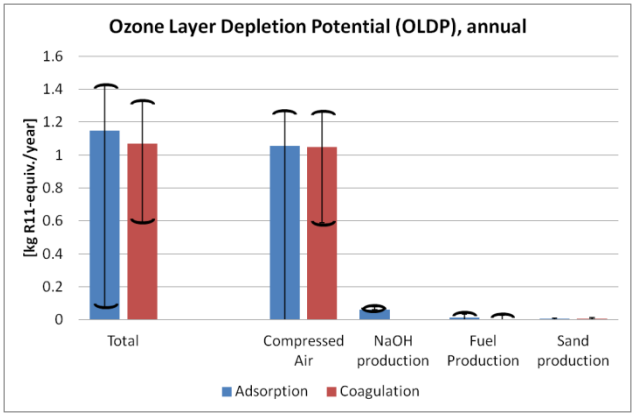

Figure 4.3. Environmental impact assessment from the top 4 contributors in each category. Note that electricity is not a major direct contributor. An equivalence method for each category is applied to chemicals and materials in accordance with International Organization for Standardization (ISO) and Institute of Environmental Sciences (CML) methods. An example of the equivalence method is given (*top right*); carbon dioxide is set as a standard value and other compounds are given relative values through the cited ISO method. [158,101] Note: scale bars represent extremes resulting from calculated best, average, and worst case scenarios and do not have relation to standard deviation.

regeneration was nearly the quantity required to support coagulation-filtration for an entire year. As such, reducing the sorption capacity of the sorbents would greatly minimize this shipping burden and overall impact.

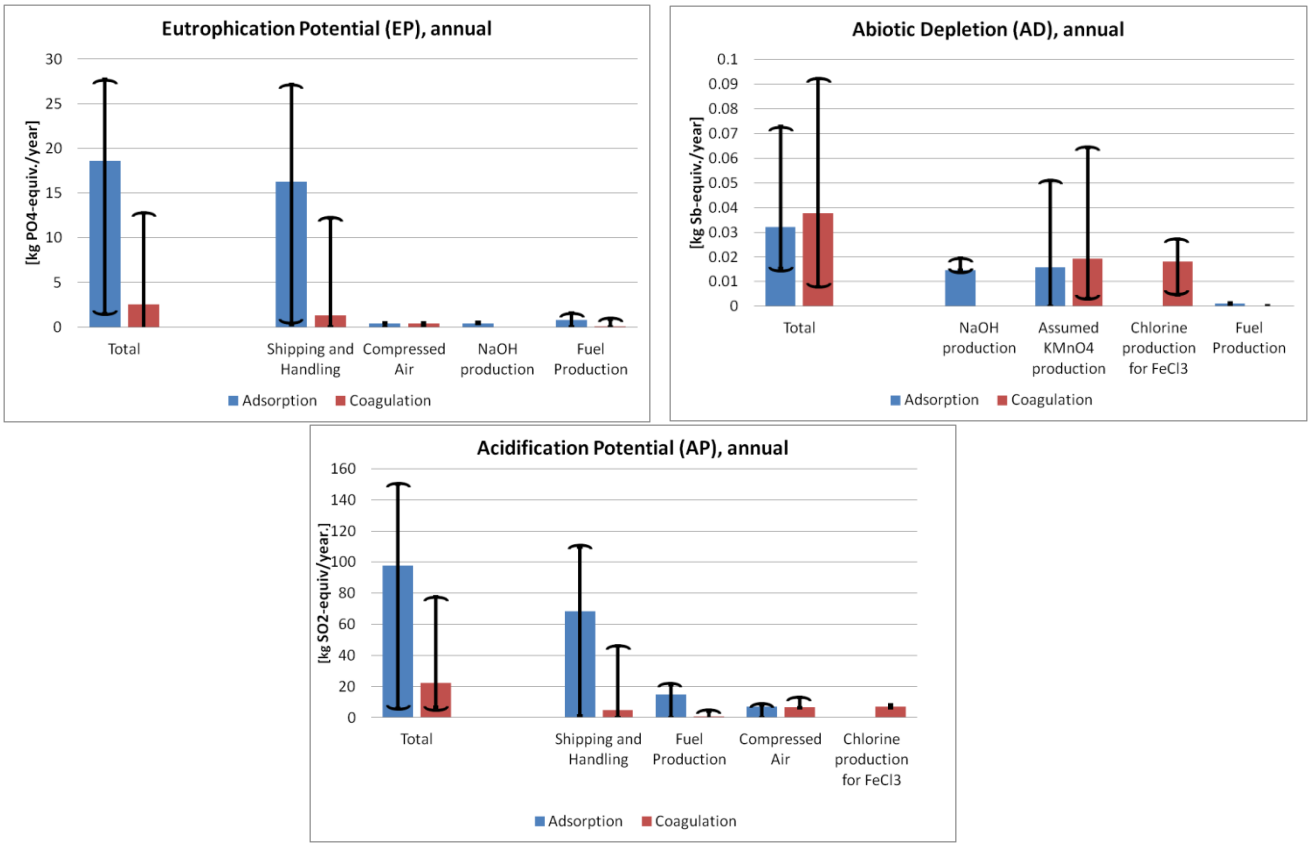

Figure 4.4. Abiotic depletion of non-fossil fuels (*top right*) is the only category with greater impact that adsorption in the average case; however, overlap and therefore variability is high. Additionally, a key contributor to this graph is from an assumed value. Note: eutrophication potential is defined as a risk associated for an environmental response due to the process or chemical introduced; acidification potential is same however the concern is with rising acidity. [161, 162]

It is important to note that a more generalized model without a connection to a real-world scenario, comparing only technical aspects, might exclude this shipping and handling impact. In this study, one technology had several chemical requirements and a finite, international shipping requirement; the other had neither. Including this information is crucial in accounting for the impact due to the operation of these

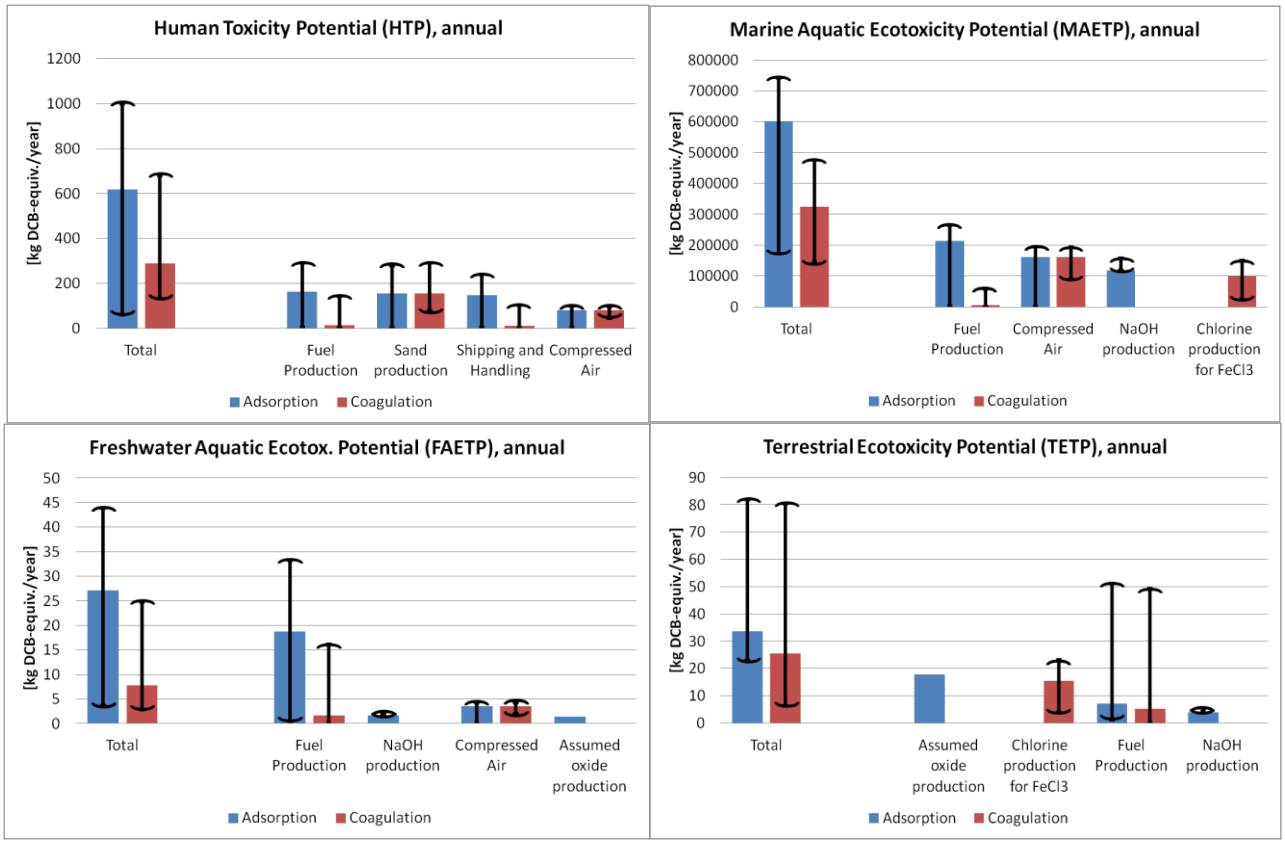

Figure 4.5. In our case, adsorption technology shifts impacts to pre-operational phases in comparison to coagulation-flocculation. Fuel production is the first contributor to three of the potentials; this is due to shipping requirements. Note: ecotoxicity potentials are defined as the risk associated for negative impact on life due to the process or chemical introduced.[163]

technologies, such as the vast effects of air freight. One could also use this example as a benchmark, comparing the environmental effect of arsenic removal against such shipping and handling impacts

A subject of much debate is hazardous waste management (Figure 4.6). Under "ideal" best case water conditions, coagulation-filtration was capable of producing

nearly half the waste of the adsorption. However, both technologies produced relatively the same amount of hazardous waste in average and non-ideal worst case scenarios. Additionally, this particular adsorption technology did not have a standardized waste concentration technique. Such a process is an important tool in mitigating waste and lowering environmental impact and cost; prefilters, however, did apply a 1% concentration technique also used seen in coagulation-filtration as the technology is similar.

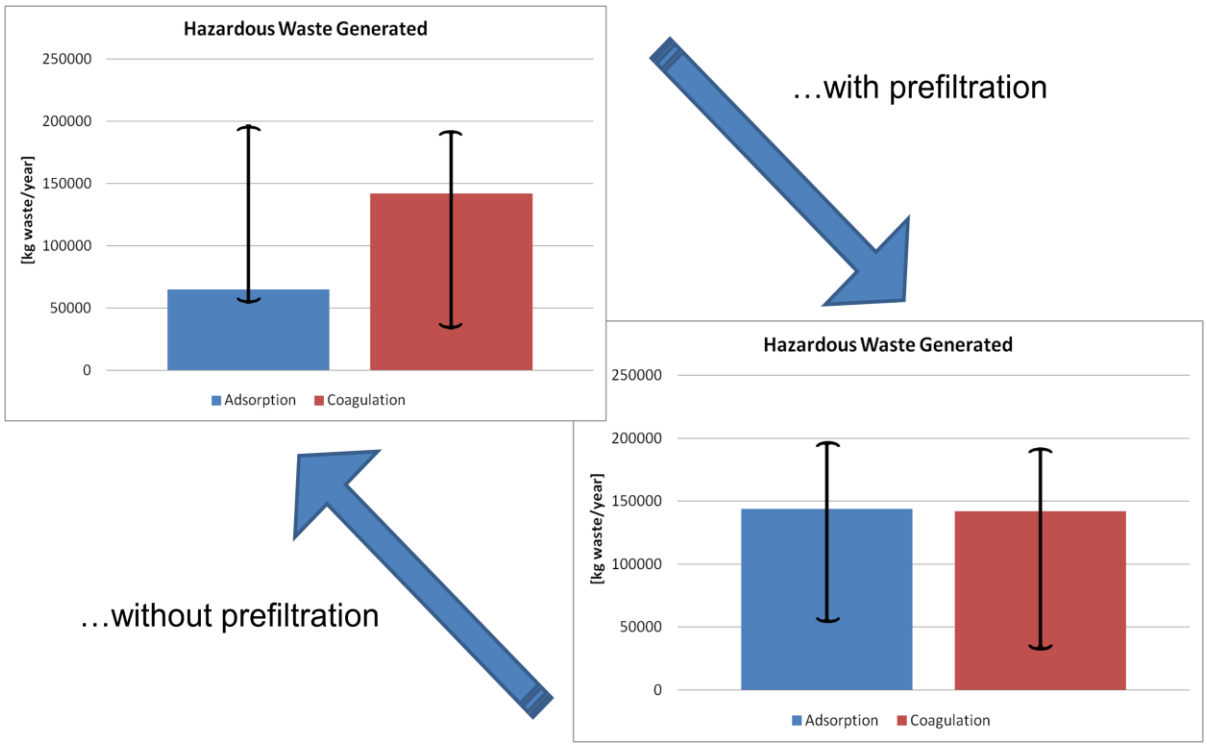

Figure 4.6. Focus on hazardous waste management is key in solving arsenic remediation concerns. Hazardous waste production for both technologies is about the same in non-ideal scenarios. Under the normal Hungarian conditions modeled, interferences clog adsorption columns over time, thus requiring a prefilter producing hazardous waste that negates gained benefits.

Finally, in modelling these technologies, one major drawback was the lack of validated production information. Assumptions had to be made to fill this information gap, with remarkable consequences as seen in GWP in Figure 4.3. The assumed production for the adsorbent is a common, easily produced oxide; note this is one of the highest contributors to GWP. This value could be lower for the actual material, but it is possible that more uncommon or difficult to make products would generate several times to orders of magnitude higher an impact. Gaining an accurate representation of the technology landscape will require consideration of other approaches to the arsenic problem, as well as engagement from industries in such studies.

4.3.2 Cost Analysis

The two technologies modeled differ greatly in the location of their greatest financial burden, as illustrated in Table 4.3. Coagulation-filtration was the cheaper of the two technologies; its largest expense in proper hazardous waste disposal, and excessively so in the worst case scenario. Foreign-purchased adsorbent media in the adsorption worst case scenario was the single most expensive line item in the study.

Costs could also be significantly reduced through a number of changes. Regenerations for the media were costly due to high chemical demand; sodium hydroxide itself made up nearly 96% of the regeneration expense. Reduction of all shipping distances and other quantities of the various chemicals required would also decrease costs. Many prices, however, are difficult to reduce for water systems with high arsenic loads. Factors such as the potassium permanganate for arsenic oxidation

Table 4.3. Annual cost-analysis comparing modeled operation-phase coagulation-filtration, in Hungarian forints and euros. System was built off expenditures for a plant with a daily water distribution of 500 m^3/day. The forint to euro rate of 303 as ft/euro of 20 January 2012 was used.

	Coagulation-filtration					
	Good scenario		*Average scenario*		*Worst scenario*	
Design parameter	*Forint*	*Euro*	*Forint*	*Euro*	*Forint*	*Euro*
Quartz sand	20000	66	40000	131	75000	246
$FeCl_3$ coagulant	597455	490	149364	1959	896182	2938
Adsorbent media	-	-	-	-	-	-
$KMnO_4$ oxidant	88288	289	529729	1737	1765764	5789
All regeneration chemicals	-	-	-	-	-	-
NaOH	-	-	-	-	-	-
NaHClO	-	-	-	-	-	-
HCl	-	-	-	-	-	-
Energy for mixing	1669	5	2715	9	2715	9
Energy for sand filter backwash	3090	10	6180	20	6180	20
Energy for sorbent filter backwash	-	-	-	-	-	-
Energy for regeneration	-	-	-	-	-	-
Hazardous Waste Disposal	1706250	5594	7153090	23453	9555000	31328
Total operational costs per year	1970329	8290	8331752	34715	12303556	51264
Technology contribution to cost of 1 m^3 water to users	***10.63***	***0.03***	***42.47***	***0.14***	***61.18***	***0.20***

Table 4.4. Annual cost-analysis comparing modeled operation-phase adsorption technologies, in Hungarian forints and euros. System was built off expenditures for a plant with a daily water distribution of 500 m^3/day. The forint to euro rate of 303 as ft/euro of 20 January 2012 was used.

	Adsorption					
	Good scenario		*Average scenario*		*Worst scenario*	
Design parameter	*Forint*	*Euro*	*Forint*	*Euro*	*Forint*	*Euro*
Quartz sand	-	-	40000	131	75000	246
$FeCl_3$ coagulant	-	-	-	-	-	-
Adsorbent media	5775000	18934	7150000	23443	10214286	33489
$KMnO_4$ oxidant	-	-	438883	1406	1394679	4573
All regeneration chemicals	1730721	5674	1730721	5674	2307628	7566
NaOH	1656000	5430	1656000	5430	2208000	7239
NaHClO	20520	67	20520	67	27360	90
HCl	54201	178	54201	178	72268	237
Energy for mixing	-	-	2715	9	2715	9
Energy for sand filter backwash	-	-	6180	20	6180	20
Energy for sorbent filter backwash	294	1.0	294	1.0	294	1.0
Energy for regeneration	111	0.4	111	0.4	149	0.5
Hazardous Waste Disposal	2750000	9016	7198500	23602	9807300	32155
Total operational costs per year	10256127	33626	16554690	54278	23805516	78051
Technology contribution to cost of 1 m^3 water to users	***56.35***	***0.18***	***86.85***	***0.30***	***130.80***	***0.43***

or the amount of sand in the filter tank, are somewhat fixed expenses. Future technologies may reduce, extract, or make use of hazardous chemicals from waste, thereby lowering these costs.

4.4 Conclusions

Coagulation-filtration and cerium adsorption technologies were modeled via an LCA approach and compared across several important categories including cost and environmental impact. Nine out of ten considered LCA environmental impact categories favor coagulation, however the relative magnitude of the benefits varied substantially with the water chemistry and site constraints. A smaller waste impact from adsorption operation was countered by large impacts generated in production and delivery; .

Regeneration was observed to be the single most costly, chemically demanding, and environmentally taxing process in the application of arsenic sorbent technologies. In one cycle, regeneration required the material quantity used by coagulation-filtration technology over an entire year. Efforts by producers of adsorption media to reduce the number and cost of required regenerations, as well as efforts to produce adsorption media locally, would substantially increase their appeal to municipalities.

This study used LCA methodology to enumerate and evaluate the numerous technical, economical, and environmental concerns that must be balanced when choosing an arsenic removal technology. Given their local water conditions, municipalities might use this study to examine and compare what operational setup will work best for them. However, no “magic bullet” to arsenic contamination has yet been

found for all water conditions, and individual choices to address challenges in managing the hazardous waste stream may continue to drive decisions for these communities.

REFERENCES

1. Erbs, M.; Hansen, H. C. B.; Olsen, C. E., Reductive dechlorination of carbon tetrachloride using iron(II) iron(III) hydroxide sulfate (green rust). *Environmental Science & Technology* **1999,** *33* (2), 307-311.

2. Matta, R.; Hanna, K.; Kone, T.; Chiron, S., Oxidation of 2,4,6-trinitrotoluene in the presence of different iron-bearing minerals at neutral pH. *Chem. Eng. J.* **2008,** *144* (3), 453-458.

3. Choi, J.; Batchelor, B., Nitrate reduction by fluoride green rust modified with copper. *Chemosphere* **2008,** *70* (6), 1108-1116.

4. Chun, C. L.; Hozalski, R. M.; Arnold, W. A., Degradation of disinfection byproducts by carbonate green rust. *Environmental Science & Technology* **2007,** *41* (5), 1615-1621.

5. O'Loughlin, E. J.; Kelly, S. D.; Cook, R. E.; Csencsits, R.; Kemner, K. M., Reduction of Uranium(VI) by mixed iron(II/iron(III) hydroxide (green rust): Formation of UO2 manoparticies. *Environmental Science & Technology* **2003,** *37* (4), 721-727.

6. Pepper, S. E.; Bunker, D. J.; Bryan, N. D.; Livens, F. R.; Charnock, J. M.; Pattrick, R. A. D.; Collison, D., Treatment of radioactive wastes: An X-ray absorption spectroscopy study of the reaction of technetium with green rust. *J. Colloid Interface Sci.* **2003,** *268* (2), 408-412.

7. Bernal, D., and Mackay, The oxides and hydroxides of iron and their structural inter-relationships. *Clay Miner. Bull* **1958,** *(website temp down)*.

8. Ma, R. Z.; Liu, Z. P.; Takada, K.; Iyi, N.; Bando, Y.; Sasaki, T., Synthesis and exfoliation of Co2+-Fe3+ layered double hydroxides: An innovative topochemical approach. *J. Am. Chem. Soc.* **2007,** *129* (16), 5257-5263.

9. Wiesli, R. A.; Beard, B. L.; Johnson, C. M., Experimental determination of Fe isotope fractionation between aqueous Fe(II), siderite and "green rust" in abiotic systems. *Chem. Geol.* **2004,** *211* (3-4), 343-362.

10. Sabot, R.; Jeannin, M.; Gadouleau, M.; Guo, Q.; Sicre, E.; Refait, P., Influence of lactate ions on the formation of rust. *Corrosion Science* **2007,** *49* (3), 1610-1624.

11. Genin, J. M. R.; Refait, P.; Bourrie, G.; Abdelmoula, M.; Trolard, F., Structure and stability of the Fe(II)-Fe(III) green rust "fougerite" mineral and its potential for reducing pollutants in soil solutions. *Appl. Geochem.* **2001,** *16* (5), 559-570.

12. Trolard, F.; Bourrie, G.; Abdelmoula, M.; Refait, P.; Feder, F., Fougerite, a new mineral of the pyroaurite-iowaite group: Description and crystal structure. *Clays and Clay Minerals* **2007,** *55* (3), 323-334.

13. Sandstrom, M.; Jalilehvand, F.; Persson, I.; Gelius, U.; Frank, P.; Hall-Roth, I., Deterioration of the seventeenth-century warship Vasa by internal formation of sulphuric acid. *Nature* **2002,** *415* (6874), 893-897.

14. Trolard, F.; Genin, J. M. R.; Abdelmoula, M.; Bourrie, G.; Humbert, B.; Herbillon, A., Identification of a green rust mineral in a reductomorphic soil by Mossbauer and Raman spectroscopies. *Geochim. Cosmochim. Acta* **1997,** *61* (5), 1107-1111.

15. McNeill, L. S.; Edwards, M., Iron pipe corrosion in distribution systems. *J. Am. Water Work Assoc.* **2001,** *93* (7), 88-+.

16. Refait, P.; Memet, J. B.; Bon, C.; Sabot, R.; Genin, J. M. R., Formation of the Fe(II)-Fe(III) hydroxysulphate green rust during marine corrosion of steel. *Corrosion Science* **2003,** *45* (4), 833-845.

17. Pineau, S.; Sabot, R.; Quillet, L.; Jeannin, M.; Caplat, C.; Dupont-Morral, I.; Refait, P., Formation of the Fe(II-III) hydroxysulphate green rust during marine corrosion of steel associated to molecular detection of dissimilatory sulphite-reductase. *Corrosion Science* **2008,** *50* (4), 1099-1111.

18. Zegeye, A.; Bonneville, S.; Benning, L. G.; Sturm, A.; Fowle, D. A.; Jones, C.; Canfield, D. E.; Ruby, C.; MacLean, L. C.; Nomosatryo, S.; Crowe, S. A.; Poulton, S. W., Green rust formation controls nutrient availability in a ferruginous water column. *Geology* **2012,** *40* (7), 599-602.

19. Refait, P. H.; Abdelmoula, M.; Genin, J. M. R., Mechanisms of formation and structure of green rust one in aqueous corrosion of iron in the presence of chloride ions. *Corrosion Science* **1998,** *40* (9), 1547-1560.

20. Peulon, S.; Legrand, L.; Antony, H.; Chausse, A., Electrochemical deposition of thin films of green rusts 1 and 2 on inert gold substrate. *Electrochem. Commun.* **2003,** *5* (3), 208-213.

21. Peulon, S.; Baraize, Q.; Chausse, A., Iron compounds electrodeposited onto a transparent semiconductor: Synthesis and characterisation by UV-vis spectroscopy. *Electrochim. Acta* **2007,** *52* (27), 7681-7688.

22. Ruby, C.; Gehin, A.; Abdelmoula, M.; Genin, J. M. R.; Jolivet, J. P., Coprecipitation of Fe(II) and Fe(III) cations in sulphated aqueous medium and formation of hydroxysulphate green rust. *Solid State Sci.* **2003,** *5* (7), 1055-1062.

23. Gehin, A.; Ruby, C.; Abdelmoula, M.; Benali, O.; Ghanbaja, J.; Refait, P.; Genin, J. M. R., Synthesis of Fe(II-III) hydroxysulphate green rust by coprecipitation. *Solid State Sci.* **2002,** *4* (1), 61-66.

24. Misawa, T.; Hashimot.K; Shimodai.S, Formation of Fe(Ii)1-Fe(Iii)1 Intermediate Green Complex on Oxidation of Ferrous Ion in Neutral and Slightly Alkaline Sulfate Solutions. *Journal of Inorganic & Nuclear Chemistry* **1973,** *35* (12), 4167-4174.

25. Drissi, S. H.; Refait, P.; Abdelmoula, M.; Genin, J. M. R., The Preparation and Thermodynamic Properties of Fe(Ii)-Fe(Iii) Hydroxide-Carbonate (Green-Rust-1) - Pourbaix Diagram of Iron in Carbonate-Containing Aqueous-Media. *Corrosion Science* **1995,** *37* (12), 2025-2041.

26. Ona-Nguema, G.; Abdelmoula, M.; Jorand, F.; Benali, O.; Gehin, A.; Block, J. C.; Genin, J. M. R., Iron(II,III) hydroxycarbonate green rust formation and stabilization from lepidocrocite bioreduction. *Environmental Science & Technology* **2002,** *36* (1), 16-20.

27. Legrand, L.; Abdelmoula, M.; Gehin, A.; Chausse, A.; Genin, J. M. R., Electrochemical formation of a new Fe(II)-Fe(III) hydroxy-carbonate green rust: characterisation and morphology. *Electrochim. Acta* **2001,** *46* (12), 1815-1822.

28. Genin, J. M. R.; Aissa, R.; Gehin, A.; Abdelmoula, M.; Benali, O.; Ernstsen, V.; Ona-Nguema, G.; Upadhyay, C.; Ruby, C., Fougerite and FeII-III hydroxycarbonate green rust; ordering drprotonation and/or cation substitution; structure of hydrotalcite-like compounds and mythic ferrosic hydroxide Fe(OH)((2+x)). *Solid State Sci.* **2005,** *7* (5), 545-572.

29. Refait, P.; Simon, L.; Genin, J. M. R., Reduction of SeO42- anions and anoxic formation of iron(II)-iron(III) hydroxy selenate green rust. *Environmental Science & Technology* **2000,** *34* (5), 819-825.

30. Refait, P.; Charton, A.; Genin, J. M. R., Identification, composition, thermodynamic and structural properties of a pyroaurite-like iron(II)-iron(III) hydroxy-oxalate Green Rust. *Eur. J. Solid State Inorg. Chem.* **1998,** *35* (10-11), 655-666.

31. Ayala-Luis, K. B.; Koch, C. B.; Hansen, H. C. B., One-pot synthesis and characterization of Fe-II-Fe-III hydroxide (green rust) intercalated with C9-C14 linear alkyl carboxylates. *Appl. Clay Sci.* **2010,** *50* (4), 512-519.

32. Refait, P.; Drissi, S. H.; Pytkiewicz, J.; Genin, J. M. R., The anionic species competition in iron aqueous corrosion: Role of various green rust compounds. *Corrosion Science* **1997,** *39* (9), 1699-1710.

33. Genin, J. M. R.; Ruby, C.; Gehin, A.; Refait, P., Synthesis of green rusts by oxidation of Fe(OH)(2), their products of oxidation and reduction of ferric oxyhydroxides; Eh-pH Pourbaix diagrams. *C. R. Geosci.* **2006,** *338* (6-7), 433-446.

34. Ruby, C.; Aissa, R.; Gehin, A.; Cortot, J.; Abdelmoula, M.; Genin, J. M., Green rusts synthesis by coprecipitation of Fe-II-Fe-III ions and mass-balance diagram. *C. R. Geosci.* **2006,** *338* (6-7), 420-432.

35. Boucherit, N.; Goff, A. H. L.; Joiret, S., RAMAN STUDIES OF CORROSION FILMS GROWN ON FE AND FE-6MO IN PITTING CONDITIONS. *Corrosion Science* **1991,** *32* (5-6), 497-507.

36. Refait, P.; Benali, O.; Abdelmoula, M.; Genin, J. M. R., Formation of 'ferric green rust' and/or ferrihydrite by fast oxidation of iron(II-III) hydroxychloride green rust. *Corrosion Science* **2003,** *45* (11), 2435-2449.

37. Mullet, M.; Guillemin, Y.; Ruby, C., Oxidation and deprotonation of synthetic Fe-II-Fe-III (oxy)hydroxycarbonate Green Rust: An X-ray photoelectron study. *J. Solid State Chem.* **2008,** *181* (1), 81-89.

38. Miyata, S., SYNTHESES OF HYDROTALCITE-LIKE COMPOUNDS AND THEIR STRUCTURES AND PHYSICOCHEMICAL PROPERTIES .1. SYSTEMS MG2+-AL3+-NO-3,MG2+-AL3+-CL-,MG2+-AL3+-CLO-4,NI2P-AL3+-CL- AND ZN2+-AL3+-CL. *Clays and Clay Minerals* **1975,** *23* (5), 369-&.

39. Simon, L.; Francois, M.; Refait, P.; Renaudin, G.; Lelaurain, M.; Genin, J. M. R., Structure of the Fe(II-III) layered double hydroxysulphate green rust two from Rietveld analysis. *Solid State Sci.* **2003,** *5* (2), 327-334.

40. Refait, P.; Abdelmoula, M.; Trolard, F.; Genin, J. M. R.; Ehrhardt, J. J.; Bourrie, G., Mossbauer and XAS study of a green rust mineral; the partial substitution of Fe2+ by Mg2+. *Am. Miner.* **2001,** *86* (5-6), 731-739.

41. Jolivet, J. P.; Chaneac, C.; Tronc, E., Iron oxide chemistry. From molecular clusters to extended solid networks. *Chem. Commun.* **2004,** (5), 481-487.

42. O'Loughlin, E. J.; Larese-Casanova, P.; Scherer, M.; Cook, R., Green rust formation from the bioreduction of gamma-FeOOH (lepidocrocite): Comparison of several Shewanella species. *Geomicrobiol. J.* **2007,** *24* (3-4), 211-230.

43. Legrand, L.; Mazerolles, L.; Chausse, A., The oxidation of carbonate green rust into ferric phases: solid-state reaction or transformation via solution. *Geochim. Cosmochim. Acta* **2004,** *68* (17), 3497-3507.

44. Kwon, S. K.; Kimijima, K.; Kanie, K.; Suzuki, S.; Muramatsu, A.; Saito, M.; Shinoda, K.; Waseda, Y., Influence of silicate ions on the formation of goethite from green rust in aqueous solution. *Corrosion Science* **2007,** *49* (7), 2946-2961.

45. Ruby, C.; Usman, M.; Naille, S.; Hanna, K.; Carteret, C.; Mullet, M.; Francois, M.; Abdelmoula, M., Synthesis and transformation of iron-based layered double hydroxides. *Appl. Clay Sci.* **2010,** *48* (1-2), 195-202.

46. Benali, O.; Abdelmoula, M.; Refait, P.; Genin, J. M. R., Effect of orthophosphate on the oxidation products of Fe(II)-Fe(III) hydroxycarbonate: The transformation of green rust to ferrihydrite. *Geochim. Cosmochim. Acta* **2001,** *65* (11), 1715-1726.

47. Antony, H.; Legrand, L.; Chausse, A., Carbonate and sulphate green rusts - Mechanisms of oxidation and reduction. *Electrochim. Acta* **2008,** *53* (24), 7146-7156.

48. Ayala-Luis, K. B.; Koch, C. B.; Hansen, H. C. B., Intercalation of linear C9-C16 carboxylates in layered Fe-II-Fe-III-hydroxides (green rust) via ion exchange. *Appl. Clay Sci.* **2010,** *48* (3), 334-341.

49. Dyar, M. D.; Agresti, D. G.; Schaefer, M. W.; Grant, C. A.; Sklute, E. C., Mossbauer spectroscopy of earth and planetary materials. In *Annual Review of Earth and Planetary Sciences*, 2006; Vol. 34, pp 83-125.

50. Genin, J. M. R.; Ruby, C., Anion and cation distributions in Fe(II-III) hydroxysalt green rusts from XRD and Mossbauer analysis (carbonate, chloride, sulphate,...); the "fougerite" mineral. *Solid State Sci.* **2004,** *6* (7), 705-718.

51. McGill, I. R.; McEnaney, B.; Smith, D. C., Crystal structure of green rust formed by corrosion of cast iron. *Nature* **1976,** *259* (5540), 200-201.

52. Kelly, S. D., Hesterberg, D. and Ravel, B., Analysis of soils and minerals using X-ray absorption spectroscopy. In *Methods of Soil Analysis, Part 5 - Mineralogical Methods*, Drees, A. L. U. a. L. R., Ed. Soil Science Society of America: Madison, WI, USA, 2008; p 387.

53. Suzuki, S.; Shinoda, K.; Sato, M.; Fujimoto, S.; Yamashita, M.; Konishi, H.; Doi, T.; Kamimura, T.; Inoue, K.; Waseda, Y., Changes in chemical state and local structure of green rust by addition of copper sulphate ions. *Corrosion Science* **2008,** *50* (6), 1761-1765.

54. Chung, K. T.; Fulk, G. E.; Andrews, A. W., MUTAGENICITY TESTING OF SOME COMMONLY USED DYES. *Applied and Environmental Microbiology* **1981,** *42* (4), 641-648.

55. Kone, T.; Hanna, K.; Abdelmoula, M.; Ruby, C.; Carteret, C., Reductive transformation and mineralization of an azo dye by hydroxysulphate green rust preceding oxidation using H2O2 at neutral pH. *Chemosphere* **2009,** *75* (2), 212-219.

56. Meharg, A. A.; Raab, A., Getting to the bottom of arsenic standards and guidelines. *Environ. Sci. Technol.* **2010,** *44* (12), 4395-4399.

57. Randall, S. R.; Sherman, D. M.; Ragnarsdottir, K. V., Sorption of As(V) on green rust (Fe-4(II)Fe-2(III)(OH)(12)SO4 center dot 3H(2)O) and lepidocrocite (gamma-FeOOH): Surface complexes from EXAFS spectroscopy. *Geochim. Cosmochim. Acta* **2001,** *65* (7), 1015-1023.

58. Schwertmann, U.; Fechter, H., The Formation of Green Rust and Its Transformation to Lepidocrocite. *Clay Min.* **1994,** *29* (1), 87-92.

59. Lin, Y. T.; Weng, C. H.; Chen, F. Y., Effective removal of AB24 dye by nano/micro-size zero-valent iron. *Sep. Purif. Technol.* **2008,** *64* (1), 26-30.

60. Liu, Y. Q.; Majetich, S. A.; Tilton, R. D.; Sholl, D. S.; Lowry, G. V., TCE dechlorination rates, pathways, and efficiency of nanoscale iron particles with different properties. *Environmental Science & Technology* **2005,** *39* (5), 1338-1345.

61. Bond, D. L.; Fendorf, S., Kinetics and structural constraints of chromate reduction by green rusts. *Environmental Science & Technology* **2003,** *37* (12), 2750-2757.

62. Skovbjerg, L. L.; Stipp, S. L. S.; Utsunomiya, S.; Ewing, R. C., The mechanisms of reduction of hexavalent chromium by green rust sodium sulphate: Formation of Cr-goethite. *Geochim. Cosmochim. Acta* **2006,** *70* (14), 3582-3592.

63. Hanna, K.; Kone, T.; Ruby, C., Fenton-like oxidation and mineralization of phenol using synthetic Fe(II)-Fe(III) green rusts. *Environ. Sci. Pollut. Res.* **2010,** *17* (1), 124-134.

64. Amonette, J. E.; Workman, D. J.; Kennedy, D. W.; Fruchter, J. S.; Gorby, Y. A., Dechlorination of carbon tetrachloride by Fe(II) associated with goethite. *Environmental Science & Technology* **2000,** *34* (21), 4606-4613.

65. Elsner, M.; Schwarzenbach, R. P.; Haderlein, S. B., Reactivity of Fe(II)-bearing minerals toward reductive transformation of organic contaminants. *Environmental Science & Technology* **2004,** *38* (3), 799-807.

66. Gorski, C. A.; Nurmi, J. T.; Tratnyek, P. G.; Hofstetter, T. B.; Scherer, M. M., Redox Behavior of Magnetite: Implications for Contaminant Reduction. *Environmental Science & Technology* **2010,** *44* (1), 55-60.

67. Ayala-Luis, K. B.; Cooper, N. G. A.; Koch, C. B.; Hansen, H. C. B., Efficient Dechlorination of Carbon tetrachloride by Hydrophobic Green Rust Intercalated with Dodecanoate Anions (vol 46, pg 3390, 2012). *Environmental Science & Technology* **2012,** *46* (8), 4683-4683.

68. Fang, G. D.; Dionysiou, D. D.; Al-Abed, S. R.; Zhou, D. M., Superoxide radical driving the activation of persulfate by magnetite nanoparticles: Implications for the degradation of PCBs. *Appl. Catal. B-Environ.* **2013,** *129*, 325-332.

69. Latta, D. E.; Gorski, C. A.; Boyanov, M. I.; O'Loughlin, E. J.; Kemner, K. M.; Scherer, M. M., Influence of Magnetite Stoichiometry on U-VI Reduction. *Environmental Science & Technology* **2012,** *46* (2), 778-786.

70. Rusevova, K.; Kopinke, F. D.; Georgi, A., Nano-sized magnetic iron oxides as catalysts for heterogeneous Fenton-like reactions-Influence of Fe(II)/Fe(III) ratio on catalytic performance. *J. Hazard. Mater.* **2012,** *241*, 433-440.

71. Gorski, C. A.; Scherer, M. M., Influence of Magnetite Stoichiometry on Fe-II Uptake and Nitrobenzene Reduction. *Environmental Science & Technology* **2009,** *43* (10), 3675-3680.

72. Usman, M.; Hanna, K.; Abdelmoula, M.; Zegeye, A.; Faure, P.; Ruby, C., Formation of green rust via mineralogical transformation of ferric oxides (ferrihydrite, goethite and hematite). *Appl. Clay Sci.* **2012,** *64*, 38-43.

73. Kim, W.; Suh, C. Y.; Cho, S. W.; Roh, K. M.; Kwon, H.; Song, K.; Shon, I. J., A new method for the identification and quantification of magnetite-maghemite mixture using conventional X-ray diffraction technique. *Talanta* **2012,** *94,* 348-352.

74. Rickard, D.; Luther, G. W., Chemistry of iron sulfides. *Chem. Rev.* **2007,** *107* (2), 514-562.

75. Fleischer, H.; Dienes, Y.; Mathiasch, B.; Schmitt, V.; Schollmeyer, D., Cysteamine and its homoleptic complexes with group 12 metal ions. Differences in the coordination chemistry of Zn-II, Cd-II, and Hg-II with a small N,S-donor ligand. *Inorg. Chem.* **2005,** *44* (22), 8087-8096.

76. Vauquelin, L. N., Such as hydrogen sulfide acts on iron, and whether to form hydrochloric acid. *Ann. Pys. Leipzig* **1801,** *9* (40).

77. Yoshioka, H., A STUDY ON CORROSION OF IRON BY ELECTRON DIFFRACTION. *J. Phys. Soc. Jpn.* **1949,** *4* (4-6), 270-275.

78. Rao, T. V.; Sain, B.; Murthy, P. S.; Rao, T.; Jain, A. K.; Joshi, G. C., Iron(III)-ethylenediaminetetraacetic acid mediated oxidation of thiols to disulfides with molecular oxygen. *J. Chem. Res.-S* **1997,** (8), 300-301.

79. Mikhlin, Spectroscopic and XRD studies of the air degradation of acid-reacted pyrrhotites. *Geochim. Cosmochim. Acta* **2002,** *66* (23), 4057-4067.

80. Woods, B. a., **1997**.

81. Kim, C. H.; Parkin, S.; Bharara, M.; Atwood, D., Linear coordination of Hg(II) by cysteamine. *Polyhedron* **2002,** *21* (2), 225-228.

82. Gorski, C. A.; Scherer, M. M., Determination of nanoparticulate magnetite stoichiometry by Mossbauer spectroscopy, acidic dissolution, and powder X-ray diffraction: A critical review. *Am. Miner.* **2010,** *95* (7), 1017-1026.

83. Woo, K.; Hong, J.; Choi, S.; Lee, H. W.; Ahn, J. P.; Kim, C. S.; Lee, S. W., Easy synthesis and magnetic properties of iron oxide nanoparticles. *Chem. Mat.* **2004,** *16* (14), 2814-2818.

84. Bishop, M., Hailiang, D., Jaisi, D., Ravi K., Ji, J. In *BIOAVAILABILITY OF FE(III) IN LOESS SEDIMENTS: AN IMPORTANT SOURCE OF ELECTRON ACCEPTORS*, CLAYS OF THE BIG SKY: 46th Annual Meeting of The Clay Minerals Society, Billings, Montana, USA, Joseph W. Stucki, U. o. I., Ed. Billings, Montana, USA, 2009; p 54.

85. Yavuz, C. T.; Mayo, J. T.; Yu, W. W.; Prakash, A.; Falkner, J. C.; Yean, S.; Cong, L. L.; Shipley, H. J.; Kan, A.; Tomson, M.; Natelson, D.; Colvin, V. L., Low-field magnetic separation of monodisperse Fe3O4 nanocrystals. *Science* **2006,** *314* (5801), 964-967.

86. Temperley, A. A., Lefevre, H.W., THE MOSSBAUER EFFECT IN MARCASITE STRUCTURE IRON COMPOUNDS. *Journal of Physics and Chemistry of Solids* **1966,** *27*, 85-92.

87. Blomquist, J.; Helgeson, U.; Folkesson, B.; Larsson, R., STUDIES OF SOME IRON DITHIOLATE COMPLEXES BY THE ESCA, MOSSBAUER AND EXTENDED HUCKEL METHODS. *Chem. Phys.* **1983,** *76* (1), 71-78.

88. Jones, C. J., Chattopadhyay, S., Lee, S.S., Hwang, N., Cho, M., Ozarowski, A., Guo, W., Kelly, S.D., Mayo, J.T., Prakash, A., Gonzales Pech, N., Avendano, C., Colvin, V.L *Investigation of Novel Iron Material's Composition via Mössbauer Spectroscopy*; 2011.

89. Stiefl, E. I., Transitional Metal Sulfur Chemistry: Biological and Industrial Significance and Key Trends. In *Transition Metal Sulfur Chemistry: Biological and Industrial Significance*, 1996.

90. DuBois, M. R. J., B.; Noll, B.; Dietz, S., Synthesis, Structures, and Reactions of Cyclopentadienyl Metal Complexes with Bridging Sulfur Ligands. In *Transition Metal Sulfur Chemistry: Biological and Industrial Significance*, 1996.

91. Yu, W. W.; Falkner, J. C.; Yavuz, C. T.; Colvin, V. L., Synthesis of monodisperse iron oxide nanocrystals by thermal decomposition of iron carboxylate salts. *Chem. Commun.* **2004,** (20), 2306-2307.

92. Segre, C. U., et. al In *Synchrotron Radiation Instrumentation*, Eleventh U.S. National Conference CP521, 2000; pp 419-422.

93. Newville, M., IFEFFIT: interactive EXAFS analysis and FEFF fitting. *J. Synchrotron Rad.* **2001,** *8*, 322-324.

94. Zabinsky, S. I.; Rehr, J. J.; Ankudinov, A.; Albers, R. C.; Eller, M. J., MULTIPLE-SCATTERING CALCULATIONS OF X-RAY-ABSORPTION SPECTRA. *Phys. Rev. B* **1995,** *52* (4), 2995-3009.

95. Ravel, B.; Newville, M., ATHENA, ARTEMIS, HEPHAESTUS: data analysis for X-ray absorption spectroscopy using IFEFFIT. *J. Synchrot. Radiat.* **2005,** *12*, 537-541.

96. Taylor, P.; Shoesmith, D. W., Nature of Green Alkaline Iron Sulfide Solutions and Preparation of Sodium Iron(Iii) Sulfide, Nafes2. *Can. J. Chem.-Rev. Can. Chim.* **1978,** *56* (22), 2797-2802.

97. Mellor, J. W., *A comprehensive treatise on inorganic and theoretical chemistry*. Longmans: London, 1935; Vol. XIV.

98. Pavelko, G. F., Reactions of thiols and organic disulfides with iron and its oxides. *Russ. Chem. Bull.* **2006,** *55* (8), 1436-1439.

99. Penfold, B. R.; Grigor, J. A., THE CRYSTAL STRUCTURE OF IRON(II) CHLORIDE TETRAHYDRATE. *Acta Crystallographica* **1959,** *12* (11), 850-854.

100. Karpenko, V.; Norris, J. A., Vitriol in the history of chemistry. *Chem. Listy* **2002,** *96* (12), 997-1005.

101. Pavelko, G. F., Reactions of thiols and organic sulfides with hydrogen in the presence of iron powder. **2006**.

102. Shriver, A. a., d-Metal Complexes: Electronic Structure and Spectra. In *Inorg. Chem.*, 4th ed.; 2006.

103. Miessler, G. L., Tarr, D.A., Electronic Spectra of Coordination Compounds. In *Inorg. Chem.*, Pearson Prentice Hall: Upper Saddle River, NJ, 2004; p p407.

104. Lancashire, R. J. Tanabe-Sugano Diagrams. http://wwwchem.uwimona.edu.jm/courses/Tanabe-Sugano/TanSugd6ls.html (accessed October 2012).

105. Kondo, M.; Yoshizawa, K., A theoretical study of spin-orbit coupling in an Fe(II) spin-crossover complex. Mechanism of the LIESST effect. *Chem. Phys. Lett.* **2003,** *372* (3-4), 519-523.

106. Nassau, K., THE CAUSES OF COLOR. *Sci.Am.* **1980,** *243* (4), 124-&.

107. Gorelsky, S. I.; Basumallick, L.; Vura-Weis, J.; Sarangi, R.; Hodgson, K. O.; Hedman, B.; Fujisawa, K.; Solomon, E. I., Spectroscopic and DFT investigation of M{HB(3,5-(i)Pr(2)pz)(3)}(SC6F5) (M = Mn, Fe, Co, Ni, Cu, and Zn) model complexes: Periodic trends in metal-thiolate bonding. *Inorg. Chem.* **2005,** *44* (14), 4947-4960.

108. NIST XPS Database. http://srdata.nist.gov/xps/ (accessed 2008).

109. Volmeruebing, M.; Stratmann, M., A Surface Analytical and an Electrochemical Study of Iron Surfaces Modified by Thiols. *Appl. Surf. Sci.* **1992,** *55* (1), 19-35.

110. Vaughan, D. J.; Lennie, A. R., THE IRON SULFIDE MINERALS - THEIR CHEMISTRY AND ROLE IN NATURE. *Science Progress* **1991,** *75* (298), 371-388.

111. Pratt, A. R.; Muir, I. J.; Nesbitt, H. W., X-RAY PHOTOELECTRON AND AUGER-ELECTRON SPECTROSCOPIC STUDIES OF PYRRHOTITE AND MECHANISM OF AIR OXIDATION. *Geochim. Cosmochim. Acta* **1994,** *58* (2), 827-841.

112. Jones, C. F.; Lecount, S.; Smart, R. S. C.; White, T. J., COMPOSITIONAL AND STRUCTURAL ALTERATION OF PYRRHOTITE SURFACES IN SOLUTION - XPS AND XRD STUDIES. *Appl. Surf. Sci.* **1992,** *55* (1), 65-85.

113. Herbert, R. B.; Benner, S. G.; Pratt, A. R.; Blowes, D. W., Surface chemistry and morphology of poorly crystalline iron sulfides precipitated in media containing sulfate-reducing bacteria. *Chem. Geol.* **1998,** *144* (1-2), 87-97.

114. Coates, J., Interpretation of Infrared Spectra, A Practical Approach. In *Encyclopedia of Analytical Chemistry*, Meyers, R. A., Ed. John Wiley & Sons Ltd: Chichester,, 2000; pp pp. 10815–10837.

115. Johnson, M. K.; Hare, J. W.; Spiro, T. G.; Moura, J. J. G.; Xavier, A. V.; Legall, J., Resonance Raman-Spectra of 3-Iron Centers in Ferredoxins from Desulfovibrio-Gigas. *J. Biol. Chem.* **1981,** *256* (19), 9806-9808.

116. Dave, B. C.; Czernuszewicz, R. S.; Prickril, B. C.; Kurtz, D. M., Resonance Raman-Spectroscopic Evidence for the Fes4 and Fe-O-Fe Sites in Rubrerythrin from Desulfovibrio-Vulgaris. *Biochemistry* **1994,** *33* (12), 3572-3576.

117. Descostes, M.; Beaucaire, C.; Mercier, F.; Savoye, S.; Sow, J.; Zuddas, P., Effect of carbonate ions on pyrite (FeS2) dissolution. *Bull. Soc. Geol. Fr.* **2002,** *173* (3), 265-270.

118. Wrzosek, B.; Bukowska, J.; Kudelski, A., Raman study on the structure of adlayers formed on silver from mixtures of 2-aminoethanethiol and 3-mercaptopropionic acid. *J. Raman Spectrosc.* **2005,** *36* (11), 1040-1046.

119. Descostes, M.; Schlegel, M. L.; Eglizaud, N.; Descamps, F.; Miserque, F.; Simoni, E., Uptake of uranium and trace elements in pyrite (FeS2) suspensions. *Geochim. Cosmochim. Acta* **2010,** *74* (5), 1551-1562.

120. Mernagh, T. P.; Trudu, A. G., A LASER RAMAN MICROPROBE STUDY OF SOME GEOLOGICALLY IMPORTANT SULFIDE MINERALS. *Chem. Geol.* **1993,** *103* (1-4), 113-127.

121. Remazeilles, C.; Saheb, M.; Neff, D.; Guilminot, E.; Tran, K.; Bourdoiseau, J. A.; Sabot, R.; Jeannin, M.; Matthiesen, H.; Dillmann, P.; Refait, P., Microbiologically influenced corrosion of archaeological artefacts: characterisation of iron(II) sulfides by Raman spectroscopy. *J. Raman Spectrosc.* **2010,** *41* (11), 1425-1433.

122. Bon, C. E. In *The morphology and structure of smythite, (Fe,Ni)3S4, from Bloomington, Indiana*, The 38th Rochester Mineralogical Symposium, Radisson Hotel Rochester Airport, Radisson Hotel Rochester Airport, 2011.

123. White, S. N., Laser Raman spectroscopy as a technique for identification of seafloor hydrothermal and cold seep minerals. *Chem. Geol.* **2009,** *259* (3-4), 240-252.

124. Zhu, L.; Richardson, B.; Tanumihardja, J.; Yu, Q. M., Controlling morphology and phase of pyrite FeS2 hierarchical particles via the combination of structure-direction and chelating agents. *Crystengcomm* **2012,** *14* (12), 4188-4195.

125. Morice, J. A., Rees, L.V.C., Rickard, D.T., Mossbauer Studies of Iron Sulphides. *Journal of Inorganic & Nuclear Chemistry* **1969,** *31*, 3797.

126. Berry, F. J.; Jones, C. J.; McCleverty, J. A.; Sharpe, J.; Bailey, N. A.; Deadman, M., STRUCTURAL AND MOSSBAUER INVESTIGATIONS OF SOME IRON COMPLEXES CONTAINING BOTH CARBONYL AND SULFUR LIGANDS. *Journal of Organometallic Chemistry* **1988,** *353* (2), 209-213.

127. Rudneva, T. N.; Sanina, N. A.; Lyssenko, K. A.; Aldoshin, S. M.; Antipin, M. Y.; Ovanesyan, N. S., Synthesis and structure of a water-soluble nitrosyl iron complex with cysteamine ligand. *Mendeleev Commun.* **2009,** *19* (5), 253-255.

128. Fleissner, G.; Kozlowski, P. M.; Vargek, M.; Bryson, J. W.; O'Halloran, T. V.; Spiro, T. G., UVRR spectroscopy and vibrational analysis of mercury thiolate compounds resembling d(10) metal binding sites in proteins. *Inorg. Chem.* **1999,** *38* (15), 3523-3528.

129. Maresca, K. P.; Femia, F. J.; Bonavia, G. H.; Babich, J. W.; Zubieta, J., Cationic complexes of the '3+1' oxorhenium-thiolate family. *Inorg. Chim. Acta* **2000,** *297* (1-2), 98-105.

130. Bronstein, L. M.; Huang, X. L.; Retrum, J.; Schmucker, A.; Pink, M.; Stein, B. D.; Dragnea, B., Influence of iron oleate complex structure on iron oxide nanoparticle formation. *Chem. Mat.* **2007,** *19* (15), 3624-3632.

131. Kolthoff, I. M.; Meehan, E. J.; Choi, Q. W.; Tsao, M. S., OXIDATION OF NORMAL-OCTYL MERCAPTAN BY FERRICYANIDE IN ACETONE-WATER SOLUTION. *J. Phys. Chem.* **1962,** *66* (7), 1233-&.

132. Patai, S., *The Chemistry of the Thiol Group*. John Wiley & Sons: London, New York, Sydney, Toronto, 1974; Vol. II.

133. Kooyman, E. C., Thiyl Radicals. *Pure and Applied Chemistry* **1967,** *15* (1), 81-88.

134. O'Toole, M. G.; Kreso, M.; Kozlowski, P. M.; Mashuta, M. S.; Grapperhaus, C. A., Spin-state-dependent oxygen sensitivity of iron dithiolates: sulfur oxygenation or disulfide formation. *Journal of Biological Inorganic Chemistry* **2008,** *13* (8), 1219-1230.

135. Rajsekhar, G.; Rao, C. P.; Saarenketo, P. K.; Kolehmainen, E.; Rissanen, K., C-S bond cleavage by cobalt: synthesis, characterization and crystal structure determination of 1,2-di-(o-salicylaldiminophenylthio)ethane and its Co(III) product with C-S bond cleaved fragments. *Inorg. Chem. Commun.* **2002,** *5* (9), 649-652.

136. Rahman, M., Arsenic and contamination of drinking-water in Bangladesh: A public-health perspective. *J. Heatlh Popul. Nutr.* **2002,** *20* (3), 193-197.

137. Marchiset-Ferlay, N.; Savanovitch, C.; Sauvant-Rochat, M. P., What is the best biomarker to assess arsenic exposure via drinking water? *Environ. Int.* **2012,** *39* (1), 150-171.

138. Smedley, P. L.; Kinniburgh, D. G., A review of the source, behaviour and distribution of arsenic in natural waters. *Appl. Geochem.* **2002,** *17* (5), 517-568.

139. Mohan, D.; Pittman, C. U., Arsenic removal from water/wastewater using adsorbents - A critical review. *J. Hazard. Mater.* **2007,** *142* (1-2), 1-53.

140. Arsenic in drinking water. Fact Sheets. http://www.who.int/mediacentre/factsheets/fs210/en/index.html.

141. Government Decree No. 201/2001. (X.25.) on the quality standards and monitoring of drinking waters. http://net.jogtar.hu/jr/gen/hjegy_doc.cgi?docid=A0100201.KOR.

142. Petrusevski, B., Sharma, S.K., Schippers, J.C. and Shordt, K. *Arsenic in drinking water*; IRC: Delft, The Netherlands. , 2007.

143. MSZ 445, 1989. Hungarian Standard about the quality of drinking water. 1989.

144. Directive 98/83/EC on the quality of water intended for human consumption. http://eur-lex.europa.eu/LexUriServ/LexUriServ.do?uri=CELEX:31998L0083:EN:NOT.

145. Gregor, J., Arsenic removal during conventional aluminium-based drinking-water treatment. *Water Res.* **2001,** *35* (7), 1659-1664.

146. Wickramasinghe, S. R.; Han, B. B.; Zimbron, J.; Shen, Z.; Karim, M. N., Arsenic removal by coagulation and filtration: comparison of groundwaters from the United States and Bangladesh. *Desalination* **2004,** *169* (3), 231-244.

147. Floch, J.; Hideg, M., Application of ZW-1000 membranes for arsenic removal from water sources. *Desalination* **2004,** *162* (1-3), 75-83.

148. Han, B. B.; Runnells, T.; Zimbron, J.; Wickramasinghe, R., Arsenic removal from drinking water by flocculation and microfiltration. *Desalination* **2002,** *145* (1-3), 293-298.

149. Leventon, J. We don't eat fish…" Science, policy and EU governance: the implementation of arsenic limits for drinking water in a Hungarian case study. Central European University, Budapest, Hungary, 2011.

150. Dodbiba, G.; Nukaya, T.; Kamioka, Y.; Tanimura, Y.; Fujita, T., Removal of arsenic from wastewater using iron compound: Comparing two different types of adsorbents in the context of LCA. *Resour. Conserv. Recycl.* **2009,** *53* (12), 688-697.

151. Arpke, A.; Hutzler, N., Domestic water use in the United States - A life-cycle approach. *J. Ind. Ecol.* **2006,** *10* (1-2), 169-184.

152. NIST BEES Software. http://www.nist.gov/el/economics/BEESSoftware.cfm.

153. SimaPro Pricing. http://www.pre-sustainability.com/pricelist.

154. Godskesen, B.; Zambrano, K. C.; Trautner, A.; Johansen, N. B.; Thiesson, L.; Andersen, L.; Clauson-Kaas, J.; Neidel, T. L.; Rygaard, M.; Kloverpris, N. H.; Albrechtsen, H. J., Life cycle assessment of three water systems in Copenhagen-a management tool of the future. *Water Sci. Technol.* **2011,** *63* (3), 565-572.

155. Hungarian Technical Guidelines MI-10-135-4: 1981 – Water treatment equipments, Elimination of iron and manganese. 1981.

156. Mészáros, G. *Subsurface water treatment*; Eötvös József College: Baja, Hungary, 1998.

157. Laky, D.; Licsko, I., Arsenic removal by ferric-chloride coagulation - effect of phosphate, bicarbonate and silicate. *Water Sci. Technol.* **2011,** *64* (5), 1046-1055.

158. Guinée, J. B., Gorrée, M., Heijungs, R., Huppes, G., Kleijn, R., Koning, A. de, Oers, L. van, Wegener Sleeswijk, A., Suh, S., Udo de Haes, H.A., Bruijn, H. de, Duin, R. van, Huijbregts, M.A.J. , *Handbook on life cycle assessment. Operational guide to the ISO standards.* . Dordrecht, 2002.

159. EN ISO 14044:2006 Environmental Management – Life Cycle Assessment – Requirements and Guidelines. 2006.

160. Raluy, G.; Serra, L.; Uche, J., Life cycle assessment of MSF, MED and RO desalination technologies. *Energy* **2006,** *31* (13), 2361-2372.

161. Smith, V. H.; Tilman, G. D.; Nekola, J. C., Eutrophication: impacts of excess nutrient inputs on freshwater, marine, and terrestrial ecosystems. *Environ. Pollut.* **1999,** *100* (1-3), 179-196.

162. Bobbink, R.; Hornung, M.; Roelofs, J. G. M., The effects of air-borne nitrogen pollutants on species diversity in natural and semi-natural European vegetation. *J. Ecol.* **1998,** *86* (5), 717-738.

163. Huijbregts, M. A. J.; Thissen, U.; Guinee, J. B.; Jager, T.; Kalf, D.; van de Meent, D.; Ragas, A. M. J.; Sleeswijk, A. W.; Reijnders, L., Priority assessment of toxic substances in life cycle assessment. Part I: Calculation of toxicity potentials for 181 substances with the nested multi-media fate, exposure and effects model USES-LCA. *Chemosphere* **2000,** *41* (4), 541-573.